A Computational and Experimental Study on the Electrical and Thermal Properties of Hybrid Nanocomposites based on Carbon Nanotubes and Graphite Nanoplatelets

Masoud Safdari

Dissertation submitted to the Faculty of the
Virginia Polytechnic Institute and State University
in partial fulfillment of the requirements for the degree of

Doctor of Philosophy
in
Engineering Mechanics

Marwan S. Al-Haik, Chair
Michael L. Madigan
Robert L. West
Shane D. Ross
Sunny Jung

December 3rd, 2012
Blacksburg, Virginia

Keywords: Carbon Nanotube, Graphite Nanoplatelet, Thermal Conductivity, Electrical Conductivity, Polymer Nanocomposites

A Computational and Experimental Study on the Electrical and Thermal Properties of Hybrid Nanocomposites based on Carbon Nanotubes and Graphite Nanoplatelets

Masoud Safdari

(ABSTRACT)

Carbon nanotubes (CNTs) and graphite nanoplatelets (GNPs) are carrying great promise as two important constituents of future multifunctional materials. Originating from their minimal defect confined nanostructure, exceptional thermal and electrical properties have been reported for these two allotropic forms of carbon. However, a brief survey of the literature reveals the fact that the incorporation of these species into a polymer matrix enhances its effective properties usually not to the degree predicted by the composite's upper bound rule. To exploit their full potential, a proper understanding of the physical laws characterizing their behavior is an essential step. With emphasis on the electrical and thermal properties, the following study is an attempt to provide more realistic physical and computational models for studying the transport properties of these nanomaterials.

Originated from quantum confinement effects, electron tunneling is believed to be an important phenomenon in determining the electrical properties of nanocomposites comprising CNTs and GNPs. To assess its importance, in this dissertation this phenomenon is incorporated into simulations by utilizing tools from statistical physics. A qualitative parametric study was carried out to demonstrate its dominating importance. Furthermore, a model is adopted from the

literature and extended to quantify the electrical conductivity of these nanocomposite. To establish its validity, the model predictions were compared with relevant published findings in the literature. The applicability of the proposed model is confirmed for both CNTs and GNPs.

To predict the thermal properties, a statistical continuum based model, originally developed for two-phase composites, is adopted and extended to describe multiphase nanocomposites with high contrast between the transport properties of the constituents. The adopted model is a third order strong-contrast expansion which directly links the thermal properties of the composite to the thermal properties of its constituents by considering the microstructural effects. In this approach, a specimen of the composite is assumed to be confined into a reference medium with known properties subjected to a temperature field in the infinity to predict its effective thermal properties. It was noticed that such approach is highly sensitive to the properties of the reference medium. To overcome this shortcoming, a technique to properly select the reference medium properties was developed. For verification purpose the proposed model predictions were compared with the corresponding finite element calculations for nanocomposites comprising cylindrical and disk-shaped nanoparticles.

To shed more light on some conflicting reports about the performance of the hybrid CNT/GNP/polymer nanocomposites, an experimental study was conducted to study a hybrid ternary system. CNT/polymer, GNP/polymer and CNT/GNP/polymer nanocomposite specimens were processed and tested to evaluate their thermal and electrical conductivities. It was observed that the hybrid CNT/GNP/polymer composites outperform polymer composites loaded solely with CNTs or GNPs.

Finally, the experimental findings were utilized to serve as basis to validate the models developed in this dissertation. The experimental study was utilized to reduce the modeling uncertainties and the computational predictions of the proposed models were compared with the experimental measurements. Acceptable agreements between the model predictions and experimental data were observed

and explained in light of the experimental observations.

The work proposed herein will enable significant advancement in understanding the physical phenomena behind the enhanced electrical and thermal conductivities of polymer nanocomposites specifically CNT/GNP/polymer nanocomposites. The dissertation results offer means to tune-up the electrical and thermal properties of the polymer nanocomposite materials to further enhance their performance.

To my parents Ezzat and Mortaza and to my wife Fatemeh for their everlasting support and love....

Acknowledgements

It is really difficult to acknowledge those whom helped me throughout this endeavor to the extent they deserve....
First, I express my deepest appreciation and gratitude to my advisor Dr. Marwan Al-Haik for his diligence, wisdom, insight and strong sense of humor that paved my road when I was struggling and shined my direction when I was clueless. I kindly appreciate all of his priceless efforts in teaching me how to conduct research effectively. He was not only my scientific advisor but also my life mentor whom without his endless support I would not be here today. He encouraged the sprit of fairness in me and I would always appreciate him for all the lessons of life I learned from him.

Second, I would like to acknowledge those who directly and indirectly assisted me throughout my Ph.D. tenure. Many thanks goes to Dr. Majid Baniassadi for his commitment to excellence and for his scientific advices and inputs throughout this research. My sincere gratitude goes to Dr. Hamid Garmestani who introduced me to Dr. Al-Haik and always supported me. I sincerely appreciate my Ph.D. committee members Dr. Michael Madigan who taught me discipline, Dr. Bob West who taught me integrity, Dr. Shane Ross who taught me insight and Dr. Sunny Jung who taught me the passion for research. I would like to thank Dr. Muhammad Hajj and Mrs. Lisa Smith for all of their efforts for the graduate students. I would like to thank Mr. Alireza Chadegani for his accurate and insightful advises on using ABAQUS that I learned a lot from.

Third, I should thank all members of our research group Dr. Mehran Tehrani, Mr. Amir Alipour, Mr. Ayoub Yarri, Mr. Toney Nelson, Mr. Nejib Mesghuni, Mr. Ramez Hajj and Mr. Thomas Haugh whom I learned from the spirits of group research. I thank all of my scientific collaborators including Dr. Said Ahzi, Dr. Akbar Ghazavizadeh and Mrs. Azadeh Sheidaei for their insightful

comments. I sincerely appreciate all of my friends including Mr. Karim Saeid who helped me to enjoy my life in Blacksburg since 2010, in Albuquerque during 2009-2010 and in Wichita during 2008-2009.

Last but not least, hereby my truthful gratitude and love is presented to whom I dedicate this work to: my mother Ezzat, my father Mortaza and my wife Fatemeh for their endless love, support and prayer, and to my siblings Zari and Saeid who always backed me up with their sacrifice.

Masoud Safdari
Winter 2012, Blacksburg

Contents

List of Figures

List of Tables

1

Introduction

1.1 Preliminary Background

1.1.1 Nanomaterials and Nanotechnology

In a general perspective, the science of the design, production, characterization and application of nanomaterials is denoted by Nanotechnology. Nanomaterials can be broadly categorized as structured components with at least one dimension in the range of 1-100 nm. Nanomaterials can be classified by their geometry into zero dimensional like nanoparticles, one dimensional like nanofibers, nanowires and nanotubes, two dimensional like nanoplatelets and three dimensional like fullerenes. In the case of the zero dimensional and the one-dimensional nanomaterials, their surface per unit volume ratios are inversely proportional to their size and, thus, greater surface area can be expected for smaller diameters. Nanomaterials are famous for their enhanced properties such as thermal properties, electrical properties, reactivity, strength, etc. To explain the unusual properties of nanomaterials, two important factors could be acknowledged: their increased surface area per unit volume and their quantum confinement effects (3). It should be mentioned that the quantum effects are occurring because these small species can confine their electrons into their relatively large surfaces.

1.1.2 Nanocomposites

Composites are materials comprising at least two different components aiming to utilize the best properties of each component. A particular type of composites are those in which a

material acts as a filler inside the matrix of another host material. Nanomaterials have been also used as one or more components of the composites and specially as fillers inside ceramics or polymers matrices. Generally the multifunctional materials produced this way are called nanocomposites with emerging application in different fields. The typical characteristics and applications of the macroscale fillers and the nanoscale filler materials are compared in table 1.1. For instance, multi-wall carbon nanotubes (MWCNTs) possess significant electrical conductivity (4) and they can be added to a poor electroconductive polymer and enhance its electrical properties (5). Similarly, graphite nanoplatelets (GNPs) possess astonishing thermal conductivity of 3000 $Wm^{-1}K^{-1}$ (6) and they can successfully enhance the thermal conductivity of a thermal insulator material. Usually, the extreme surface to volume ratios of nanomaterials along with their significant aspect ratios enable them to form large interfaces with the host matrix. The properties of the host matrix are significantly affected in the vicinity of these interfaces. Thus, the large area of interface enhances the macroscopic properties of the bulk host material.

Table 1.1: Comparison between the characteristics of traditional and nanoscale materials (1).

	Approximate Shape	Smallest Dimension (nm)	Aspect Ratio	Elastic Modulus (GPa)	Electrical Conductivity (S/cm)	Thermal Conductivity (W/mK)	Commercial Applications
Traditional Fillers							
Carbon black	agglomerate of spheres	10-100	1-5	...	10-100	0.1-0.4	tires, hoses, shoes, elastomers
Carbon fiber	rods	5,000-20,000	10-50	300-800	0.1-10	100-1000	aerospace, marine, sporting, medical
Carbon graphite	plate	250-500	15-50	500-600	1-10	100-500	gaskets, seals
E-glass	rod	10,000-20,000	20-30	75	...	...	marine, automotive, filtration
Mineral: $CaCO_3$	sphere	45-70	≈ 1	35	...	3-5	paper, paint,
	platelet	600-4,000	1-30				rubber, plastics
Mineral: silica	agglomerate of spheres	8,000-30,000	5-10	30-200	...	1-10	reinforced plastics, thermal insulator, paint, rubber reinforcing agent
Mineral:talc,china clay	platelet	5,000-20,000	5-10	1-70	...	1-10	paper, consumer goods, construction
Nanoscale Fillers							
Carbon nanofiber	tube	50-100	50-200	500	700-1000	10-20	hoses, aerospace, ESD/EMI shielding, adhesives
MWCNT	tube	5-50	100-10,000	1000	500-10,000	100-1000	automotive, sporting, ESD/EMI shielding
SWCNT	tube	0.6-1.8	100-10,000	1500	1000-10,000	1000	filters, ESD/EMI shielding
Aluminosilicate nanoclay	plate	1-10	50-1000	200-250	...	1-10	automotive, packaging, sporting, tires, aerospace
Nano-TiO_2	sphere	10-40	≈ 1	230000	$10^{-11} - 10^{-12}$	12	photocatalysis, gas sensors, paint
Nano-Al_2O_3	sphere	300	≈ 1	50	10-14	20-30	seal rings, furnace liner tubes, gas laser tubes, wear pads

1.1.3 Polymer Nanocomposites

Polymer nanocomposites (PNCs) are special classes of nanocomposites in which the host matrix is a polymeric material. Nanomaterials in the form of nanoparticles, nanofibers or nanoplatelets are usually utilized as the filler phase in a polymer nanocomposite. The addition of minute loadings of nanomaterials (1-5%vol) into a polymer provides property enhancements comparable to those obtained via high loadings of conventional macroscale material (15-40%) (1). Figure 1.1 schematically shows layered silicates in a polymer matrix (3). Depending on how well the polymer chains penetrate in between the nanolayers of the silicates three different materials phases could form. Only when the polymer chains penetrate in between the nanolayers of the silicate to some degree, it can be categorized as a nanocomposite. Lower cost, ease of manufacturing and tunable properties are the main drivers for the popularity of polymer nanocomposites.

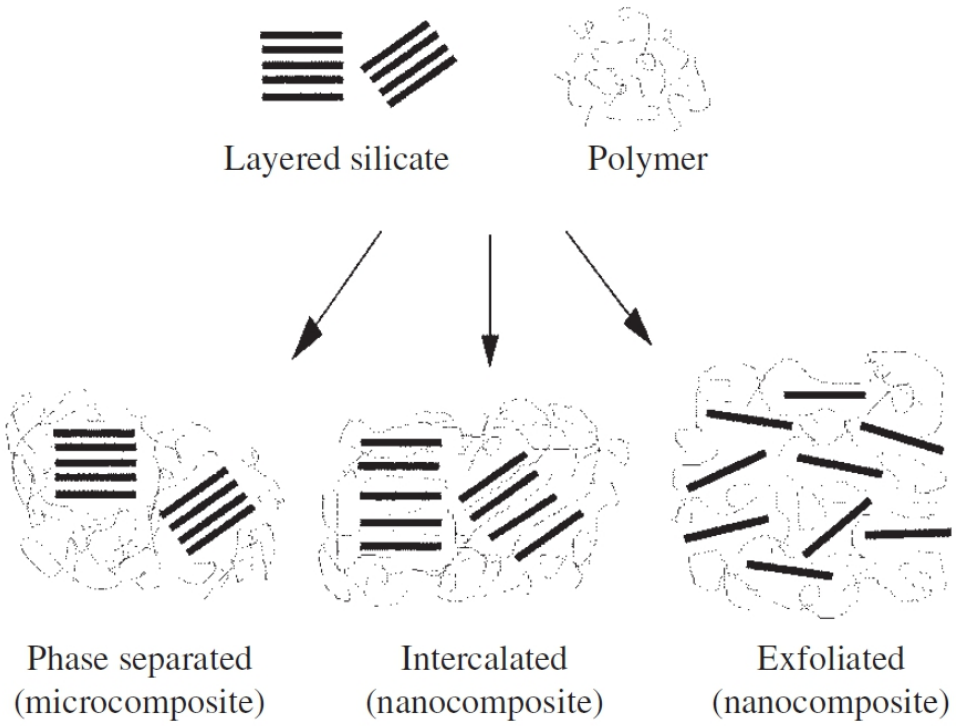

Figure 1.1: Polymer Nanocomposites - Scheme of different types of layered silicate in polymer matrix (3).

1.1.4 The Promise of Nanocomposites

Nanocomposites are well known for their enhanced mechanical, thermal, electrical, optical, chemical and permeability properties. However, in order to harvest these properties at their extremes, several challenges need to be resolved. These challenges include, but are not limited to, the extension of our current understanding of their behavior, development of proper dispersion methods to minimize large-scale disorders, developing proper techniques to control the interface and possibly interphase, managing the end user health and safety concerns and finally reducing their cost. Currently, several research works are tackling these diverse aspects of the nanocomposites. The importance of the nanocomposites can also be measured by the number of the scientific publications and patents (1). Further discussions on the subject of nanocomposites are available in the literature (1, 7).

1.2 Carbon Nanotube Polymer Nanocomposites

1.2.1 Introduction to Carbon Nanotubes (CNTs)

Due to their unusual properties, upon their discovery in 1991 (8), carbon nanotubes (CNTs) have attracted huge interest in the scientific community. The most important properties and features of CNTs are their aspect ratio (up to 132,000,000), extreme Young's modulus (0.2-5 TPa), high mechanical strength (10-150 GPa), diverse range of electrical conductivity (from a semiconductor to 1,000 times more conductive than copper), very high thermal conductivity (from almost an insulator in the radial direction to 10 times more conductor than copper along the axial direction) and low density (1.3-1.4 g/cm^{-3}) (9). These unique properties are tied with their strong sp^2 bonds and their hollow cylindrical structure formed by a single to multi-layers of seamless sheets of graphene. Based on their nanostructure, CNTs can be classified into single wall (SWCNTs), multi-wall (MWCNTs) carbon nanotubes and carbon nanofibers (CNFs). Carbon nanotubes have been synthesized by a variety of methods including arc-discharge generator, laser ablation, chemical vapor deposition (CVD) and high pressure carbon monoxide (HIPCO) conversion method (9, 10). The superior mechanical properties of CNTs (11) have made them a good choice as a filler material for the composite reinforcement purposes (9, 12). Based on the wrapping angle of their graphitic sheet (13)(also know as chirality), SWCNTs could be electrically semiconductor or highly electroconductive (metallic) and MWCNTs could also be classified as very good conductors

of charge carriers (14). Carbon nanotubes have been widely used as the electroconductive filler components in nanocomposites (5). Originated from their unusually high thermal conductivity (15), nanocomposites (16) based on CNTs have been used as good replacement materials for metallic parts in a wide range of industrial applications from power electronics to heat exchangers. Further details about the electrical and thermal properties of CNT-based polymer nanocomposites are provided in the following sections, however, more discussions of the general properties of CNTs can be found in the literature (9, 12, 17).

1.2.2 Electrical Properties of Carbon Nanotubes

1.2.2.1 Percolation Threshold

The addition of very small loadings of CNTs (0.1 wt% or less) to a low electroconductive polymer matrix enhances its electrical conductivity (σ) by several orders of magnitude. The minute loading maintains other desirable performance aspects of polymers such as transparency. This interesting feature is useful for various applications including electrostatic dissipation (electrostatic painting), electromagnetic interference (EMI) shielding, transparent conductive coatings and printable circuit wiring (12). For an insulating polymer loaded with CNTs, the transition to the electroconductive state is depicted by a sharp increase in the electrical conductivity (by many orders of magnitude) when the filler loading exceeds a critical value known as the *percolation threshold*. Physically, when the volume fraction of CNTs exceeds the percolation threshold a three dimensional cluster of CNTs is formed and could span the volume of the specimen. The percolation threshold of CNTs in different polymer matrices has been studied thoroughly in the literature (5). Generally, the percolation threshold of CNT/polymer nanocomposites is much lower (18) than that for composites containing conventional conducting fillers, such as metallic particles, carbon black or carbon fibers, due to their large aspect ratio. However, it is generally a function of many parameters including the CNT type, the synthesis method, the state of dispersion and alignment (5).

1.2.2.2 Electrical Conductivity

The effect of the addition of functional groups to CNTs on the percolation threshold has shown contradictory results in the literature. It is universally accepted that chemical fictionalization disrupts the π-conjugations of nanotubes and consequently reduces the electrical

conductivity of the CNTs (12). However, at the same time, the functional groups assist the CNTs to disentangle and thereby facilitate the dispersion (19). The good dispersion of CNTs consequently reduces the percolation threshold which outweighes the reduced electrical conductivity. The alignment of CNTs in the host matrix also affects the percolation threshold and the electrical conductivity. The study of CNTs alignment effect has showed that only certain levels of SWCNTs alignment produce higher conductivity compared to their isotropic dispersion (20).

1.2.3 Thermal Properties of Carbon Nanotubes

1.2.3.1 Thermal Conductivity

Highly thermally conductive nanocomposite have potential applications in optical, electronic and energy conversion devices. According to the experimental measurements, individual SWCNTs (21, 22) and MWCNTs (23) can be classified as excellent thermal conductors (more than 3000 $Wm^{-1}K^{-1}$ at room temperature). Basically, CNTs perfectly conduct thermal energy through atomic vibrations or phonons, however, because of the phonon scattering the high thermal conductivity of CNTs is temperature-dependent with an asymptote at $320°K$ (22). According to these observations, CNTs are good candidates to be utilized as filler for the enhancement of the thermal conductivity of polymer matrices as they do with the electrical conductivity. This early expectation was shown to be untrue (12). The low loading of CNTs only show modest improvement of the effective thermal conductivity ($100 - 300\%$ improvement compared to the neat resin) for their nanocomposites (12). One reason for this observation could be the lower contrast between the thermal conductivities of CNTs and typical polymeric materials (in the order of $\times 10^3$) compared to the contrast in the electrical conductivity (in the order of $\times 10^{15} - 10^{19}$).

1.2.3.2 Interfacial Resistance

The effect of the different parameters of CNTs (CNT type, aspect ratio, dispersion state, low-contrast etc.) on the thermal conductivity of CNT/polymer nanocomposites are discussed in the literature (24). In addition to these, the the exponentially low thermal conductance of the CNT/host interface (approximately 12 $MWm^{-1}K^{-1}$ (25)) and even between CNTs themselves (26) are two main reasons to restrict the effective thermal conductivity of their

nanocomposite to the lower values compared to what is expected form the rules of mixture laws. The large interfacial thermal resistance, also known as Kapitza's resistance (27), is mainly caused by the large difference between the frequency of the phonon modes of the CNTs and their surrounding (12). One study (24) suggests that MWCNTs are more promising for the improvement of the thermal conductivity because of their relatively lower interface area compared to SWCNTs and the existence of the shielded internal layers which facilitates phonon transfer mechanism. Functional groups can also be chemically grafted onto the surfaces of CNTs to form covalent bounds and improve interfacial conductance, however they also reduce the intrinsic thermal conductivity of the CNTs (28, 29).

1.3 Graphite Nanoplatelet Polymer Nanocomposites

1.3.1 Introduction to Graphite Nanoplatelets (GNPs)

1.3.1.1 Graphene

Upon its discovery in 2004 (30), free-standing single layer of graphene has been in the center of attention of the scientific society. Graphene is a single 2D layer formed from densely packed carbon atoms held together with strong sp^2 bonds in a honeycomb lattice (31). As shown in figure 1.2, it could be interpreted as the building block of all other allotropic forms of nanoscale graphitic materials including fullerenes, CNTs and GNPs. Graphene has extraordinary properties including Young's modulus of 1 TPa, strength of 130 GPa, thermal conductivity of 5000 $Wm^{-1}K-1$, electrical conductivity of 6000 Scm^{-1} and ultra high surface area (theoretical limit: 2630 m^2g^{-1}) (32). These significant properties can potentially improve the electrical, thermal, mechanical and gas barrier properties of their nanocomposites. Generally, single layer of graphene can be produced via both bottom-up and top-down approaches. Bottom-up approach are mainly epitaxial growth methods (33), chemical vapor deposition methods (34) and methods based on unzipping of CNTs (35). Top-down synthesis methods are based on exfoliation of graphite which are more suitable for mass production purposes. A good review on these methods can be found in the literature (32).

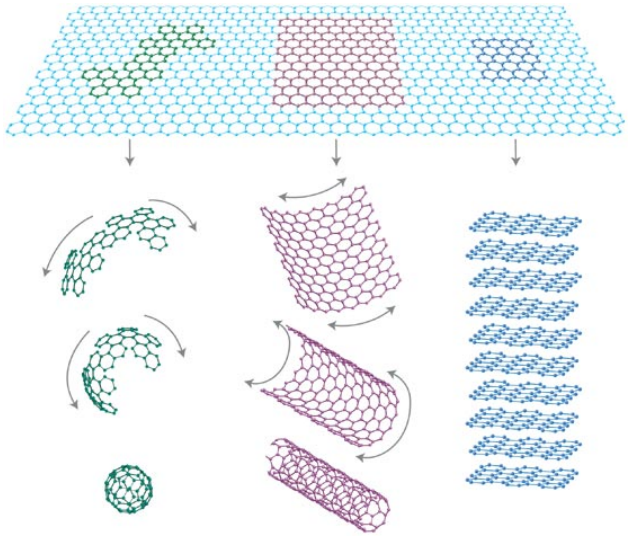

Figure 1.2: Graphene Nanostructure - Schematic of graphene as a building block of different graphitic structures taken from (31).

1.3.1.2 Graphite Nanoplatelets (GNPs)

Graphite nanoplatelets (GNPs) are made form graphene sheets stacked on top of each other and separated by 3.8 Å forming a platelet morphology. These stacks are held together by interatomic Van der Walls forces. In general, GNPs possess almost identical properties of graphene sheets inside their graphitic planes and much different properties along their stacking direction (2). Table 1.2 compares the physical properties of GNPs with those for SWCNTs and carbon nanofibers (CNFs). Similar to graphene, GNPs can be produced by both bottom-up approaches from restacking of single-layer high surface area graphene sheets (36) or top-down approaches from incomplete exfoliation of graphite. Graphite nanoplatelets are usually prepared from the intercalation and exfoliation of graphite flakes in highly concentrated acids at high temperatures (37, 38, 39). Graphite nanoplatelets are structurally more stable than single-layers of graphene, less expensive to produce and more versatile in size and aspect ratio. These properties, combined with the ease of handling, constituted the GNPs as suitable filler contents for nanocomposites.

1.3.2 Electrical Properties of Graphite Nanoplatelets

High aspect ratio GNPs can be readily incorporated into polymeric matrices. Similar to CNTs, relatively low contents of 2D graphene sheets ($\approx 0.1\%vol$) can form 3D networks

Table 1.2: Estimated physical properties of SWCNTs, Carbon nanofibers (CNFs) and GNPs (2).

Property	**Single-walled CNTs**	**Carbon Nanofibers**	**GNPs**
Specific Gravity (g/cm^3)	0.8	$1.8(AG)^a - 2.1(HT)^b$	$1.8 - 2.2$
Elastic Modulus (TPa)	≈ 1 (axial direction)	$0.4(AG) - 0.6(HT)$	≈ 1 (in-plane)
Strength (GPa)	$50 - 500$	$2.7(AG) - 7.0(HT)$	$\approx 100 - 400$
Resistivity ($\mu\Omega cm$)	$5 - 50$	$55(HT) - 1000(AG)$	50 (in-plane)
Thermal Conductivity ($Wm^{-1}K^{-1}$)	Up to $2,900$ (estimated)	$20(AG) - 1950(HT)$	$5,300$ (in-plane) $6 - 30$ (c-axis)
Magnetic Susceptibility (emu/g)	22×10^6 (radial) 0.5×10^6 (axial)	N/A	22×10^6 ($\perp$ to plane) 0.5×10^6 ($\parallel$ to plane)
Thermal Expansion (K^{-1})	Negligible in the axial direction	-1×10^{-6} (HT: axial)	-1×10^{-6} (in-plane) 29×10^{-6} (c-axis)
Thermal Stability ($^\circ C$)	> 700 (in air) 2800 (in vacuum)	$450 - 650$ (in air)	$450 - 650$ (in air)
Specific Surface Area (m^2/g)	Typically $10 - 200$ Up to $1,300$	$10 - 60$	Typically $100 - 1,000$ up to $> 2,600$

[a] AG: as grown
[b] HT: Heat treated (graphitic)

of percolating clusters to conduct electricity (6, 37). Several groups studied nanocomposite comprising GNPs embedded in a variety of polymer matrices (32, 40). Generally, GNP-based electroconductive polymer composites possess properties identical to the CNT-based nanocomposites with lower processing expenses which suits several industrial applications. Unlike CNTs, chirality is not an effective factor on the electrical properties of GNPs. Theoretically, for identical aspect ratio, disk-shaped particles percolate in volume contents two folds more than rod-shaped particles (41). It is worthwhile to mention that GNPs possess high rigidity originating from their stack shaped structure which improves their out-of-plane mechanical stiffness and reduces large deformations including buckling and folding during processing steps (42). This could be beneficial in reducing their percolation threshold. In one study, it was observed that GNPs can also affect the crystallinity of the polymer matrix which can, consequently, reduce the percolation threshold (43). The addition of functional groups to GNPs to enhance the electrical conductivity of GNP/polymer nanocomposite has also been studied, however, deteriorating effects have been reported (44).

1.3.3 Thermal Properties of Graphite Nanoplatelets

Significant intrinsic thermal conductivity of graphene and GNPs can enhance the thermal conductivity of the nanocomposites with several applications in power electronics, thermal pastes, and miniaturized electronic devices etc. (32). The addition of minute amounts of GNPs to a polymeric matrix enhances it thermal conductivity significantly (37). However, analogous to CNTs, GNPs can not enhance the thermal conductivity exponentially owing to the lower contrast between the filler/polymer properties and the mismatch between the vibrational modes of filler-filler and filler-polymer interfaces which result in poor coupling and large Kapitza resistance (45). However, a number of investigations have shown that 2D GNPs are better phonon-conductors than 1D CNTs (38, 46, 47). The addition of functional groups and covalent bounding can also enhance the GNP/polymer interfacial thermal conductivity through the reduction of the acoustic phonon scattering (44), however, like CNTs it also reduces the intrinsic GNPs conductivity. Improvement of the thermal conductivity by adding GNP has been reported for a number of polymeric matrices (32). The enhancement in the properties is reported to be a function of the dispersion, alignment and the degree of exfoliation of the GNPs (38). Highly aligned GNPs can enhance the thermal conductivity along their alignment direction and produce macroscopically anisotropic properties (48, 49).

1.4 Processing of Nanocomposites

1.4.1 Introduction

Polymeric matrices are mostly thermosets or thremoplastics. Several processing methods are available for both thermoset and thermoplastic polymers loaded with nanomaterials. Usually different processing techniques are developed to address following aspects:

- Control the deagglomeration of nanoparticles bundle
- Control the dispersion state
- Control the alignment in case of 1D, 2D or 3D nanoparticles
- Control the properties of the nanoparticle/polymer interface
- Protect the nanoparticles from damage and reserve their aspect ratios

Depending on their synthesis process, commercially available nanospecies are usually in the form of bundles of highly entangled clusters with some accompanying unwanted impurities (50). For instance, CNTs and GNPs are usually accompanied by metallic residuals and some carbonaceous particles such as amorphous carbon, fullerenes and graphites (by-products of the synthesis process)(50). Therefore, some preprocessing of the nanoparticles is usually required to purify them from contaminations, deagglomerate them to some degree and sometimes functionalize their surfaces. For purification purposes the most common methods are acid treatments (for eliminating metallic residues (51)), thermal annealing (for removing amorphous carbons (52)) and mechanical techniques. For disentangling of nanoparticles variety of methods could be utilized, however, in the case of CNTs ultrasonication in a solution is the most utilized method (53). Functionalization of the nanoparticles serves different purposes (54), it is mostly advised for the improvement of the interface bounding and increasing the performance of the nanocomposite (19). Functionalization techniques have two general categories including covalent functionalization (19) by functional groups and non-covalent (physical) functionalization by surfactants (55). Nanocomposite processing methods can be generally divided into the following groups:

- Solution processing

- Melt-mixing
- Other methods

In the following sections, brief surveys for each of these nanoparticle/polmer matrix processing methods are provided.

1.4.2 Solution Processing

In this method either the polymer or nanoparticles are dissolved into a proper solvent and mixed to form a homogenous solution and then the solvent is evaporated or removed by filtration to leave the final nanocomposite for further drying and curing steps. Sonication and homogenization methods of nanocomposites are usually more effective for low viscosity media (56). Thus, the main advantage of the solution-based methods is to facilitate the mixing and dispersion of nanoparticles into the polymer matrix through reducing its viscosity (50). The solvent is usually selected based on the polymer and could be both aqueous or organic (50). A variety of different CNT and GNP-based nanocomposites with both thermoset and thermoplastic polymers have been processed by this method (32, 50). This method has been utilized to intercalate polymer chains between CNTs and GNPs and process polymeric thin-films with enhanced mechanical properties (57). Other methods such as melt-mixing can also be combined with solution processing to improve some aspect of the processing (58).

1.4.3 Melt-Mixing

Melt mixing methods (also known as melt blending) are specially developed for thremoplastics (50, 59). In these methods, nanoparticles are added into the molten polymer to be homogenized and casted into a mold. Extrusion and injection molding are two main branches of melt-mixing techniques. These processes are originally developed for industrial scale production of plastics and, therefore, are cost-effective, quick and simple (50). Because of their solvent-free nature, they make less contamination compared to the solution processing methods. One main advantage of these methods is their ability to preserve the nanoparticles from damage (50). However, the nanoparticles should be resistant to the elevated temperatures encountered with these methods (59). Usually high shear mixing should be employed to overcome the high viscosity of the mixture occurring during processing of

high aspect ratio nanoparticles and also to improve the dispersion. Because of its shear flow nature and its special alignment control tools, more control over the alignment of the CNTs (60) and GNPs (61) is achievable by this method. A number of polymers nanocomposites have been successfully processed by this method (50).

1.4.4 Other Methods

A number of other methods for processing polymer matrix nanocomposites have been cited in the literature (50, 59). Among them the in-situ polymerization is practiced more commonly. In this technique, nanoparticles first get dispersed with a monomer and then the mixture is polymerized. It is believed that in-situ polymerization improves dispersion and integration between phases (50). This method is widely utilized for intrinsically conductive polymers such as polypyrrole (PPy) (62) and polyaniline (PANI) (63). Methods based on chemical vapor deposition (CVD) and electrochemical processing are examples of other processing methods (50).

1.5 Simulation and Modeling

1.5.1 Introduction

The importance of the polymer nanocomposites and their impact on science and industry was discussed earlier. Further development of these nanomaterials calls for fundamental understanding of their behavior. Modeling and simulation techniques have always been utilized as powerful tools to address fundamental questions about the physical behavior of different composite systems. Plethora of research have been carried out to investigate polymer nanocomposites (64). Because of their hierarchical nature, usually a number of phenomena at different time and length scales occurring simultaneously within these nanomaterials. Therefore, seamless coupling between these different time and length scales demands advanced multiscale computational techniques. A successful computational model for this purpose should cover up to three disparate scales including the molecular scale, microscale and macroscale. So far several computational and mathematical methods were developed to cover each of these length scale. These methods can be roughly divided into:

- Molecular-scale: molecular dynamics (MD) and Monte Carlo (MC) methods

- Microscale: dissipative particle dynamics (DPD), lattice Boltzmann (LB), Brownian dynamics (BD) and time-dependent Ginzburg-Landau method (TDGL)
- Mesoscale and Macroscale: micromechanics, statistical continuum mechanics, continuum mechanics and finite element methods (FEM)

For each of these methods a chapter is needed to cover only the basics. Interested readers are referred to the relevant literature (e.g. (64, 65)). Molecular scale methods are developed to study the time-evolution of a system of atoms based on a set of initial conditions and a potential field (or force filed) that describes the interaction between these atoms (66). Monte Carlo methods are essentially studying the same system, however, a set of random displacements is assigned to each atom in the system and instead of using time-integration schemes to evaluate the trajectory, the system evolves by decisions made according to a probability distribution function (67). Microscale methods are mainly developed to bridge the molecular scale to the continuum scale (64). For instance, dissipated particle dynamics (DPD) also studies the interaction and the time-evolution of a system of particles, however, each particle represents a group of atoms and thus it is able to capture larger time and length scales phenomena (e.g. bulk flow) compared to MD and MC (64). Mesoscale and macroscale methods consider the system as a continuum medium and apply conservation laws and the second law of thermodynamics. Conservation laws are the statements of the conservation of mass, linear (and angular) momentum and energy of the system which should be applicable to the system all the times. These basic laws are usually coupled with a constitutive equation (material law) and the equations of the state in order to solve a continuum problem.
In the micromechanics-based approaches, the system is replaced by a set of infinitesimal material elements denoted by representative volume element (RVE) (68). A RVE is assumed to be large enough to statistically represent the local behavior of the system (and, therefore, to encompass the smallest constituent of the system). One of the most important advantages of the micromechanics methods is their ability to relax the continuity conditions which empowers them to encompass the microstructural details of the system.
The finite element method (FEM) is a numerical method to obtain approximate solution to a boundary value problems (BVPs) of time-dependent nature. The behavior of materials with all types of discontinuity and non-linearity have been successfully simulated with FEM. In this method, the system is described by the variational principles and the material's behavior is described by a constitutive law (69). A number of finite elements (sub domains) with a variety of possible shapes are assembled together to represent the solution domain. In each

element the solution is calculated exactly at the nodes and approximated by an interpolation scheme inside the element.
In the following sections, brief reviews of the analytical and computational methods developed to model the electrical and thermal properties of polymer nanocomposites are provided with an emphasis on the most recent studies on CNT and GNP-based systems.

1.5.2 Electrical Properties

1.5.2.1 Charge Carrier Transport Mechanisms

The process of charge carrier transport can be divided into two steps including the injection of charge carriers into the materials and the motion of charge carriers through the material. The injection could be explained by Fowler-Nordheim or Tichardson-Schottky transmission processes (70). The charge carrier motion through the material could be characterized into hopping, tunneling, ballistic transport, diffusion or metallic conduction type (70, 71, 72). Generally, four different conduction aspects in a polymer composite materials exist: the conduction in the polymer matrix, the conduction in the filler phase, the conduction between fillers and the conduction from matrix to filler and vice versa. For composites with filler loading below the percolation threshold, usually the mean separation distance between the fillers is larger than the tunneling distance (at least more than 10 nm). In this scheme the conduction is governed by the intrinsic polymer conduction mechanism and the filler loading plays minor effect.
Second scenario is for the composites in which the mean particle-particle distance is in the order of $d \leq 10\ nm$. In this case, the electrical tunneling can occur between the neighboring filler particles (73) and the tunneling current can be described by equation 1.1.

$$j_{tunneling} = AE^n exp(-\frac{B}{E}) \tag{1.1}$$

in this equation, E is the applied electric field, B is the energy barrier between the polymer and the filler material and the exponential term represents the transition probability of charge carriers from the filler into the polymer and vice versa. The electrical current can also be described alternatively by a hopping mechanism (i.e. electron-hole separation) (74)

and through equation 1.2.

$$j_{hopping} = A_R T^2 exp(-\frac{K E^{1/2} \Phi}{k_B T}) \tag{1.2}$$

In this equation, $A_R = 1.2 \times 10^6\ A/K^2 m^2$ is the Schottky-Richardson constant, A, B, b and K are constants, Φ is the work function of the filler material, k_B is the Boltzmann constant and T is the temperature (in Kelvin). Finally, at high filler volume contents the conducting filler particles are in close contact and they form continuous conduction pathes. In this case, the conduction mechanism is dominated by the filler material properties.

1.5.2.2 Statistical Percolation

A number of analytical models have been developed to explain the low percolation threshold of CNT/polymer nanocomposites (5, 20, 75). Most of the early efforts to model the percolation behavior are based on the excluded volume approach (76). The excluded volume approach was originally developed to explain the percolation threshold of the statistically dispersed non-spherical conductive particles. This concept interrelates the percolation threshold of the different conductive particle geometries to their excluded volume instead of the volume fraction (5, 76). The excluded volume ($< V_{ex} >$)is defined to be a volume around an object in which the center of another identical shaped object can not penetrate into it (77). A number of studies based on the excluded volume approach tried to explain the effect of the filler shape (78), size and aspect ratio (76, 79) on the percolation threshold. According to these studies the percolation threshold is inversely proportional to the excluded volume. These efforts are based on the statistical continuum theory which usually assumes random distribution of the particles inside the polymer matrix. The predicted percolation threshold of the filler by these models is denoted by the *statistical percolation threshold*. Statistical percolation law usually predicts a scaling law of the form equation 1.3 for the electrical conductivity (σ).

$$\sigma \propto (\phi - \phi_c)^t \tag{1.3}$$

In this equation, ϕ_c is the percolation threshold, t is the critical exponent. In earlier efforts, it was assumed that the critical exponent represents the dimensionality of the percolating

system which is calculated to be $t \approx 1.33$ for two and $t\epsilon(1.65 \sim 2.00)$ for a three dimensional system (80, 81) and more than 2.00 for more complex systems. The increasing value of t is also related to the increasing tunneling barrier between the fillers (80, 82) which simultaneously reduces the maximum electrical conductivity as well. However, lately the experimental observations critiqued this equation and have shown that it is only valid for the concentration range very close to the percolation threshold (5). The percolation theory is also limited to the cases in which either the host matrix has zero conductance or the filler has zero resistance (70).

1.5.2.3 Dynamical Percolation

A number of experimental observations (18, 83, 84) have shown that the predicted statistical percolation threshold could be orders of magnitude higher than the actual values. The possibility of nanoparticles manipulation by shear forces inside the polymer matrix during processing and the formation of percolating networks in even lower volume loading compared to the statistical percolation threshold has also been studied (85). Similar studies also considered the effect of the electric forces (86) and the magnetic forces (87) on the promotion of particle movements and reduction of the percolation threshold. The percolation threshold found this way; by considering the possibility of particle manipulation, is denoted by the *dynamic (or kinetic) percolation threshold* (85). Modeling of the dynamic percolation threshold is a very complex process. Typically, mesosclae simulation techniques based on DPD approach have been utilized for this purpose (88, 89, 90). Usually these approaches add another dimension to a more realistic representation of the percolation phenomenon.

1.5.2.4 Geometric Factors and Alignment

Among the different geometrical factors, the filler aspect ratio is the most dominant in the determination of the percolation threshold. Some models based on the average interparticle distance (IPD) concept were developed to explain this observation for both CNT and GNP based nanocomposites (75, 91). Electron microscopy images for CNT/polymer nanocomposites revealed the fact that CNTs embedded into a polymer matrix are generally wavy and curved (92). This is mainly because of their high aspect ratio and low bending stiffness. A number of researchers tried to consider the effect of waviness within simulation and study its effect (93, 94, 95). According to all of these studies, by considering the waviness, the

percolation threshold could be increased roughly to twice its value for straight CNTs. The effect of alignment of the filler particles in the matrix was also studied by a number of investigators (96, 97) and it was shown that the percolation threshold of isotropically dispersed particles is lower than that when they have preferred orientation.

1.5.2.5 Entanglement and Agglomeration Effects

Some models are proposed in the literature to explain the effect of the agglomeration of the particles on a polymer composite (75, 98, 99). These studies attempted to simplify the agglomeration geometrically and probe its effect on the percolation and the electrical properties. Even though these models may be of interest from the engineering perspective, they deliver little or no information about the physical nature of the agglomeration problem. Thermodynamically, the formation of the agglomerates is a favorable process at multiple length scales. A combination of strong dispersive interactions between the particles and polymer chains and the attraction forces between the adjacent particles (of entropic origin) control the agglomeration and clustering. Knowing this, a time-evolving model which describes the formation and growth of the agglomerates and clusters is a more realistic one. In one study, two rheological and conductivity models were combined to explain the cluster formation (100). From that study, it was argued that the percolation threshold can be influenced by the agglomeration, however, more fundamental studies are still required to explain this phenomenon precisely.

1.5.3 Thermal Properties

1.5.3.1 Basic Considerations

Several models were developed to explain the thermal conductivity of traditional polymer composites (16, 101). Most of these efforts are seeking to find closed form relations for the effective thermal conductivity of the composite. Thermal conductivity is one of the transport properties of a material. Generally, transport properties are coefficients defining the ratio between a flux and the directional gradient of the driving force. In the case of thermal conductivity, the flux is the heat flux (q) and the directional driving force is the temperature gradient (dT/dx). Mathematically, the definition of the thermal conductivity can be given

by equation 1.4.

$$k = q/(dT/dx) = (Q/A)/(\Delta T/x_0) \tag{1.4}$$

In this equation, q is the rate of heat flow (Q) across a given cross section (A) and x_0 is the distance. Most of the developed theories explain the effect of the filler on the thermal conductivity of the composite. The shape and orientation of the filler particles significantly influence the effective thermal conductivity. Therefore, most theoretical treatments are usually valid for only a specific particle geometry and, hence, they can be classified by the filler shape. The possible scenarios are roughly spherical fillers, flakes, irregular shaped particles, short fibers, long fibers and continuous fibers (101). It should be noted that most of these efforts are based on the following assumptions (101):

- The interface between the matrix and the particulate filler is continuous and void-free.
- The composite only comprises a matrix and a dispersed particulate phase (two-phase).
- The size, shape and spatial distribution of the dispersed phase are known and unique for all the particles.

It is beyond the scope of the following review to consider all of the theoretical approaches to evaluate the thermal conductivity of composites. However, the fundamentals are outlined in following sections.

1.5.3.2 First-Order Models

Two basic models represent the upper bound and the lower bound of the thermal conductivity are known as the rule-of-mixtures model (also known as the arithmetic average) and the series model (also known as the harmonic average), respectively. Equation 1.5 depicts the rule-of-mixture model in which it is assumed that each phase contributes independently (parallel configuration).

$$k_c = k_p\Phi_p + k_m\Phi_m \tag{1.5}$$

In this equation k_c, k_p and k_m are the thermal conductivities of the composite, particle and matrix, respectively and Φ_m, Φ_p are the volume fractions of the matrix and particles respectively. The upper bound model assumes perfect bounding between the particles in a fully percolated network and, therefore, it usually overestimates the effective thermal conductivity. In contrast, the lower bound model assumes no contact between the particles and, therefore, the contribution of each particle is limited to the matrix phase around it (series configuration). Equation 1.6 represents the lower bound prediction for the thermal conductivity of the composite.

$$\frac{1}{k_c} = \frac{\Phi_p}{k_p} + \frac{\Phi_m}{k_m} \tag{1.6}$$

It should be noted that most of the theoretical predictions for the thermal conductivity fall between the lower-bound and upper-bound predictions. These two models are referred to as first order models (101).

1.5.3.3 Second-Order Models

Lower bound predictions are usually closer to the experimental results (101) and therefore a number of models were developed based on this approach. Inherently, most of these models are based on some complex averaging techniques and the fillers are treated as noninteractive isolated particles (non-contact conditions)(101). These models were developed to provide a better estimation for the thermal conductivity of the composites. Generally, the thermal conductivity of a particulate-matrix system can be expressed by the statistical summation of the perturbations around each filler particle. Mathematically, the localized average thermal conductivities are related to the overall thermal conductivity by a series expansion as described by equation 1.7 (102).

$$k_c/k_m = 1 + \sum_{n=1}^{\infty} A_n[(k_f - k_m)/k_m]^n \tag{1.7}$$

In this equation, A_n describes the local field and it is related to the filler particle shapes (microstructure). A truncated version of this equation limited to only the first three terms can readily provide an estimate of the thermal conductivity of the composite. However, this truncation is only useful when there is a limited contrast between the properties of the

filler and matrix phases. For higher contrasts, more terms are needed and, therefore, more information about the microstructure of the composite is required. The main drawback of the statistical approaches is that they demand more information about the microstructure of the composite than is usually available (101). One way to bypass this shortcoming is to develop relationships for upper and lower-bound of the thermal conductivity which are not requiring comprehensive knowledge of the microstructure. Several second-order models are developed based on this approach. They are called second order because they can be derived from the equation 1.7 up to the second coefficient (A_2). These models include Hashin and Shtrikman (103), Hamilton and Crosser (104), Hatta and Taya (105) and Nielson (106). The equation that Nielson (106) developed is appearing to be identical to the Hashin-Shtrikman equation, however, it additionally considers the maximum packing ratio in the model which increases its accuracy specially for higher volume contents of the filer particles (more than 30%) (101). Higher order models were also developed to provide better estimates of the thermal conductivity, however, they require more information about the microstructure (101). It should be mentioned that all of these models are valid up to the network formation limit in which the particles start to form close interactions and, thus, they usually provide good estimation of the thermal conductivity for lower volume contents and lower aspect ratio filler materials. For higher concentrations of the filler particles; where contacts are likely to happen, some models have been developed in the literature (107, 108). However, it should be noted that apart from the contact formation considerations (discussed in next section), it appears that the heat transfer mechanism is not changing fundamentally in these cases (101).

1.5.3.4 Interfacial Resistance

The addition of a particulate filler into a matrix phase for the purpose of thermal conductivity enhancement introduces a new phase to the composite known as the interface. In thermal conductivity nomenclature, the interface is the shared particle-matrix surface which usually introduces some resistance to the thermal conductivity known by the Kapitza resistance. The interface resistance could have remarkable effect on the effective thermal conductivity of the composite (109, 110). Several researchers tried to develop models for the thermal conductivity of composites by taking into account the interfacial thermal resistance for different particles shapes (109, 110, 111, 112, 113). Even though in all of these efforts particles are assumed to be isolated by the matrix material, they provide closer fit to the

experimental measurements than the models without interfacial resistance. This fact is more pronounced when nanoscale particulate filler phases, with high surface areas, are utilized in the composite.

1.5.3.5 Finite Element Modeling

The finite element method has been utilized to study the thermal properties of CNT/GNP/ polymer nanocomposites. The lack of the thermal percolation threshold in CNT-based composites has been modeled and successfully explained via finite element modeling (114). A number of studies are available in literature in which the effective thermal conductivities of CNT/polymer and GNP/polymer nanocomposites are investigated through FEM methods (115, 116, 117, 118). From these studies it was concluded that even continuum based finite element method can successfully predict the thermal properties of these nanocomposites.

1.6 Research Objectives

A brief review of the subject of polymer nanocomposites with a focus on their transport properties namely the electrical and thermal conductivities was provided in this chapter. From this review, many aspects of these nanomaterials remain almost unknown. Among them, the transport properties of the polymer nanocomposites including the electrical and thermal properties lack comprehensive understanding. This dissertation is focused on developing some fundamental understanding of the transport properties of polymer nanocomposites loaded with CNTs and GNPs. For this purpose, novel models and simulation strategies are developed aiming to study the nanocomposites under more realistic conditions. Throughout this study, the proposed models are compared with other well-established models in the literature. In order to validate the proposed models, their predictions are compared to the available experimental results reported in the literature. Furthermore, an experimental investigation is carried out to validate the proposed models under more controlled conditions. The technical objectives of this dissertation can be briefly summarized as follows:

1. Develop more realistic quantitative and qualitative models to predict the electrical and thermal properties of polymer nanocomposites filled with CNTs or GNPs.

2. Verify the proposed models with their well-established counterparts in the literature, whenever possible, and discuss the possible source of discrepancies.

3. Extend the proposed models to predict the electrical and thermal properties of hybrid polymer nanocomposites comprising both CNTs and GNPs (multiphase model).

4. Study the advantages of the hybrid polymer nanocomposites comprising both CNTs and GNPs.

5. Experimentally investigate the electrical and thermal properties of hybrid polymer nanocomposites comprising both CNTs and GNPs.

6. Validate the above proposed models with the in-house experimental studies results.

1.7 Dissertation Outline

In this dissertation, the first chapter outlines the current state of the art about the electrical/thermal transport properties of polymer nanocomposites comprising CNTs and GNPs in light of available literature. In the second chapter, the effect of the tunneling phenomena on the electrical properties of these nanocomposites is investigated. Based on this investigation, in the third chapter, a comprehensive model for predicting the electrical conductivity of these polymer nanocomposites is introduced and discussed. In the forth chapter, an attempt to introduce a proper model and simulation method to computationally investigate the thermal properties of the aforementioned polymer nanocomposites is presented. In the fifth chapter, the computational models developed in chapters three and four are employed to explore the possible benefits of the hybrid CNT/GNP/polymer nanocomposites. To validate the above mentioned models a comprehensive experimental study is carried out in the chapter six. In chapter seven of this dissertation, reported experimental findings are utilized to validate the proposed models. The final chapter of this dissertation was devoted to some concluding remarks and recommendations of future work. Each chapter in the thesis starts with a short backgrounds relevant to it. The second part of each chapter is devoted to new contributions along with the proposed methodology for the study. Finally, some results are provided along with their detailed discussions.

2

Incorporation of Electrical Tunneling

2.1 Introduction and Scope

Understanding the proper charge carrier mechanism is a crucial step in the modeling and simulation of the electrical properties of nanocomposites. In this chapter, the effect of the electrical tunneling mechanism on the electrical properties of conductive nanocomposites is comprehensively examined. For this purpose, a new approach in computational modeling of the nanoparticulate composite materials is introduced. Some basic level of details about the computer code developed to implement the proposed method is discussed as a basis for further developments in the following chapters. In this chapter, all virtual experiments are carried out for GNP-based nanocomposites, however, the proposed model is valid for CNTs as well.

Insulating polymers filled with GNPs constitute a new class of multifunctional engineering materials which are superior to the pristine polymer matrix in the sense of electrical conductivity (40, 119). Amongst the many potential applications for such materials are the electrostatic discharge (ESD) and electromagnetic interference (EMI) shielding.

According to the experimental observations, the electrical conductivity of polymers loaded with conductive additives typically shows a classical S-curve behavior with the volume fraction of fillers (40). Based on these observations the conductivity increases monotonically from almost zero filler loading up to a critical transition limit. From experimental observations, this limit is a narrow range of volume fractions which is called the percolation threshold (ϕ_c). At the percolation threshold (ϕ_c), which may vary slightly from one experiment to

another, the conductive ingredients start to percolate within the sample, thereby, the conductivity undergoes an abrupt increase (of several orders of magnitude). At post percolation threshold levels, the electrical conductivity again exhibits a rather weaker dependency on the volume fraction of the conductive additive. This behavior is attributed to the establishment of multiple continuous paths throughout the medium beyond the percolation threshold (40).

A crucial phenomenon in the study of conductive polymers is the tunneling effect. The term *tunneling* refers to the jump of a charge carrier from one conductor to a neighboring one and in general includes both jumps over a potential barrier and quantum mechanical tunneling (120, 121, 122). In systems where the particles are not in contact physically, but do touch electrically, the measured finite macroscopic conductivity is mainly attributed to the existence of the interparticle tunneling. An evidence for this arguments is the temperature and frequency dependence of the electrical conductivity of polymer composites (120). Therefore, in a composite material containing conductive fillers, the electrical conductivity may as well depend on the average distance between the particles. In a recent study, Belberg (123) addressed this issue with greater detail. Hence, the percolation threshold for the conductive filler-based composite materials should also be a function of the topological aspects of the particles.

The basic problem of an object percolation in a medium has already been investigated thoroughly by other researchers (see e.g. (41, 91, 96, 97, 124, 125, 126)) but in the present study the percolation threshold of a polymeric composite filled with conductive GNPs is reexamined using a new computational technique. The details of the proposed Monte Carlo-based method are provided in Section 2.2. In a similar study carried out by Li and Kim (91) it was assumed that GNPs are perfect thin disk-shaped particles homogenously distributed in the matrix. Then a specific interparticle distance (IPD) with a new definition was adopted to represent the electrical percolation. Afterwards, the electrical percolation has been studied as a function of the geometry and the volume fraction of the conducting particles. Comparison with other results (e.g Kuila et. al. (40)) indicates that IPD model yields unsatisfactory results. In a step forward in this study, the dispersion process can be switched between penetrable dispersion, in which the particle penetration is allowed and impenetrable dispersion in which no physical penetration between the particles is allowed. Analysis of the percolation threshold carried out by the proposed method is believed to yield more realistic results. By applying this method, the effect of different aspect ratios GNPs as well as the tunneling distance on the percolation threshold is investigated in subsequent

sections of this chapter. The results derived by this analysis are discussed next and compared with other relevant studies in Section 2.3.

2.2 Monte Carlo Simulation

2.2.1 Basics

Based on the Monte Carlo stochastic virtual experiment (67), a computer code is implemented to simulate a RVE loaded with random distributions of GNPs with the desired level of the nanofiller loading. Implementation steps of the Monte Carlo methodology are delineated in the following sections. Numerical simulations are carried out inside a cubic unit cell (RVE) of constant side length of arbitrary units (units may be equally interpreted as 1 μm). Graphite nanoplatelets are then modeled as simple disks of tunable diameter and thickness dispersed either uniformly or with optional specific preferential orientation inside the unit cell. In the case of uniform distribution, the statistical distribution of both the spatial position and the orientation of the particles are uniform. There is the option for creating specific distribution of the diameters and lengths in the developed computer code based on a probability distribution function (PDF), however, for the sake of simplicity in this chapter the geometric dimension are kept fixed. The remaining simulation parameter is the maximum tunneling distance which is allowed to vary as the influencing parameter. For microstructure generation, two possible scenarios are: the impenetrable scenario in which the particles are not allowed to penetrate each other and the penetrable scenario in which they may penetrate and overlap each other. In the next step for the percolation check, the maximum allowable tunneling distance, which is modeled as an auxiliary envelope wrapping the particle, is varied and then the percolation is examined according to the algorithm elaborated in following sections.

2.2.2 Particle Generation

The geometry of each GNP is modeled as two parallel circular planes separated by the thickness of the GNP. Each circular plane in space may be identified by a normal, its center point, its radius and its height. To achieve a uniformly random scattering of the GNPs using the Monte Carlo method, the center of each cylinder is selected randomly inside the sample

unit cell. Then the associated normal vector is specified by means of random homogeneous functions defined by equation 2.1 which produce uniformly random scattering of points on the surface of a sphere.

$$\begin{cases} \theta = 2\pi v \\ \varphi = Arccos(2u - 1) \end{cases} \tag{2.1}$$

In the above equations, $\theta \in [0, 2\pi[$ and $\varphi \in [0, \pi]$ are spherical coordinates as shown in Figure 2.1 and u,v are random variables belonging to $]0, 1[$. The normal vectors generated by the above method guarantee a uniform random distribution of GNPs orientations (127). For generating each particle the procedure of random selection of its center and normal direction is followed successively and then the next particle is identically created.

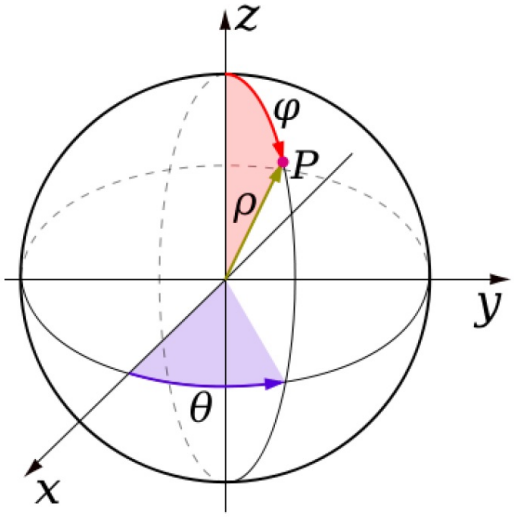

Figure 2.1: Spherical Angles - Schematic shows the spherical angles selected for particle generation.

2.2.3 Penetrable Scheme

In the penetrable scenario, particles are allowed to penetrate into each other (see Figure 2.2). Thus, a new particle is randomly lodged somewhere in the unit cell irrespective of the presence of the formerly generated particles. In other words, regions of space may be

occupied by more than one particle. This idea makes the particle generation algorithm simple and fast. Besides, by using this algorithm one can simulate virtually any volume fraction of GNPs. As another extra advantage, the penetrable algorithm can help to assess the electrical percolation directly when no tunneling is taken into account. Nevertheless, this scenario suffers from some notable drawbacks. Firstly, the assumption of penetrable fillers leads to very low volume fractions when calculating the percolation threshold of the system. As a second disadvantage, the penetrable scheme is not successful in modeling and simulating the unavoidable entanglement and agglomeration of the fillers.

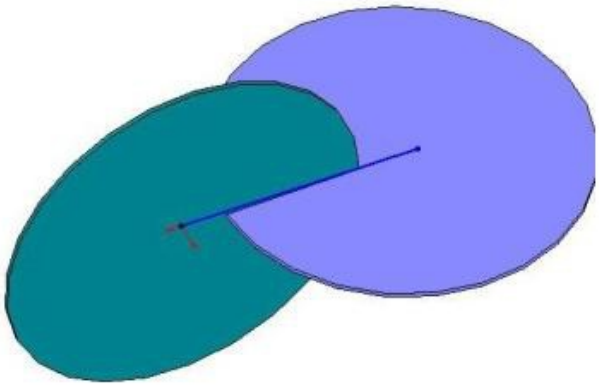

Figure 2.2: Penetrable Scenario - Schematic shows two interfering GNPs created by penetrable scenario.

For evaluating the real volume fraction of randomly distributed permeable particles, the well-known statistical method of Monte Carlo integration which relies on repeated random sampling is employed. To implement the method, a number of random or pseudo-random points are scattered inside the unit cell. Then the ratio of the number of points falling within the regions of space occupied by fillers to the total number of points is calculated as an estimate for the concentration of the filler phase. Then the number of random points inside the unit cell is increased (by up to ≈ 10 orders of magnitude) as a criterion to check the convergence of the calculated concentration. For calculating the real volume fraction in all simulations, this algorithm is employed.

2.2.4 Impenetrable Scheme: Fast Algorithm

The major distinguishing feature in the impenetrable scenario is that the overlapping or intersection of particles are not allowed. Thus, the impenetrable condition is checked during

the generation of every new particle and if a new particle cuts any neighboring particle, the selected center and orientation is rejected and a new set of random center and orientation is picked and this procedure is reiterated through the entire process of particles generation. To check the intersection of two GNPs, one can propose the following efficient algorithm. For every circular plate of a newly generated GNP, the intersections between its infinite encompassing plane and the circular plates of other GNPs are found. These intersections, if there are any, are two line segments of two chords belonging to the intersected circles. It can be shown that the conditions dictated in equation 2.2 governs the intersection state of two circular plates of interest in which r and R are half of the chord lengths and D is the distance between the centers of the chords.

$$\begin{cases} if\ D > r + R\ \Rightarrow\ No\ Contact \\ if\ D \leq r + R\ \Rightarrow\ Contact\ Exists \end{cases} \tag{2.2}$$

The impenetrable scenario, however, possesses several drawbacks such as:

- The algorithm is far too complex to develop and is more time consuming in comparison with the penetrable algorithm.
- For $t \gg h$, where t is the GNP thickness and h is the maximum allowable tunneling distance, the algorithm is likely to get locked.
- When the tunneling is either null or not to be taken into account, the percolation threshold may not be evaluated directly using this algorithm.

As a remedy to the last item, it is proposed to extrapolate the percolation threshold results to zero from simulations with non-zero h which is discussed in section 2.3. Moreover, as a results of the impenetrable constraint, the results are upper bounds for the percolation threshold when compared with the penetrable algorithm results. Compared to the hindering drawbacks, the advantages of the algorithm are significant and appealing. In contrast with the penetrable algorithm, the impenetrable scenario possesses the following benefits:

- In the impenetrable scenario the volume fraction calculations are easy and straightforward (neglecting the fillers cut by the unit cell boundaries).

- The impenetrable scenario is more suitable for finite element simulations in that there is no intersection between the fillers and mesh discretization is carried out easily.
- The predictions made by the impenetrable algorithm are expected to be closer to the true percolation thresholds obtained from experiments.

2.2.5 Incorporation of Tunneling

As discussed earlier, the tunneling effect is a quantum mechanics phenomenon which contributes to the electrical conductivity of polymer composites as well. Based on this phenomenon, two non-touching nanoflakes of GNP inside an insulating matrix will conduct electricity without direct physical contact if the distance between them is small enough for electrons to tunnel through. The maximum tunneling distance varies based on the properties of the medium (128, 129, 130). For most polymers, organic and oxide materials this distance is rather independent of the resistivity of the medium. In this chapter, this maximum distance, h, is allowed to vary to find its effect on the percolation threshold, ϕ_c. Figure 2.3 shows the incorporation of tunneling envelope into the RVE after particle placement. As shown, an imaginary envelope representing half of the tunneling span is assumed around each particle. In other words, the two opposite circular faces of each GNP are offset outward creating a larger disk which is only used for percolation threshold calculation purposes. As will be discussed in the following section, the two GNPs are regarded as touching if their imaginary envelopes intersect. It is evident that the incorporation of the tunneling phenomenon always lowers the percolation threshold (see e.g. (131)).

2.2.6 Percolation Test

Literally, the formation of connected clusters in a non-conducting medium is defined as percolation. Percolation algorithms are applied to check the continuity of an ensemble of conducting objects in touch encapsulated inside a medium. A variety of methods have been proposed in the literature for the purpose of percolation assessment (132). The criterion for evaluating the percolation is to look for at least a cluster of fillers which makes a closed pathway between the entire lateral surfaces of the unit cell.

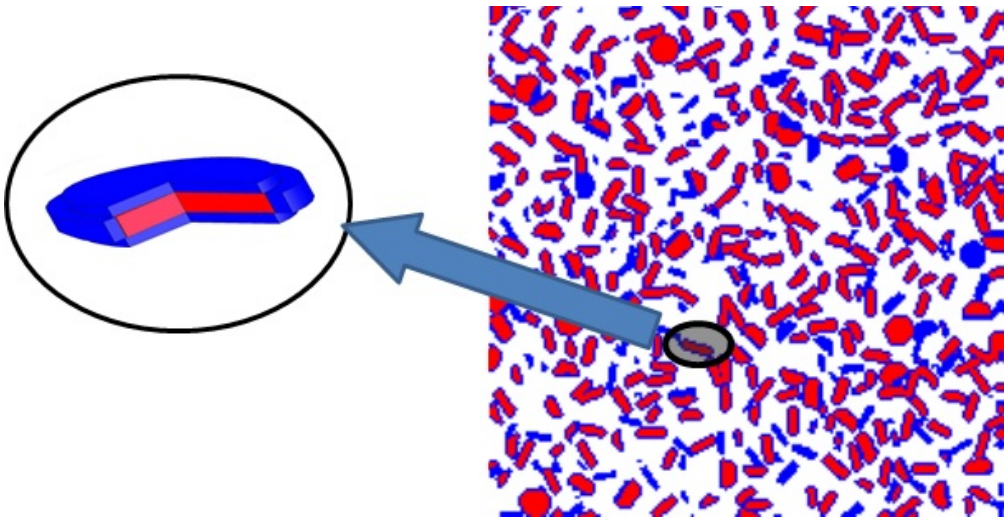

Figure 2.3: Incorporation of Tunneling - Schematic shows a cross section of RVE and incorporation of penetrable tunneling shell around particles.

In the developed simulation code, the percolation analysis is carried out continually and simultaneous to the generation of each particle. In fact, once a GNP is created a cluster number equal to the GNP number is assigned to it. Then all the possible interconnects with the existing objects will be checked and the cluster numbers will be updated. Updating is performed according to the following rule: If, upon the addition of a new object to the system, several objects become electrically connected, the least cluster number in the ensemble is assigned to all the connected objects. Two particles are considered electrically touching if their electron tunneling envelopes satisfy the second inequality in the equation 2.2. The adopted algorithm is specifically accurate for high aspect ratio of GNPs. For low aspect ratio particles, however, other considerations like those employed for nanotubes are required which will be discussed later.

2.3 Results and Discussions

In all simulations, the side length of the cubic unit cell was taken 1000 nm. The diameter of GNPs was kept fixed at 100 nm and their thickness and the tunneling length were allowed to vary to find their effect on ϕ_c. Figure 2.4 exhibits the dependence of the percolation threshold on the tunneling length for various aspect ratio using the impenetrable scenario. The diagrams suggest that for large values of the tunneling length, the percolation threshold

plateaus to some asymptotic values. As discussed earlier, for small values of the tunneling distance, the diagrams are extrapolated to zero.

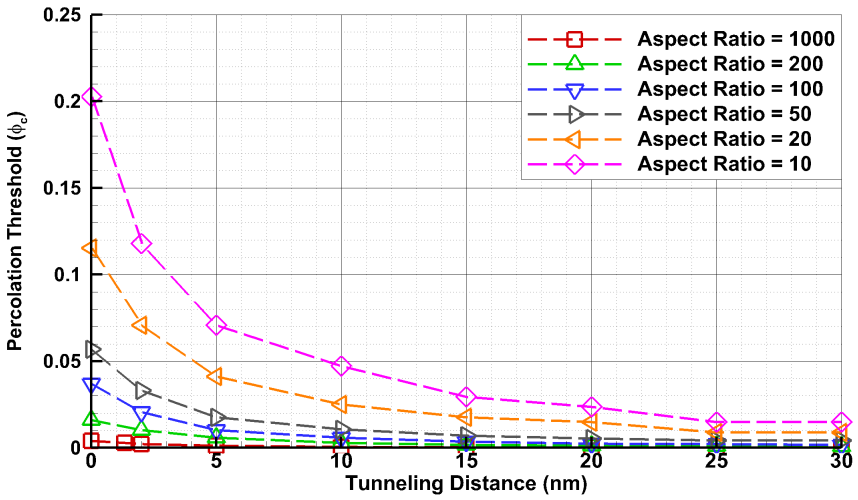

Figure 2.4: Tunneling in Hardcore GNPs - Diagram shows the variation of percolation threshold for impenetrable GNPs with the tunneling distance for different aspect ratios.

Likewise, the diagrams of percolation thresholds using the penetrable algorithm are shown in figure 2.5. The percolation thresholds again tend to plateau values for large tunneling distances. This behavior is more pronounced for high aspect ratio GNPs. As opposed to the impenetrable algorithm, the percolation threshold at zero tunneling distance is calculated directly without having to do any extrapolation. One notices that for large volume fractions of fillers, which are equivalent to large numbers of inhomogeneities, the algorithm gets locked at around a specific volume fraction and the trial number required for inserting another object to the system goes to infinity. As a primary conjecture, one may think of this volume fraction as an upper bound for the maximum obtainable volume fraction when a really random dispersion is achieved and the system is free of agglomeration.

Figure 2.6 shows the percolation threshold versus the tunneling distance obtained by both scenarios. In this figure the GNP aspect ratio is constrained to be 10. It is immediately evident that the impenetrable algorithm yields an upper bound for the small tunneling distance which corresponds to the point that particles physically contact each other at to form a conduction path. The percolation threshold predicted by the impenetrable algorithm, however, falls below that for a larger tunneling distance although the difference is not as

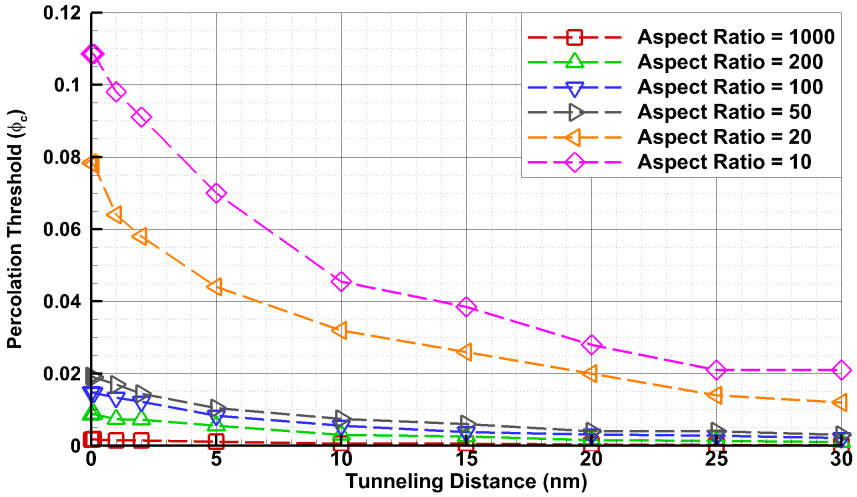

Figure 2.5: Tunneling in Softcore GNPs - Diagram shows the variation of percolation threshold for penetrable GNPs with the tunneling distance for different aspect ratios.

pronounced as the first part. To explain this difference, one may think of the tunneling envelopes as larger disks embracing the GNPs. In the penetrable algorithm, these larger disks can essentially occupy every position inside the unit cell without any restriction and irrespective of the earlier existing objects whereas in the impenetrable algorithm there is a restriction on their positioning. In fact, these new entities can penetrate each other provided that their inner cores do not intersect. Intuitively, for large values of tunneling distance which corresponds to large tunneling envelopes, the percolation threshold, which is equivalent to the least number of fillers making a closed pathway between the two opposite faces of the unit cell, takes place sooner and with fewer GNPs in the impenetrable algorithm.

Table 2.1 compares the simulations with some published experimental results. In all three simulations, the diameter, d, and thickness, t, of GNPs were selected as cited in the experimental studies (91) and the tunneling distance is selected to be $h = 10nm$ corresponding to the approximate value reported in (91). To be in the safe side, the impenetrable algorithm was employed for the simulations. The experimental percolation threshold values are dramatically higher than their respective simulation predictions. In effect, the simulation results provide a lower bound value for the percolation threshold. The main reasons for this wide discrepancy between the simulation and experimental are:

- The simulated GNPs are assumed to be unform and perfect.

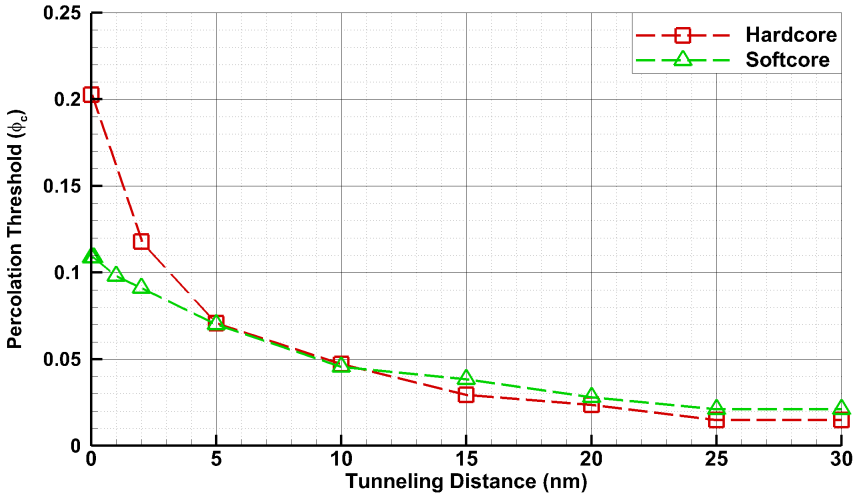

Figure 2.6: Softcore vs. Hardcore GNPs - Diagram compares the variation of percolation threshold for penetrable and impenetrable GNPs with variation of tunneling distance.

- The tunneling distance is assumed to be constant.
- GNPs are assumed to be perfectly dispersed and uniformly distributed in the simulation.
- Agglomeration, non-uniform distribution and unsuccessful dispersion of GNPs exist in the experimental results.

Some research groups reported percolation threshold values which are close enough to the current simulation results. The percolation threshold values reported in (133, 134, 135) vary from 0.1% to 0.6%. Unfortunately, the authors have not provided adequate information about the geometrical and physical properties of the composing particles to allow for conducting appropriate simulations and make a meaningful comparison, however the trend of the simulation results are encouraging.

2.4 Conclusions

In this chapter, the effect of the electron tunneling distance on the electrical percolation threshold of GNP-based nanocomposites was studied. Graphite nanoplatelets were modeled

Table 2.1: Comparison between the predicted percolation threshold of GNPs and the corresponding experimental values.

Study Case	Aspect Ratio	d (μm)	t (nm)	Predicted Percolation Threshold (%vol)	Exp. Percolation Threshold (%vol)
Weng et al. (136)	600	6	10	0.668	4.6
Fukushima and Drzal (37)	1,579	15	9.5	0.294	1.13
Chen et al (137)	5,000	50	10	0.110	0.67

as thin disks randomly distributed in a simulation cuboid. Two scenarios of penetrable and impenetrable objects were implemented for GNPs. Comparison with published experimental results indicates that the impenetrable scenario, which is closer to reality, yields a lower bound estimate for the percolation threshold. Furthermore, the difference between the experimental and simulation results could be attributed to the non-uniform geometry of the dispersed GNPs and their agglomeration in the experiments and/or the assumed invariance of influencing parameters in the simulations, such as the geometry of GNPs and the electron tunneling distance.

3

Comprehensive Electrical Conductivity Model

3.1 Introduction and Scope

As briefly reviewed earlier, CNTs and GNPs are capable of dramatically enhancing the electrical properties when they are incorporated into an insulating polymer. In essence, for a polymer the transition from an electrical insulator into a conductor is strongly dependent on the volume fraction of the conducting filler phase utilized (40). The percolation threshold (ϕ_c) is a specific volume fraction of the fillers phase from which a sharp increase in the electrical conductivity of the composite specimen is observed (80). It is known that when the filler phase is selected to be CNTs and GNPs several parameters as well as filler type and production method (2), dimensional properties (97), the state of dispersion and homogenization can influence ϕ_c. Several studies (41, 91, 96, 97, 124, 125, 126, 138, 139, 140) utilized statistical modeling and analysis tools to investigate the correlation between these parameters and the electrical properties of CNT/GNP/polymer nanocomposites. Proper understanding of the physics of the electrical conductivity in randomly distributed particular inclusions inside a medium is the cornerstone for successful modeling and simulation of the electrical conductivity for these nanocomposites. In the following sections, a more rigorous model to decipher the physics of the electrical conductivity of the CNT/GNP/polymer nanocomposites is provided. The simulation code developed in the previous chapter is also extended here to account for the proposed model. Finally, to examine the validity of the model, the outputs of the simulation are compared to some published experimental measurements.

3.2 Physical Model

For composite comprising spherical conducting particles with diameter D, it was shown (140) that for very large particles ($D \gg 100nm$) with ε as known tunneling distance ($\varepsilon/D \ll 1$), the electrical conductivity near the percolation threshold (right above it) can be described by the classical percolation law given by the equation 3.1 (80):

$$\sigma \propto (\phi - \phi_c)^t \tag{3.1}$$

where ϕ is the filler volume fraction, ϕ_c is the critical percolation threshold and t is a constant known as the conductivity exponent. For a regular 3D system $t \approx 1.6-2.0$ (5, 123), however, for complicated systems it can be 3.0 or more (5).

This model assumes the filler particles physically in touch to from conduction pathways for electrons. This is a valid assumption for large particles, however, for nanoparticles this assumption is only acceptable when they form large agglomerates. When the nanoparticles are well-distributed in the medium with minimal aggregation problems, the classical treatment of the electrical percolation problem with a simple power law scaling of type equation 3.1 was shown to be inaccurate (140). The electrical conductivity in the range of volume fraction less than the percolation threshold (also known as dielectric range) can not be explained with such treatments. Several researches have shown that for a system of conducting nanoparticles dispersed in an insulating matrix, finite size effects including the quantum inter tunneling mechanism between the nanoparticles effectively enhances the electrical conductivity (139, 140, 141). For polymers, organics and oxides matrices the tunneling is independent of their properties (91). For particulate nanocomposites, it is proper to assume the tunneling conductance between each pair of the conducting nanoparticles- i and j inside the system- to be governed by equation 3.2 (140) where δ_{ij} is the shortest distance between two particle surfaces and ϵ is the characteristic tunneling length. In this equation, σ_{pre} is a constant exponential prefactor. Based on this equation, electrons can tunnel trough the space between two conductive nanoparticles separated by a thin layer of matrix material and the probability of electron tunneling exponentially decays with the increase of the distance between them.

$$\sigma_{ij} = \sigma_{pre} exp(-\frac{2\delta_{ij}}{\epsilon}) \tag{3.2}$$

Compared to an insulating polymer ($\sigma_{polymers} = 10^{-15} - 10^{-12}\ Sm^{-1}$), one may assume that the nanoparticles are prefect conductors and in order to investigate the effective electrical conductivity of a polymer composite comprising them, one possible scenario is to calculate the conductivity between each pair of the nanoparticles based on equation 3.2 and form a global tunneling network (GTN), where the conducting nanofillers create a network of globally connected sites utilizing the tunneling mechanism (140). This way the effective conductivity of the network can be found numerically trough Krichhof's law. This method can successfully predict the effective electrical conductivity of nanocomposite materials loaded with nanoparticles fillers. However, even for the case of simple spherical nanoparticles fillers, the GTN method is computationally expensive for large simulation domains and practically it is necessary to impose artificial limitations to the model parameters in order for it to converge (138, 140).

Recently, the GTN approach was extended to nanoparticles with anisotropic geometry (e.g. nanotubes, nanoplatelets)(140). Furthermore, it was observed (140) that the results of the GTN can be successfully reproduced by the critical path (CP) approximation method (138, 142, 143) which was originally developed to explain the electrical conductivity of hopping-type for a dilute system of extremely small particles (nanoparticles) in an amorphous medium. According to this approach, the electrical conductivity of the whole GTN network can be evaluated through a geometric parameter denoted by the critical distance (δ_c) and the tunneling distance (ϵ) based on the equation 3.3.

$$\sigma_c = \sigma_0 exp(-\frac{2\delta_c}{\epsilon}) \tag{3.3}$$

In this equation σ_c is the critical conductivity and σ_0 is a constant. According to this equation, the critical distance (δ_c) represents statistically averaged interparticle distance for the whole specimen (or simulation cell) for which electrons should tunnel through the matrix to establish the critical conductivity (σ_c). The σ_c can be assigned to all particles participating in a cluster spanning over the entire composite. Therefore, the effective conductivity for such percolated system is also governed by a formulation identical to equation 3.3 with a proper prefactor proportional to the contact conductance. This way the electrical conductivity problem for a system of conductive nanoparticles and insulating matrix can be simplified to a more well-understood geometric percolation problem worked out with established theoretical frame in the literature (5).

In the equation 3.3, there is no presumptions regarding the fillers particles geometry. Therefore, the present approach can be readily extended to systems with various filler shapes. However, this advantage is coupled to a new difficulty. The interparticle surface-to-surface distance between each pair of particles becomes now dependent on their relative orientations. Another difficulty arises from the hardcore (non-penetration) requirement. In a computational study, such requirement is easier to retain for simple geometries (e.g. spherical particles) compared to particles with different geometries. However, to overcome this difficulty, each particle can be approximated by an enclosing cylinder around it. Hence, using this virtual cylindrical shell, the interaction between two particles is simply replaced with the interaction between their enclosing cylindrical shells. The current study targets, the electrical conductivity of CNTs and GNPs with intrinsic cylindrical geometry. In the subsequent sections this problem is computationally tackled by utilizing Monte Carlo method.

3.3 Computational Model

3.3.1 Basics

To investigate the problem computationally, first an initial random dispersion of CNTs and GNPs inside a cubic simulation cell was generated (described in section 3.3.2). Starting with an initial guess for δ_c, a penetrable conforming cylindrical shell with thickness $\delta_c/2$ was added to each nanoparticle within the simulation cell and the minimum value of δ_c is found such to insure percolation in all three directions. The percolation was checked according to the method described earlier (see section 2.2.6). By carrying a number of simulations with identical parameters, but each time with different random distribution of the nanoparticles, the statistical averaged value of δ_c was found for each setting. Thus, δ_c was obtained for mixed configurations with different volume fractions of fillers phases with different geometric parameters. The percolation threshold of the desired configuration can be determined simply by comparing δ_c with the electrical tunneling distance as will be described later. As mentioned before, it is important to retain the non-penetrable (hardcore) requirement. The contact assessment algorithm utilized previously (see section 2.2.4) fails for high aspect ratio CNTs. A precise algorithm to examine the particle contact was developed and utilized in all studies. The details of the Monte Carlo model is provided in following sections.

3.3.2 Particle Generation

An infinitesimal element of the composite, sufficiently large to represent the local behavior statistically, is modeled as a cuboid RVE filled with an amorphous insulating polymer comprising two species of conducting fillers (CNTs and GNPs). For this purpose each specie of the nanoparticles presumed to have cylindrical geometry with constant height (h) and diameter (D). For simplicity, the aspect ratio of either filler particle is defined as the ratio of its larger dimension to its smaller dimension. Desired volume fractions of CNTs, GNPs and mixed CNT/GNP were generated homogenously throughout the cell. In order to prevent nonequilibrium conditions and artificial aggregation in the mixed filler configurations, an extended version of standard random sequential addition (RSA) procedure (144) was implemented. For this purpose, during the sequential addition of particles to the simulation cell, the new particle was chosen randomly from the remaining number of CNTs and GNPs. A subset of three random numbers was generated as the position coordinates of the center. In order to ensure isotropic orientation distribution, the orientations of the particles were generated based on the method discussed earlier (see equation 2.1). A new method was applied to impose the hardcore condition as described in section 3.3.3. To minimize the size effects, the RVE was chosen to be big enough with periodic boundary conditions according to a method discussed elsewhere (145). Figure 3.1 shows a sample RVE prepared by the discussed method for the Monte Carlo study.

3.3.3 Impenetrable Cylinders: Precise Algorithm

The intersection between two cylinders can be detected through projection method based on an algorithm originally developed by Eberly (146). A cylinder can be defined by its center $\boldsymbol{C}$, axis direction $\boldsymbol{W}$, hight h and radius r. It is possible to establish a right-hand cartesian coordinate system based on unit-length orthonormal vectors $(\boldsymbol{U}, \boldsymbol{V}, \boldsymbol{W})$. A point in the cylinder is parameterized by equation 3.4 where $\theta \in [0, 2\pi)$, $0 \leq s \leq r$ and $\mid t \mid \leq h/2$.

$$\boldsymbol{X}(s, \theta, t) = \boldsymbol{C} + s\cos(\theta)\boldsymbol{U} + s\sin(\theta)\boldsymbol{V} + t\boldsymbol{W} \tag{3.4}$$

based on this representation, the cylinder wall can be defined by $(\boldsymbol{X} - \boldsymbol{C})^T(\boldsymbol{I} - \boldsymbol{W}\boldsymbol{W}^T)(\boldsymbol{X} - \boldsymbol{C}) = r^2$ and the boundedness of the cylinder is specified by $\mid \boldsymbol{W} \cdot (\boldsymbol{X} - \boldsymbol{C}) \mid \leq h/2$. According to the projection method, two convex objects are separated if they have a separation line. A

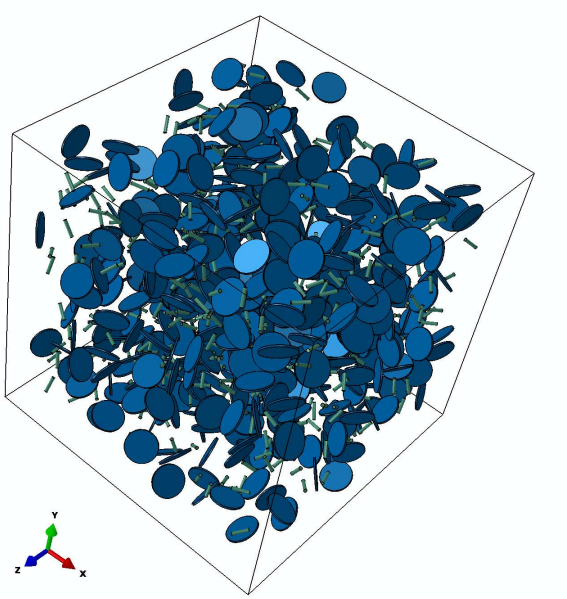

Figure 3.1: Sample RVE Containing CNTs and GNPs - Schematic shows a sample RVE generated by the discussed method containing impenetrable CNTs (0.1 %vol) and GNPs (0.5 %vol) and aspect ratio=10.

separation line is a line for which the intervals of projection of the two objects onto it do not intersect. The projection interval of the convex set C on a line passing through the origin with direction $\boldsymbol{D}$ is defined by equation 3.5.

$$I \equiv [\lambda_{min}(\boldsymbol{D}), \lambda_{max}(\boldsymbol{D})] = [min(\boldsymbol{D} \cdot \boldsymbol{X} : \boldsymbol{X} \in C), max(\boldsymbol{D} \cdot \boldsymbol{X} : \boldsymbol{X} \in C)] \tag{3.5}$$

Two convex sets (C_0, C_1), are separated if there is a direction $\boldsymbol{D}$ such that their projection intervals I_0 and I_1 do not intersect $(I_0 \bigcap I_1 = \varnothing)$. There is no need to check infinite directions to find the separation line. Generally, for a pair of convex polyhedrons, one should only check vectors normal to the faces of the polyhedron and vectors generated by cross products of two edges, one from each polyhedron. Eberly (146) also provided detailed algorithm and pseudo-code for the determination of cylinder-cylinder intersection which for briefness is not discussed here. It should be mentioned that this algorithm is relatively slow and computationally expensive. However, to ensure the fulfilment of the impenetrable conditions, this algorithm is adopted to check the intersection between the particles in the current study.

3.3.4 Tunneling Considerations

According to equation 3.3, the critical distance and the tunneling distance are crucial parameters that dictate the electrical conductivity of a nanocomposite loaded with nanofillers. It was observed that the tunneling distance can vary with the filler particle dimensions and geometry (75). However, there is no simple relation to correlate the geometry of the particle to the tunneling range. Here, to partially avoid this drawback, in the upcoming simulations -with mixed configurations of CNTs and GNPs- the geometry of the particles is simplified to cylinders and their characteristic dimension (selected to be the larger dimension) is selected to be equal and constant. To control the aspect ratio the second unconstrained dimension is allowed to be vary. By employing this strategy, the tunneling distance effect on the simulation will be minimal and, thus, the critical distance is the only governing factor.

3.4 Model Verification and Validation

In order to investigate the accuracy and the applicability of the model, in this section the simulation results are compared with some published theoretical and experimental works. Several experimental studies were carried out for assessing the electrical percolation of nanocomposites based on CNTs or GNPs as single type of fillers (2, 5) but there are not as many studies treating the electrical percolation of a mix of CNTs and GNPs (47, 147, 148, 149). To authors's best knowledge, currently there is no cited literature utilizing identical statistical simulation approach for the case of mixed particle geometries. Additionally, most of the theoretical approaches oversimplify the simulations by assuming the filler particles to be penetrable.

Figure 3.2 illustrates the present simulation predictions for GNP/polymer nanocomposites. In this figure, each curve represent one aspect ratio for the GNPs and the dashed line represents the electron tunneling distance $\epsilon = 10\ nm$. Under ideal conditions the intercept of the dashed line with the different aspect ratio curves constitutes a good criterion for the theoretical percolation threshold. For the aspect ratio=100, the corresponding percolation threshold is about 0.20 % vol which is in good agreement with in the theoretically predicted value cited in the literature (91).

Figure 3.3 compares the present model predictions with three different experimentally measured electrical conductivity of GNPs nanocomposites cited in the literature. To ensure con-

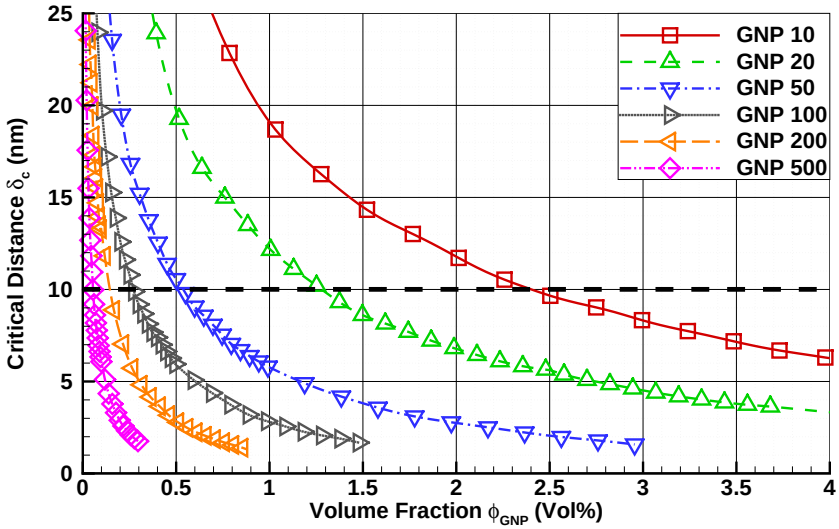

Figure 3.2: Simulation Predictions for GNPs - Diagram shows variation of critical distance as a function of filler content for GNPs with various aspect ratios.

sistency, for all the simulations the electron tunneling distance between the GNPs at room temperature was selected to be 10 nm; in agreement with the published value (140, 144). Figure 3.3 suggests that for volume fractions less than 0.30%vol, the predicted electrical conductivity results are in good agreement with the experimental values.

According to Figure 3.3, for high volume fractions and high aspect ratios, the simulation results deviate significantly from the experiments. For instance, the calculated electrical conductivity of a composite comprising GNPs with initial aspect ratio of 100 starts to deviate from the corresponding measurements at about 0.40 %vol and falls right above the GNP-10 curve. The discrepancy between the experimental and the simulation results are even worse for higher aspect ratios (> 100). This discrepancy can be explained in lieu of the modeling and experimental uncertainties. Based on the experimental observations, graphene sheets have ripple-like corrugated shapes originated from thermal fluctuations (153) which reduces their effective aspect ratio. Graphite nanoplatelets are less compliant along the out-of-plane direction compared to graphene, however, they still have tendency to fold. Moreover, the sonication process- employed to disperse the GNPs- provides mechanical stimulation which could increase the chances of folding. Opposingly, in the simulations GNPs are considered to be perfect cylinders with unique aspect ratio. Furthermore, it was experimentally observed (151) that highly localized deformation energy exerted to GNPs during the sonication step

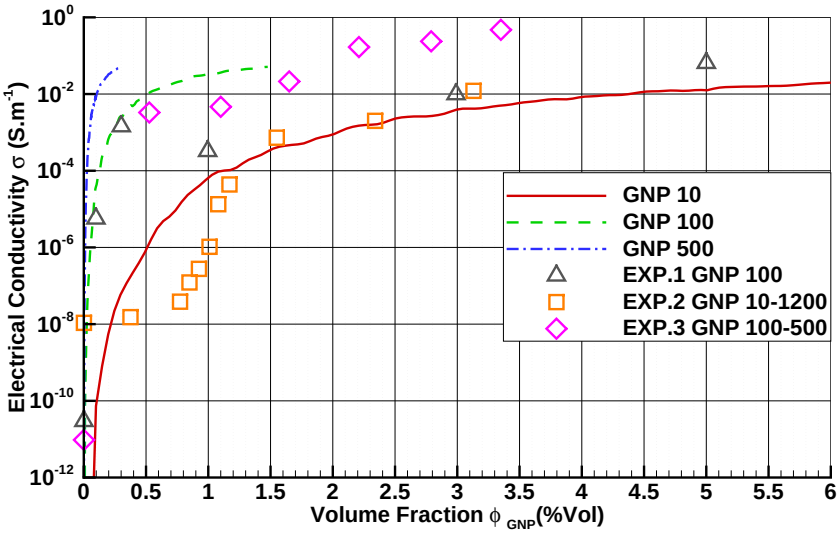

Figure 3.3: Validation of Simulation for GNPs - Diagram compares prediction of σ for GNP/polymer nanocomposites with experiment. Solid lines represent simulation predictions ($\epsilon = 10nm$ and $\sigma_0 = 0.1$) for aspect ratios 10-500. Exp-1 after (150), Exp-2 after (151) and Exp-3 after (152).

could fracture them into smaller fragments. Intuitively, the higher the aspect ratio the more prone are the GNPs to fracture. To clarify, the results of a relevant experimental observation (151) is compared to the simulation results in Figure 3.3. According to this experimental study, during sonication initially high aspect ratio GNPs are fragmented to smaller particles with the final aspect ratio in the wide range of 10-1200. Although the authors did not provide a shape distribution histogram, intuitively it should be more skewed toward finer particle with lower aspect ratios (≈ 10).

To investigate the possible effect of the nanoparticles geometry, the experimentally measured σ for CNT/polymer nanocomposites are compared with the simulation predictions as illustrated in Figure 3.4. Experimental data were drawn from experimental studies reporting both well and poorly dispersed CNTs. For samples with well-dispersed CNTs (Exp.1 and Exp.2), the simulation results corresponding to aspect ratios of 150 and 400 (CNT 150 and CNT 400) are in good agreements with the measured conductivity. For ill dispersed CNTs, the experimental results shows no special trend since the present simulation is not accounting for the nanoparticle agglomeration.

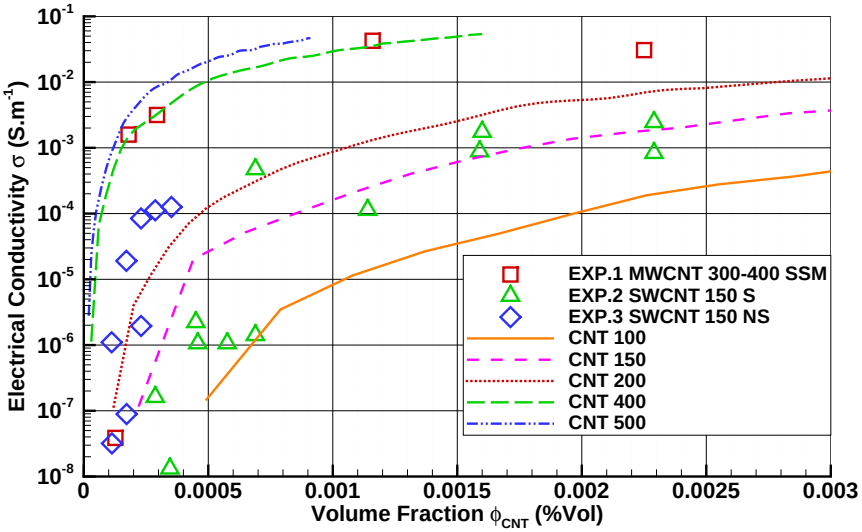

Figure 3.4: Validation of the Simulation for CNTs - Diagram compares the prediction of σ for CNT/polymer nanocomposites with experiment. Solid lines represent simulation predictions ($\epsilon = 10nm$ and $\sigma_0 = 0.25$) for CNTs with aspect ratio 100-500. S: Sonicated, NS: Non-Sonicated and SSM: Sonicated and Shear Mixed. Exp.1 after (18), Exp.2, Exp.3 and Exp.4 after (154)

3.5 Conclusions

To conclude this chapter, it should be emphasized that for low filler's concentrations; good distribution and agglomerate free filler phase, the proposed model successfully predicts the electrical conductivity measurements. However, by increasing the filler contents, the simulation results start to deviate from the experimental measurement which is mainly attributed to the complexity of the system and modeling uncertainties. As far as modeling uncertainties, the current treatment of the tunneling conductivity considers exponential decay of the tunneling current, however, directional dependency of the tunneling could be an important factor which should be addressed in future work. Furthermore, aleatory experimental uncertainties should be also addressed in the model as well as the distribution of particle geometric dimensions, dispersion and particle entanglement, particle deformation, damage and fracture, presence of voids, microbubbles and residual contaminations. These types of information should be provided by experimental studies.

4

Comprehensive Thermal Conductivity Model

4.1 Introduction and Scope

Carbon nanotubes and GNPs are famous for their superior inherent thermal conductivity (1, 2) and their potential to enhance the effective thermal conductivity of their derivative nanocomposite. Traditionally, classical homogenization techniques have been utilized to evaluate the effective thermal conductivity of the composites materials (101). To evaluate the effective thermal conductivity of the composite materials, a number of closed form relations were developed (101). However, most of these relations break down for nanocomposites in which the filler phase usually possess large thermal conductivity compared to the matrix, shape polydispersity (multiphase) and random heterogenous structure (nonperiodic).

The main branches of the classical homogenization techniques are statistical methods (155), mean field methods (156), asymptotic methods (157), variational energy-based methods (158) and empirical/semiempirical methods (159). Generally, the mean field homogenization and the asymptotic approaches are not applicable for the homogenization of random heterogeneous materials because they are mostly limited to composite materials with particular inclusions and periodic microstructure. Variational energy-based methods usually provide some bounds on the effective properties under specific conditions (101, 155). This is not the case for the statistical homogenization techniques since they are neither limited to the periodic microstructures nor just providing bounds on the effective properties. Through statistical continuum theory (160), it is possible to mathematically depict the dispersion and

distribution of the heterogeneous materials. Based on these methods, structural information is directly reflected in the solution through microstructural descriptor functions which are appearing within the solution expression (155). Different types of correlation functions such as the N-point correlation functions (155, 160) are examples of these functions. Through N-point correlation functions, the distribution, orientation and the shape of the heterogeneity for non-eigen heterogeneous systems can be completely described when N is infinite. In the case of periodic eigen microstructures even two-point correlation functions are sufficient to describe the microstructure up to an inversion or translation (161). In general, two-point correlation functions of a d-dimensional isotropic media can be extracted from a m-dimensional cut of the d-dimensional medium (m=1, 2, . . . , d-1) (162).

In the past decades, statistical continuum mechanics methods have been proven as a powerful basis for the reconstruction and homogenization of the microstructures (155). For instance, weak contrast expansions are originally developed based on the perturbation series which can perfectly estimate the effective properties for the small contrast of the constituent properties. Developing a powerful approach for estimating the effective properties of a microstructure with high-contrast constituents and complex microstructure led to the strong-contrast expansions (155, 162, 163). The d-dimensional strong-contrast formulation was first developed to evaluate the effective elastic, electrical, thermal and permeability properties of a microstructure comprising two isotropic phases (155). Later, this approach was extended to multiphase microstructures (162, 163). As a shortcoming, despite some simple microstructures, strong-contrast expansions should be evaluated numerically. To numerically evaluate them, their series expansion is usually truncated up to third order terms which only incorporates the two-point and three-point correlation functions into the solution.

In the following chapter, the strong contrast expansion is adopted and developed for multiphase microstructures (163). This expansion computes a third-order estimate for the effective thermal conductivity of CNT and GNP-based nanocomposites. To generalize the applicability of the proposed solution, a novel method is applied to approximate the three point correlation functions by two-point correlation functions of the same microstructure. Generally, strong-contrast expansions presume a reference medium properties in their derivation. In the case of multiphase hybrid nanocomposites it was shown that the proper selection of this reference medium is very important. A novel approach is also exploited to minimize the effect of the reference phase properties on the estimated effective thermal conductivity. As mentioned earlier, the proposed method is suitable for nanomaterials such as CNTs with

tubular structure and GNPs with disk-shaped structure. To investigate the validity of the proposed approach, sets of two-phase and three-phase microstructures comprising tubular and disk-shaped inclusions are selected. The effective thermal conductivity for each microstructure is estimated with both the proposed method and with a standard finite element method. Finally, the estimated properties of both methods are quantitatively compared and the comparisons between the results are discussed.

4.2 Computational Model

4.2.1 Strong-Contrast Expansion

The construction of the model for a general microstructure will be discussed. For a general microstructure with characteristic microscopic length scale much smaller than that of the specimen length scale and consisting of three different phases, where each phase has the volume fraction $\phi_\alpha(\alpha = 1..3)$ and is characterized by isotropic thermal conductivity of σ_α, the local conductivity at position $\boldsymbol{x}$ is described by equation 4.1.

$$\sigma(\boldsymbol{x}) = \sum_{\alpha=1}^{3} \sigma_\alpha \mathcal{J}^{(\alpha)}(\boldsymbol{x}) \tag{4.1}$$

In this relation, the indicator function ($\mathcal{J}^{(\alpha)}(\boldsymbol{x})$ is) for each phase is defined by equation 4.2.

$$\mathcal{J}^{(\alpha)}(\boldsymbol{x}) = \begin{cases} 1 & \boldsymbol{x} \text{ in phase } \alpha \\ 0 & \text{otherwise} \end{cases} \tag{4.2}$$

Knowing that the local intensity filed ($\boldsymbol{E(x)}$) and the local thermal current ($\boldsymbol{J(x)}$) are interrelated by equation 4.3.

$$\boldsymbol{J(x)} = \sigma(\boldsymbol{x})\boldsymbol{E(x)} \tag{4.3}$$

It is possible to embed this microstructure into a reference medium with thermal conductivity σ_0, subjected to an intensity field $\boldsymbol{E_0(x)}$ at the infinity and define a polarization field $\boldsymbol{P(x)}$

by equation 4.4.

$$\boldsymbol{P}(\boldsymbol{x}) = (\sigma(\boldsymbol{x}) - \sigma_0)\boldsymbol{E}(\boldsymbol{x}) \tag{4.4}$$

Under steady state condition the polarization field is related to the temperature distribution (and also knowing that $\boldsymbol{E}(\boldsymbol{x}) = -\boldsymbol{\nabla}T(\boldsymbol{x})$) by equation 4.5.

$$\sigma_0 \Delta T(\boldsymbol{x}) = \boldsymbol{\nabla}.\boldsymbol{P}(\boldsymbol{x}) \tag{4.5}$$

Adopting the Green's function solution to the Laplace equation at the infinity this equation can be solved. However, to obtain the intensity field $\boldsymbol{E}(\boldsymbol{x})$, the solution to this equation should be differentiated by excluding an infinitesimal region around each solution point and introducing a cavity intensity field ($\boldsymbol{F}(\boldsymbol{x})$). Torquato (155) has shown that equation 4.6 is established.

$$\boldsymbol{E}(\boldsymbol{x}) = \boldsymbol{E_0}(\boldsymbol{x}) + \int dx' \boldsymbol{G^{(0)}}(\boldsymbol{r}).\boldsymbol{P}(\boldsymbol{x'}) \tag{4.6}$$

where $\boldsymbol{G^{(0)}}(\boldsymbol{r})$ is defined by equation 4.7.

$$\boldsymbol{G^{(0)}}(\boldsymbol{r}) = -\boldsymbol{D^{(0)}}\delta(\boldsymbol{r}) + \boldsymbol{H^{(0)}}(\boldsymbol{r}) \tag{4.7}$$

and also $\boldsymbol{D^{(0)}}$ is defined through equation 4.8.

$$\boldsymbol{D^{(0)}} = \frac{1}{3\sigma_0}\boldsymbol{I}, \quad \boldsymbol{H^{(0)}}(\boldsymbol{r}) = \frac{1}{4\pi\sigma_0}\frac{3\boldsymbol{nn} - \boldsymbol{I}}{r^3} \tag{4.8}$$

where the vector $\boldsymbol{n} = \boldsymbol{r}/|\boldsymbol{r}|$ and $\boldsymbol{I}$ is the second order identity tensor. This integral over the surface of an excluded infinitesimal spherical cavity is identically zero. Thus, a formulation for the cavity intensity field $F(x)$ can be deduced by substituting equation 4.8 into equation 4.7 and finding equation 4.9.

$$\boldsymbol{F}(\boldsymbol{x}) = \boldsymbol{E_0}(\boldsymbol{x}) + \int_{\epsilon} dx' \boldsymbol{H^{(0)}}(\boldsymbol{x} - \boldsymbol{x'}).\boldsymbol{P}(\boldsymbol{x'}) \tag{4.9}$$

in which the cavity intensity field is $\boldsymbol{F(x)}$ is defined by equation 4.10

$$\boldsymbol{F(x)} = \{\boldsymbol{I} + \boldsymbol{D^{(0)}}[\sigma(\boldsymbol{x}) - \sigma_0]\}.\boldsymbol{E(x)} \tag{4.10}$$

by combining equations 4.10 and 4.4, the relationship between the polarization field and cavity intensity field is established by equation 4.11.

$$\boldsymbol{P(x)} = L(\boldsymbol{x})\boldsymbol{F(x)} \tag{4.11}$$

where in this equation $L(\boldsymbol{x})$ is defined by equation 4.12.

$$L(\boldsymbol{x}) = 3\sigma_0 \sum_{\alpha=1}^{3} b_{\alpha 0}\mathfrak{I}^{(\alpha)}(\boldsymbol{x}) \tag{4.12}$$

and $b_{\alpha 0}$ is defined by equation 4.13

$$b_{\alpha 0} = \frac{\sigma_\alpha - \sigma_0}{\sigma_\alpha + 2\sigma_0} \quad , \alpha = 1 \cdots 3 \tag{4.13}$$

Knowing that the average cavity field is related to the polarization field by equation 4.14.

$$\langle \boldsymbol{P(x)} \rangle = \boldsymbol{L_e}.\langle \boldsymbol{F(x)} \rangle \tag{4.14}$$

in which the angular brackets represent the ensemble average. With some mathematical simplification, it is possible to show that the second-order tensor $\boldsymbol{L_e}$ is related to the effective thermal conductivity tensor for the microstructure ($\boldsymbol{\sigma_e}$) by equation 4.15.

$$\boldsymbol{L_e} = 3\sigma_0\{\boldsymbol{\sigma_e} - \sigma_0\boldsymbol{I}\}.\{\boldsymbol{\sigma_e} + 2\sigma_0\boldsymbol{I}\}^{-1} \tag{4.15}$$

Torquato (155) has shown that the explicit form of the effective conductivity can be defined by equation 4.16

$$\boldsymbol{L_e^{-1}(1)} = \frac{\boldsymbol{I}(1)}{\langle L(1)\rangle} - \int (\frac{\langle L(1)L(2)\rangle - \langle L(1)\rangle\langle L(2)\rangle}{\langle L(1)\rangle\langle L(2)\rangle})\boldsymbol{H}^{(0)}(1,2)d2 - \int\int (\frac{\langle L(1)L(2)L(3)\rangle}{\langle L(1)\rangle\langle L(2)\rangle} - \frac{\langle L(1)L(2)\rangle\langle L(2)L(3)\rangle}{\langle L(1)\rangle\langle L(2)\rangle\langle L(3)\rangle})\boldsymbol{H}^{(0)}(1,2).\boldsymbol{H}^{(0)}(2,3)d2d3 + \cdots \tag{4.16}$$

in this equation the shorthand notation $X = 1$, $X' = 2$ and $X'' = 3$ were applied. This equation utilizes $\langle L(1)\cdots L(n)\rangle$ terms which are related to the N-point microstructural correlation functions. For instance, for a combination of three phases α, β and γ one can establish equations 4.17 and 4.18.

$$\langle L(1)\rangle = 3\sigma_0 \sum_{\alpha=1}^{3} b_{\alpha 0} S_1^{(\alpha)}(1) \tag{4.17}$$

$$\langle L(1)L(2)\rangle - \langle L(1)\rangle\langle L(2)\rangle = (3\sigma_0)^2 \sum_{\alpha=0}^{3}\sum_{\beta=0}^{3} b_{\alpha 0} b_{\beta 0}[S_2^{(\alpha\beta)}(1,2) - S_1^{(\alpha)}(1)S_1^{(\beta)}(2)] \tag{4.18}$$

in which $S_3^{(\alpha\beta\gamma)}$ is a 3-point correlation function defined by equation 4.19.

$$S_3^{(\alpha\beta\gamma)}(\boldsymbol{x_1}, \boldsymbol{x_2}, \boldsymbol{x_3}) = \langle \mathcal{I}^{(\alpha)}(\boldsymbol{x_1})\mathcal{I}^{(\beta)}(\boldsymbol{x_2})\mathcal{I}^{(\gamma)}(\boldsymbol{x_3})\rangle, \quad \alpha, \beta, \gamma = 1\cdots 3 \tag{4.19}$$

4.2.2 Truncated Strong-Contrast Expansion

Following Torquato (155), Pham (163) and Quang (164), the series in equation 4.16 can be truncated up to its third-order terms and then by substituting equation 4.15 into it, after some simplification, the effective conductivity tensor for a general case of macroscopically anisotropic microstructure comprising three phases (CNTs, GNPs and matrix) reduces to equation 4.20.

$$\Big(\frac{1}{\sigma_0}\boldsymbol{\sigma_e} - \boldsymbol{I}\Big)^{-1} = \frac{1}{3}\Big(\frac{1}{\sum_{\alpha=1}^{3}\phi_\alpha b_{\alpha 0}} - 1\Big)\boldsymbol{I} - \boldsymbol{A_2} - \boldsymbol{A_3} \tag{4.20}$$

This equation introduces second-order ($\boldsymbol{A_2}$) and third-order ($\boldsymbol{A_3}$) terms, respectively. Using equations 4.17 and 4.18 and similar expansion for higher order terms, one can show that the $\boldsymbol{A_2}$ and $\boldsymbol{A_3}$ terms can be defined by equations 4.21 and 4.22.

$$\boldsymbol{A_2} = \frac{\sigma_0}{(\sum_{\alpha=1}^{3} \phi_\alpha b_{\alpha 0})^2} \int \sum_{\alpha=1}^{3} \sum_{\beta=1}^{3} \Big(b_{0\alpha} b_{0\beta} [S_2^{(\alpha\beta)}(1,2) - S_1^{(\alpha)}(1) S_1^{(\beta)}(2)] \Big) \boldsymbol{H^{(0)}(1,2)} d2 \quad (4.21)$$

$$\boldsymbol{A_3} = \frac{3\sigma_0}{(\sum_{\alpha=1}^{3} \phi_\alpha b_{\alpha 0})^2} \int \int \Big(\sum_{\alpha=1}^{3} \sum_{\beta=1}^{3} \sum_{\gamma=1}^{3} b_{0\alpha} b_{0\beta} b_{0\gamma} S_3^{(\alpha\beta\gamma)}(1,2,3) - \frac{1}{\sum_{\alpha=1}^{3} \phi_\alpha b_{\alpha 0}} \sum_{\alpha=1}^{3} \sum_{\beta=1}^{3} \sum_{\gamma=1}^{3} \sum_{\delta=1}^{3} b_{0\alpha} b_{0\beta} b_{0\gamma} b_{0\delta} S_2^{(\alpha\beta)}(1,2) S_2^{(\gamma\delta)}(2,3) \Big) \boldsymbol{H^{(0)}(1,2) H^{(0)}(2,3)} d2 d3 \quad (4.22)$$

It should be noted that in both equations 4.21 and 4.22, the $b_{0\alpha} (\alpha = 1 \cdots 3)$ terms only depend on the properties of each phase and the reference medium and, therefore, the summations can be expanded and these terms can be factored out of each tensor integration as constants. The third-order terms require three-point correlation function which can be approximated properly; the details are addressed in section 4.2.3. Since equation 4.20 has no closed form analytical solution, it should be evaluated numerically. Because of the truncated nature of this expansion, care must be taken during the numerical solution in order to guarantee its convergence to the true solution. Detailed discussion about the numerical evaluation of this equation is provided in section 4.2.4.

4.2.3 Microstructural Descriptor Functions

Several mathematical approaches toward describing microstructural details are developed in relatively disparate fields of applied physics. Among them the N-points probability functions introduced by equation 4.19 have been widely applied in the context of determining the effective properties (155). One-point correlation function is approximating the volume fraction (ϕ_α) of each phase in a microstructure. Two-points correlation functions (TPCFs) are the lowest order of their kind that are capable of providing geometrical information about the microstructure (155). For instance, TPCF of the homogeneous two-phase microstructures

comprising isotropic dispersion of unique tubular inclusions is shown in Figure 4.1. In this figure, the TPCFs are calculated numerically from a RVE generated by the Monte Carlo method described in section 3.3.2. As the correlation length approaches infinity, TPCFs converge to a constant value ($\approx \phi_\alpha^2$) with no dependence on the orientation.

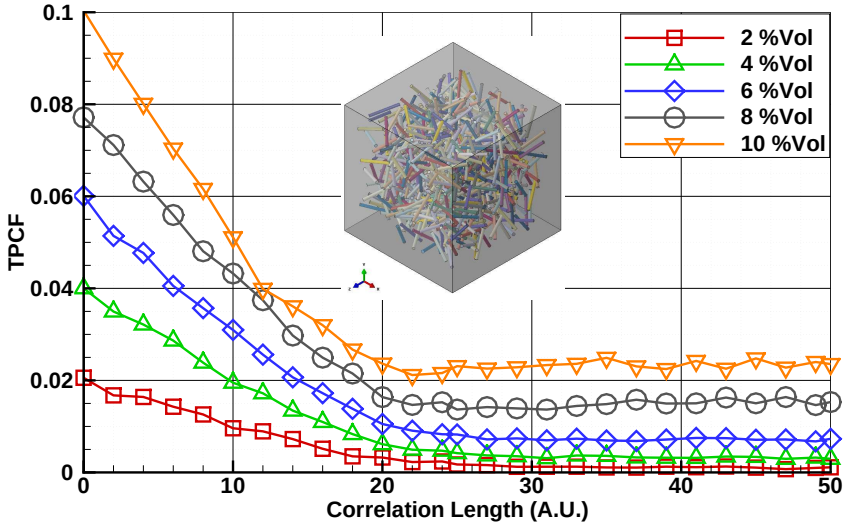

Figure 4.1: TPCFs of Isotropic Tubes - Two-point correlation function (TPCF) of isotropic homogeneous microstructures loaded with 2-10 %vol tubular inclusions ($\phi = 20$, $l = 200$ and Aspect Ratio = 10). The inset shows 3D view of the RVE for 4%vol configuration.

Similar functions for an anisotropic microstructure with tubular inclusions aligned in x-direction should show strong correlation in this direction compared to the other directions. Figure 4.2 shows TPCFs of microstructure comprising 4%vol tubular inclusion when they are perfectly aligned in the x-direction.

In order to correctly represent this anisotropic microstructure a three-dimensional correlation function is required. Three dimensional correlation functions can be approximated from TPCFs evaluated from two-dimensional cuts of microstructure. Corson method (165) is applied here to evaluate the three dimensional TPCF of this microstructure as illustrated in Figure 4.3.

Two-point correlation functions can be analytically evaluated for certain simple microstructures (155). However for a general random heterogenous microstructure TPCFs can be evaluated numerically by Monte-Carlo simulation. Direct numerical evaluation of higher

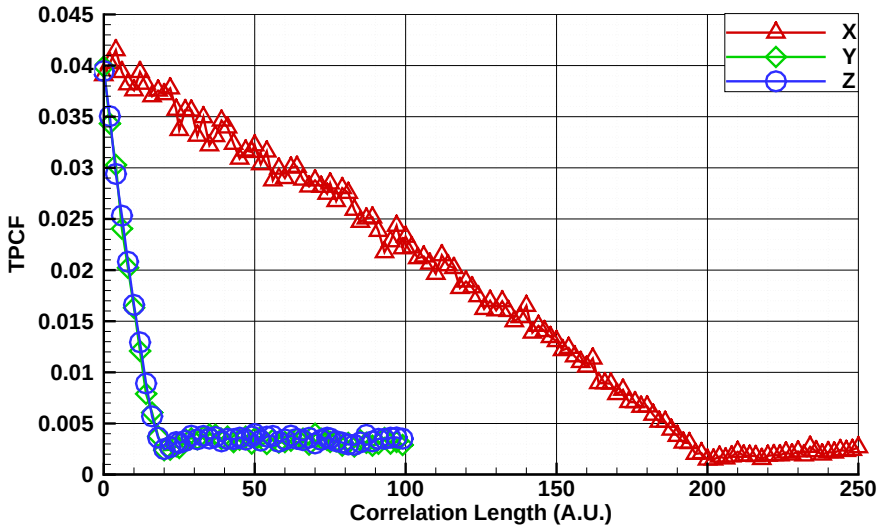

Figure 4.2: TPCFs of Anisotropic Tubes - Two-point correlation functions (TPCFs) of anisotropic homogeneous microstructures loaded with 4 %vol tubular inclusions ($\phi = 20$, $l = 200$ and Aspect Ratio = 10) aligned int the x-direction.

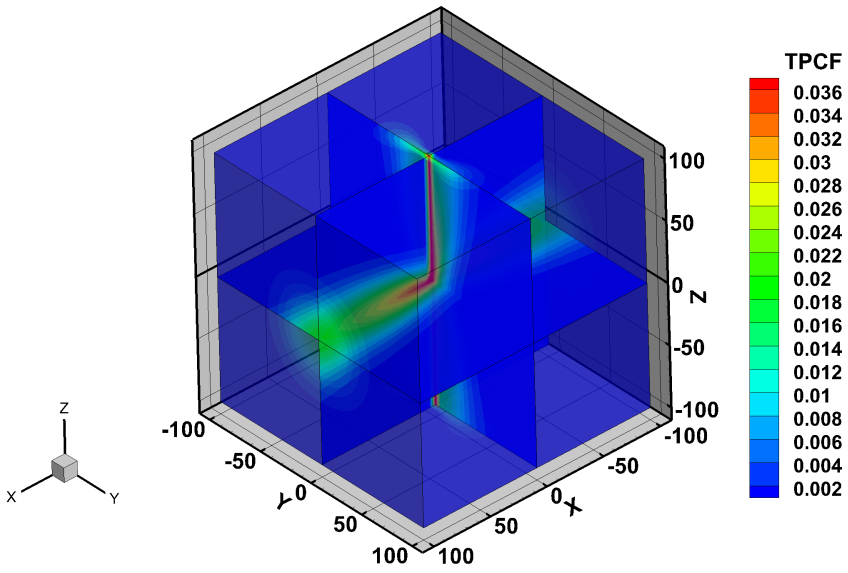

Figure 4.3: 3D TPCF of Anisotropic Tubes - Three dimensional representation of two-point correlation function of homogeneous anisotropic microstructure loaded with 4%vol tubular inclusions ($\phi = 20$, $l = 200$ and Aspect Ratio = 10) with preferred orientation along the x-direction.

order correlation functions is a computationally prohibitive process. Different methods are developed to approximate higher order probability functions from lower order ones (166, 167). Recently a novel method is introduced to approximate n-point correlation functions from (n-1)-point correlation functions (167). Here three-point correlation function are approximated from TPCFs by utilizing this method according to equation 4.23.

$$S_3^{(\alpha\beta\gamma)}(1,2,3) \approx W_1^3 \frac{S_2^{(\alpha\beta)}(1,2) S_2^{(\alpha\gamma)}(1,3)}{S_1^{(\alpha)}(1)} + W_2^3 \frac{S_2^{(\alpha\beta)}(1,2) S_2^{(\beta\gamma)}(2,3)}{S_1^{(\beta)}(2)} + W_3^3 \frac{S_2^{(\beta\gamma)}(2,3) S_2^{(\alpha\gamma)}(1,3)}{S_1^{(\gamma)}(3)} \tag{4.23}$$

in which the weight functions are defined by equation 4.24.

$$W_i^3 = \frac{R_i}{\sum_{j=1}^{3} R_j} \quad , i = 1 \cdots 3 \tag{4.24}$$

where R_1, R_2 and R_3 are representing the shortest distance between each pair of points (1-3).

4.2.4 Reference Medium Selection

As discussed in the derivation, the strong contrast expansion introduced in equation 4.16 is based on the assumption that the specimen is completely bounded by an infinite reference medium. A strong-contrast expansion comprises infinite number of terms. For the limit of infinite number of terms and when the microstructure is comprising two phases, the expansion is known to converge to the true solution regardless of the properties of the reference medium (σ_0) (155). However, for a three-terms truncation, the absolute convergence to the true solution is contestable. In fact, there is a better chance for this equation to converge to the true solution when the properties of the reference medium (σ_0) are close enough to the effective properties. For only two phase media, Torquato (155) recommends one of the constituents to be selected as the reference medium for the solution. Even under such conditions, two different expansions can be written with no guarantee for a single solution. For a microstructure comprising more than two phases -with orders of magnitude discrepancy between their properties usually the case of CNTs and GNPs- the effective properties can be significantly different from each of the individual phases. For instance, the effective conductivity of microstructure composed of isotropically dispersed tubular inclusions inside a matrix phase with two orders of magnitude difference between the thermal conductivities

$(\sigma_1/\sigma_2 = 100)$ is shown in Figure 4.4. It can be observed that by varying the thermal conductivity of the reference medium between the arithmetic and the harmonic averages, there is a three-fold variation in the estimation of the effective thermal conductivity of the microstructure. This observation strengthens the necessity to devise a method for proper selection of the reference phase properties.

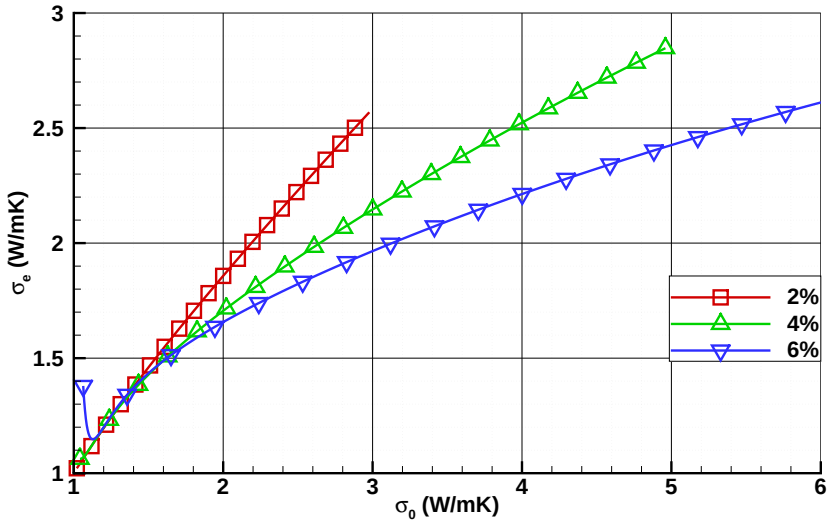

Figure 4.4: Effect of Reference Phase - Effect of σ_0 selection on σ_e for the microstructures loaded with 2,4 and 6%vol tubular inclusions. (Aspect Ratio = 10 and $\sigma_{tube}/\sigma_{matrix} = 100$)

In order to find proper interval for σ_0, equation 4.20 should be solved for $\boldsymbol{\sigma_e}$ as shown in the equation 4.25.

$$\boldsymbol{\sigma_e} = \sigma_0 \left(\boldsymbol{I} + \left(\frac{1}{3} \left(\frac{1}{\sum_{\alpha=1}^{3} \phi_\alpha b_{\alpha 0}} - 1 \right) \boldsymbol{I} - \boldsymbol{A_2} - \boldsymbol{A_3} \right)^{-1} \right) = \boldsymbol{f}(\sigma_0, microstructure) \tag{4.25}$$

In this equation, $\boldsymbol{f}$ represents the approximation function. Assuming the true solution is $\boldsymbol{\sigma_{true}}$, the square absolute approximation error as a function of σ_0 is defined by equation 4.26.

$$\boldsymbol{e}(\sigma_0) = \left(\boldsymbol{f}(\sigma_0) - \boldsymbol{\sigma_{true}} \right)^2 \tag{4.26}$$

Assuming the function $\boldsymbol{e}$ is smooth throughout the domain, one can differentiate this equation and set it to zero as shown in equation 4.27.

$$\frac{\partial \boldsymbol{e}}{\partial \sigma_0} = 2\frac{\partial \boldsymbol{f}}{\partial \sigma_0}\big(\boldsymbol{f}(\sigma_0) - \boldsymbol{\sigma_{true}}\big) = 0 \tag{4.27}$$

the solutions to this equation are shown by equations 4.28 and 4.29.

$$\frac{\partial \boldsymbol{f}}{\partial \sigma_0} = 0 \tag{4.28}$$

$$\boldsymbol{f}(\sigma_0) = \boldsymbol{\sigma_{true}} \tag{4.29}$$

Now, the roots of these equations should possess minimal sensitivity of the function $\boldsymbol{e}$ to the reference phase properties. The solution of the equation 4.29 is trivial, however, equation 4.28 can be solved with the available information. Thus, the roots of equation 4.28 are the best candidates for σ_0. Considering second order continuity for Equation 4.26, it can be differentiated once more as shown by equation 4.30.

$$\frac{\partial^2 \boldsymbol{e}(\sigma_0)}{\partial \sigma_0^2} = 2\frac{\partial^2 \boldsymbol{f}}{\partial \sigma_0^2}\big(\boldsymbol{f}(\sigma_0) - \boldsymbol{\sigma_{true}}\big) + 2\big(\frac{\partial \boldsymbol{f}}{\partial \sigma_0}\big)^2 \tag{4.30}$$

The second term of equation 4.30 vanishes at the candidate points. Intuitively, the solutions of equation 4.25 at the candidate points either overestimate or underestimate the effective properties. Based on this fact, the expression inside the parenthesis of the first term in this equation is either positive or negative thus the best approximation to the effective properties are either local minima or maxima of equation 4.25. When there are at least one local minimum and one maximum points available, the arithmetic average value of them could offer a better estimate of the effective properties by canceling out errors. Evaluation of equation 4.27 analytically is only viable for very simple microstructures. However, numerically it can be evaluated potentially for any combination of microstructure and properties. For the isotropic microstructures described earlier (see Figure 4.1), Figure 4.5 depicts the variation of σ_e ($\boldsymbol{\sigma_e} = \sigma_e \boldsymbol{I}$) with σ_0. The local minimum and maximum provide an upper and lower estimates of the effective properties.

For a general anisotropic microstructure equation 4.27 yields a number of different candidate points. Each of these points represents one possible candidate point for σ_0 to estimate the

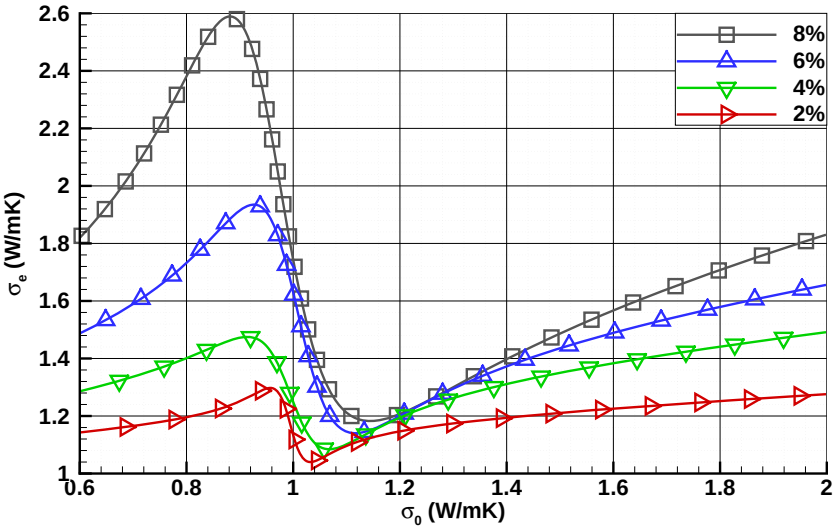

Figure 4.5: Candidate Points for Isotropic Solution - Candidate points for the evaluation of σ_e in an isotropic microstructure loaded with 2, 4, 6 and 8%vol tubular inclusions (Aspect Ratio = 10 and $\sigma_{tube}/\sigma_{matrix} = 100$)

effective properties. For instance, for the anisotropic microstructure described earlier (see Figure 4.2) these point are shown in Figure 4.6.

4.3 Finite Element Model

In this section the effective thermal conductivity for two phase microstructures comprising tubular inclusion and disk-shaped inclusions is studied using FEM. A RVE of the microstructures was generated via the method described in section 3.3.2. The effective thermal conductivity was calculated by finite element method using the commercial finite element code Abaqus 6.10-EF. For the finite element model the microstructure was simulated and meshed with tetrahedral DC3D4 elements. It was assumed there is perfect bounding between the particulate inclusions and the matrix. In order to converge the FEM solution a number of mesh refinement strategies was applied. Initially the mesh was refined around each inclusion by a factor. Then, in the convergence study the mesh was globally refined several times. The boundary conditions was chosen to comprise a constant temperature distributed over the mesh grids on two opposing sides along the x-direction (0 and 100°C) of the simulation cuboid. The analysis was set to be solved under steady state conditions. Finally, the effec-

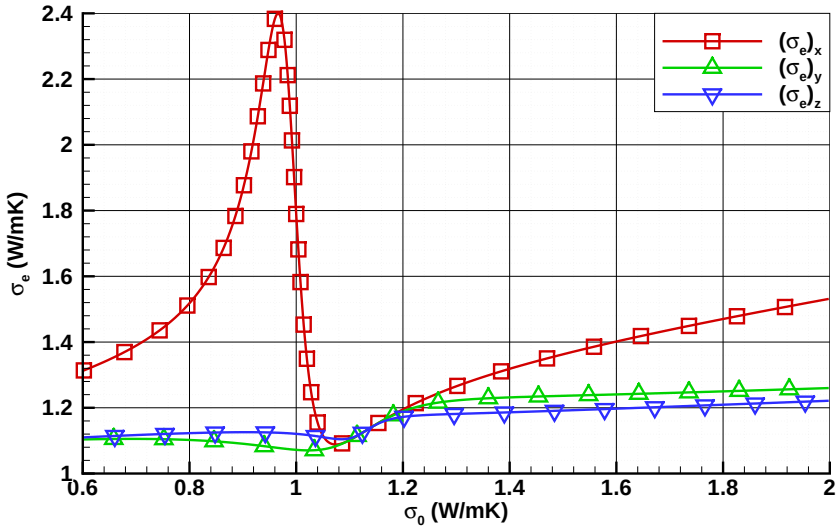

Figure 4.6: Candidate Points for Anisotropic Solution - Existence of different candidate points for an anisotropic microstructure loaded with 4%vol tubular inclusions with preferred orientation in the x-direction. (Aspect Ratio = 10 and $\sigma_{tube}/\sigma_{matrix} = 100$).

tive thermal conductivity was calculated from the temperature difference and the volume averaged heat-flux vector over the whole cuboid. Figure 4.7 shows the output of one of the finite elements simulations for a microstructure with disk-shaped inclusions. Depending on the volume fraction of the inclusions and including the solution convergence study, each FEM simulation was concluded within 10 to 96 hours on a double quad core workstation with 12 GB of memory.

4.4 Model Verification

For the verification purpose, the effective thermal conductivity of the same microstructures utilized in previous section was also evaluated by the proposed method. Strong contrast predictions were computed from two-point correlation functions directly evaluated from the microstructure (RVE) and the approximated three-point correlation functions. The results are compared with their corresponding FEM predictions. Figure 4.8 shows the effective thermal conductivity for the homogeneous composite specimens loaded with different volume fractions of the tubular inclusions (microstructure described in Figure 4.1). The thermal conductivity of the isotropic inclusions was selected such that $\sigma_{tube}/\sigma_{matrix} = 100$. In this

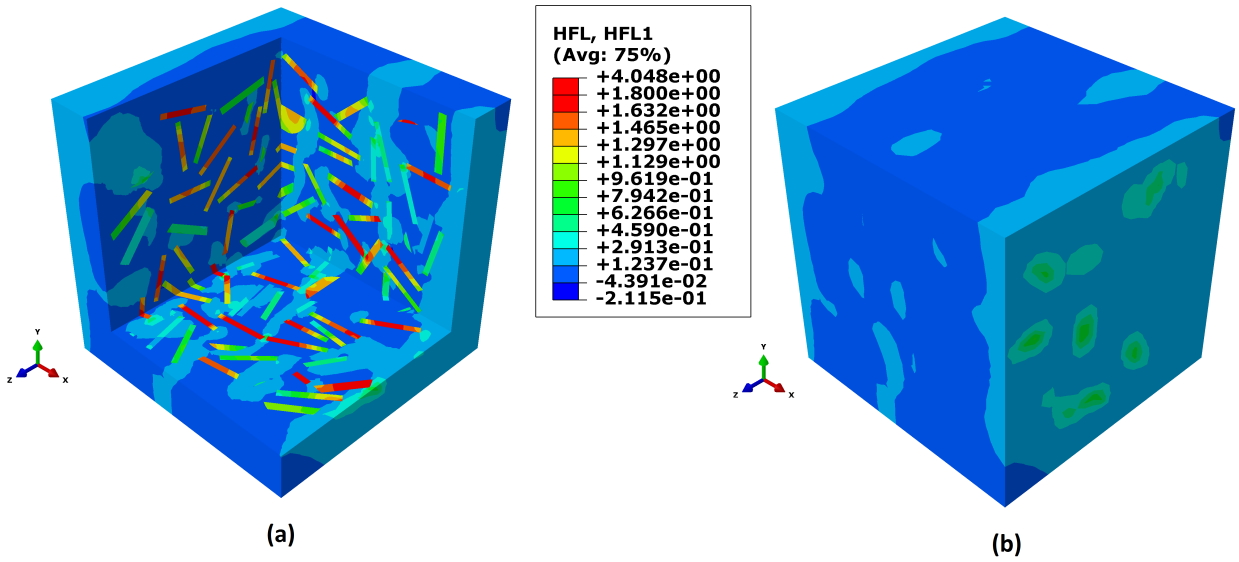

Figure 4.7: Sample FEM Result - FEM calculation of the distribution of the heat-flux in x-direction in the RVE loaded with 10%vol disk-shaped inclusions (Aspect ratio = 10 and $\sigma_{disk} = 100\sigma_{matrix}$) (a) internal view (b) full view.

figure the strong contrast predictions are calculated twice. First, the reference medium selected to be identical to the inclusion phase and then it is selected by the proposed method. Both predictions are also compared with the lower-bound and the FEM predictions. It can be observed that only the predictions of the proposed method are in good agreement with the finite elements results for the case of tubular inclusions.

To verify the applicability of the proposed method for different particle shapes, the effective conductivity of the homogeneous microstructures filled with disk-shaped inclusions was also evaluated. Figure 4.9 shows the comparison between the predicted results of different methods for different volume fractions of disk-shaped inclusions. Good agreement with the finite element predictions is also observed for the proposed strong-contrast method.

4.5 Conclusions

In this chapter a modified version of the strong contrast expansions was formulated to evaluate the effective thermal conductivity of multi-phase heterogenous materials with application in CNT/GNP based nanocomposites. It was shown that the reference medium selection affects the strong-contrast model predictions for microstructures with contrast. A novel

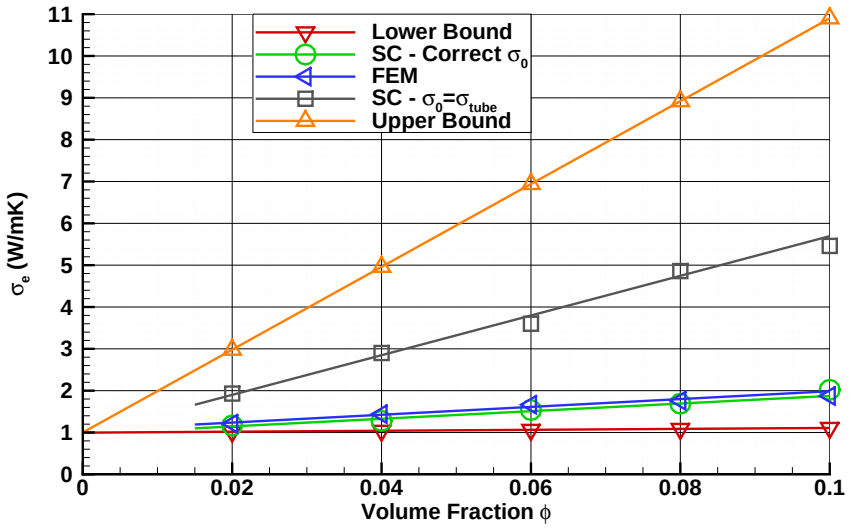

Figure 4.8: Tube Verification - Comparison between the effective thermal conductivities predicted by strong contrast method and finite element method for isotropic microstructures loaded with tubular inclusions. (Aspect Ratio = 10 and $\sigma_{tube}/\sigma_{matrix} = 100$)

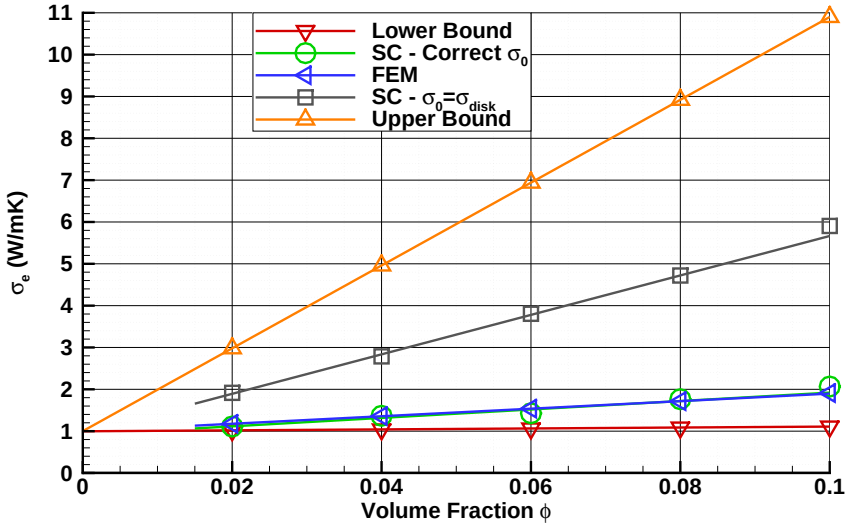

Figure 4.9: Disk Verification - Comparison between the effective thermal conductivities predicted by strong-contrast method and finite element method for isotropic microstructures loaded with disk-shaped inclusions. (Aspect Ratio = 10 and $\sigma_{disk}/\sigma_{matrix} = 100$)

method is proposed to minimize the effect of the reference medium on the solution. The proposed method formulates error between the predicted thermal conductivity and the unknown true thermal conductivity as a function of the reference phase properties and then finds its extremal points. It is argued that by choosing the properties of the reference phase on the neighborhood of these extremal points, the predicted effective properties will retain minimal error compared to the arbitrary selection of the reference phase argued by existing methods. In order to establish the validity of the proposed method, its results are compared with those from finite element simulations for three different microstructures consisting of tubular and disk-shaped inclusions. Good agreement between the proposed strong-contrast model predictions and the FEM calculations is observed for both cases.

5

Hybridization Effects

5.1 Introduction and Scope

Two computational models for evaluating the effective electrical/thermal conductivities of the polymer nanocomposites were proposed in the previous chapters. The predictions of these computational models for the polymer nanocomposites comprising a single type of filler nanoparticles (either CNTs or GNPs) were compared to some published results. As discussed earlier, the proposed models were originally developed for the hybrid nanocomposites with at least two different types of the filler nanoparticles. In the following chapter, these models are utilized to predict the effective electrical and thermal conductivities of such hybrid polymer nanocomposites filled with the cylindrical (CNTs) and the disk-shaped (GNPs) nanoparticles. Whenever possible, the model predictions are verified with the predictions of alternative approaches. In the first section of this chapter, the effective electrical properties of the hybrid nanocomposites are explored. In the second section, the effective thermal conductivity of such hybrid nanocomposites is explored. In each section, the model predictions for the hybrid nanocomposites are compared against corresponding predictions for nanocomposites with a single type of nanoparticles. Finally, the chapter is concluded with a summary of the important findings.

5.2 Hybrid Nanocomposite Electrical Properties

5.2.1 Percolation Threshold

To investigate the percolation threshold of the hybrid CNT/GNP/polymer nanocomposites, it was assumed that GNPs are the main conductive phase and CNTs are the auxiliary conductive phase and for this purpose the volume loadings of CNTs and GNPs were selected such that $\phi_{CNT}/\phi_{GNP} = 0.01$. A number of simulations are carried out for different loadings of GNPs based on the method described earlier in the chapter 3. The aspect ratio as the main geometrical parameter for a particle was varied to study its effect and each curve in the following figures represents certain simulation configuration according to the selected aspect ratio of the GNPs and the CNTs.

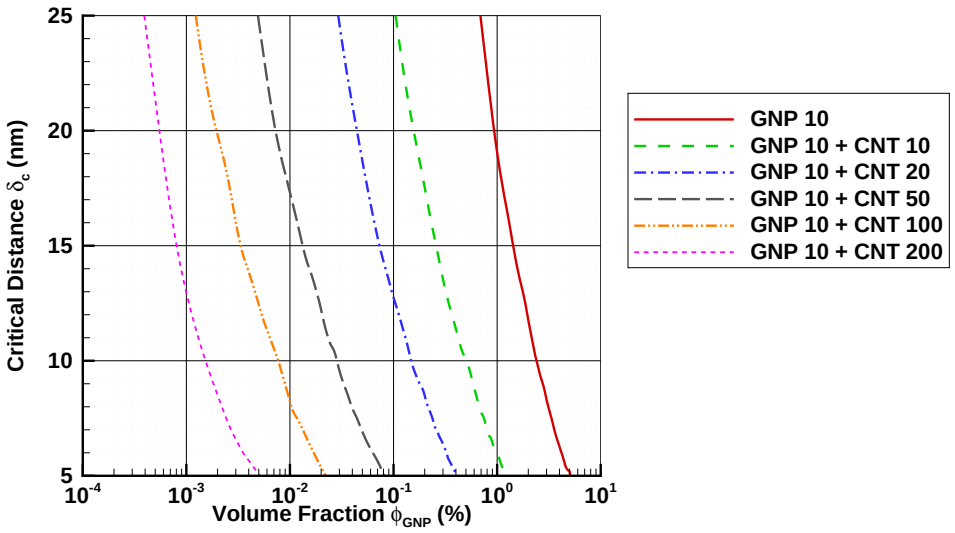

Figure 5.1: Hybrid Critical Distance for the Low Aspect Ratio GNPs - Predicted critical distance for the hybrid nanocomposites homogenously filled with low aspect ratio GNPs (10) and with the different aspect ratio CNTs ($\phi_{CNT}/\phi_{GNP} = 0.01$).

Figure 5.1 shows how the critical distance, as the main output of the simulation, varies with the CNT's aspect ratio while the GNPs are selected to maintain a low aspect ratio (aspect ratio = 10). Under ideal conditions, one might assign the tunneling distance to be a constant $\epsilon = 10\ nm$ (140). Therefore, according to this figure, the percolation threshold is about 2.5%*vol* when there is only GNPs and by adding auxiliary CNTs, it starts to shrink

down to almost 0.001%*vol*. This three orders of magnitude reduction in the percolation threshold by the addition of negligible amounts of CNTs can be ascribed to the high aspect ratio of CNTs (relative to the GNPs) and their complimentary tubular geometry which facilitates the formation of the global tunneling percolation network.

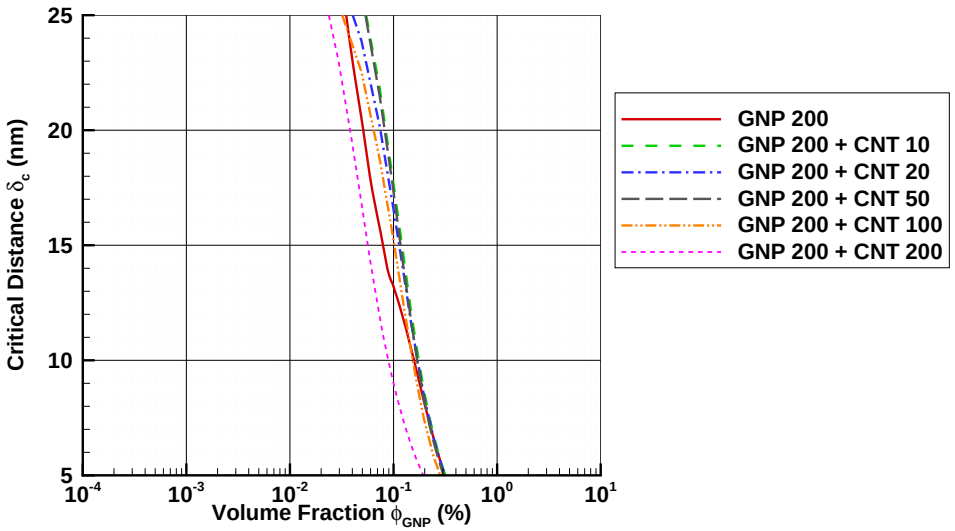

Figure 5.2: Hybrid Critical Distance for the High Aspect Ratio GNPs - Predicted critical distance for the hybrid nanocomposites homogenously filled with high aspect ratio GNPs (200) and with different aspect ratios CNTs ($\phi_{CNT}/\phi_{GNP} = 0.01$).

Figure 5.2 shows the variation of the critical distance for high aspect ratio GNPs when the other simulation conditions remain intact. It is observed that contrasting to the Figure 5.1 findings, the addition of low aspect ratio CNTs to the high aspect ratio GNPs has minimal contribution to the critical distance. By comparing Figure 5.1 and Figure 5.2, it is observed that the proper selection of the auxiliary CNTs reduces the percolation threshold; however, from the critical distance perspective, it is hard to draw conclusions about the electrical conductivity. The next section will be devoted to quantifying the electrical conductivity corresponding to these simulations. Finally, it should be noted that in practice CNTs and GNPs are not perfect straight cylindrical and disk-shaped particles that are perfectly distributed within the host polymer matrix as it is assumed here. Special considerations are needed to interpret the predictions under more realistic conditions. More discussions about these considerations will be provided in the validation chapter of this dissertation.

5.2.2 Electrical Conductivity

The electrical conductivity of the hybrid CNT/GNP/polymer nanocomposites was also calculated under the same settings of the simulation conditions as discussed in the previous section. Figure 5.3 shows the variation of the electrical conductivity for a hybrid nanocomposite homogenously filled with low aspect ratio GNPs (10) and different aspect ratio CNTs (under the same assumption of $\phi_{CNT}/\phi_{GNP} = 0.01$). It is observed that by adding tiny amounts of the auxiliary CNTs, the electrical conductivity is enhanced significantly and this enhancement is proportional to the relative CNT/GNP aspect ratio as well.

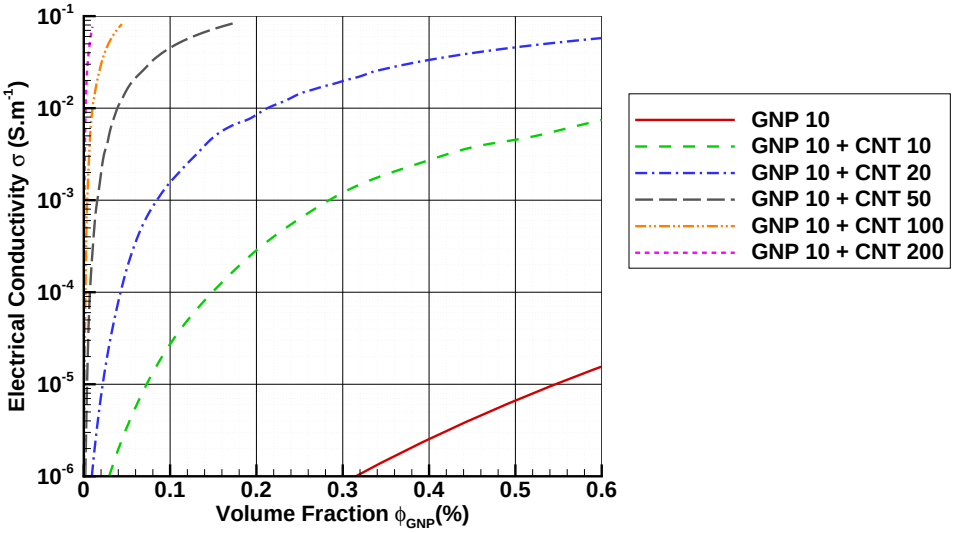

Figure 5.3: Hybrid Electrical Conductivity for the Low Aspect Ratio GNPs - Predicted electrical conductivity for the hybrid nanocomposites homogenously filled with low aspect ratio GNPs (10) and with different aspect ratio CNTs ($\phi_{CNT}/\phi_{GNP} = 0.01$).

Identical analysis was carried out for the hybrid nanocomposites with high aspect ratio GNPs and varying aspect ratio auxiliary CNTs. The results are shown in the Figure 5.4. This time the CNTs helped to enhance the electrical conductivity, however, not to the same extent predicted in Figure 5.3. By comparing Figure 5.3 and Figure 5.4, one could draw the conclusion that the hypothesis of the addition of CNTs as auxiliary phase into a network of GNPs inside a polymer host facilitates the formation of the tunneling network and, correspondingly, enhances the electrical conductivity. Similarly, these computational observations are only valid under ideal conditions.

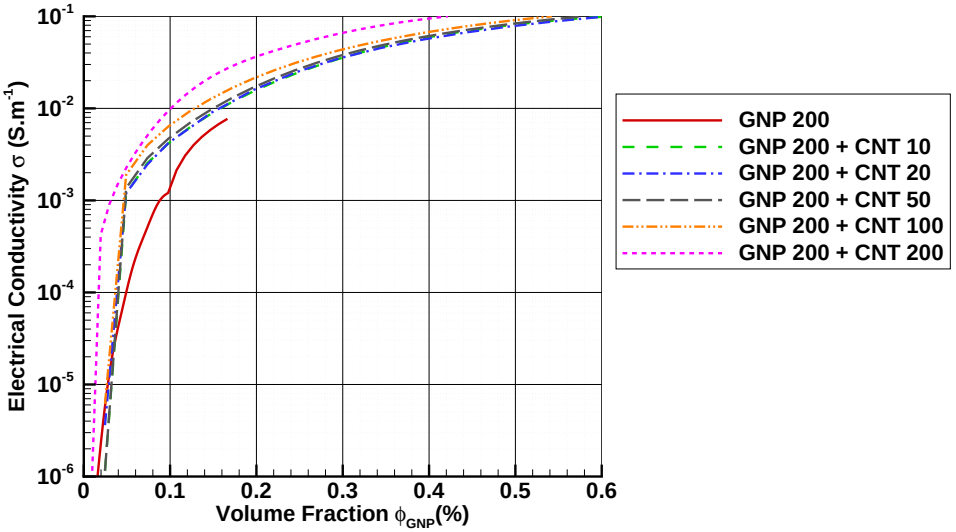

Figure 5.4: Hybrid Electrical Conductivity for the High Aspect Ratio GNPs - Predicted electrical conductivity for the hybrid nanocomposites homogenously filled with high aspect ratio GNPs (200) and with different aspect ratio CNTs ($\phi_{CNT}/\phi_{GNP} = 0.01$).

5.3 Hybrid Nanocomposite Thermal Conductivity

To investigate the potential advantage of the hybridization on the effective thermal conductivity of the polymer nanocomposites, a number of simulations were carried out in this section based on the method described earlier in chapter 4. For each simulation, the same volume loadings of the tubular (CNTs) and the disk-shaped (GNPs) inclusions with aspect ratio 10 were added and isotropically distributed into the simulation cell and the effective thermal conductivity was calculated by various methods. To evaluate the effective thermal conductivity through the formulation developed in chapter 4, the two-point correlation functions were evaluated from the Monte Carlo generated particle distributions. Figure 5.5 shows the two-point correlation functions for the 5%*vol* CNT and 5%*vol* GNP configuration with a total of 10%*vol* filler loading.

A unique value was selected for the inherent thermal conductivity of the tubes and the disks ($\sigma_{tube} = \sigma_{disk} = 100\ Wm^{-1}K^{-1}$) and to keep high contrast between the properties, the thermal conductivity for the polymer was selected to be $\sigma_{polymer} = 1\ Wm^{-1}K^{-1}$. The effective thermal conductivity was calculated by the corrected strong-contrast method, strong-contrast method with arbitrary reference ($\sigma_0 = \sigma_{disk}$), finite element method and

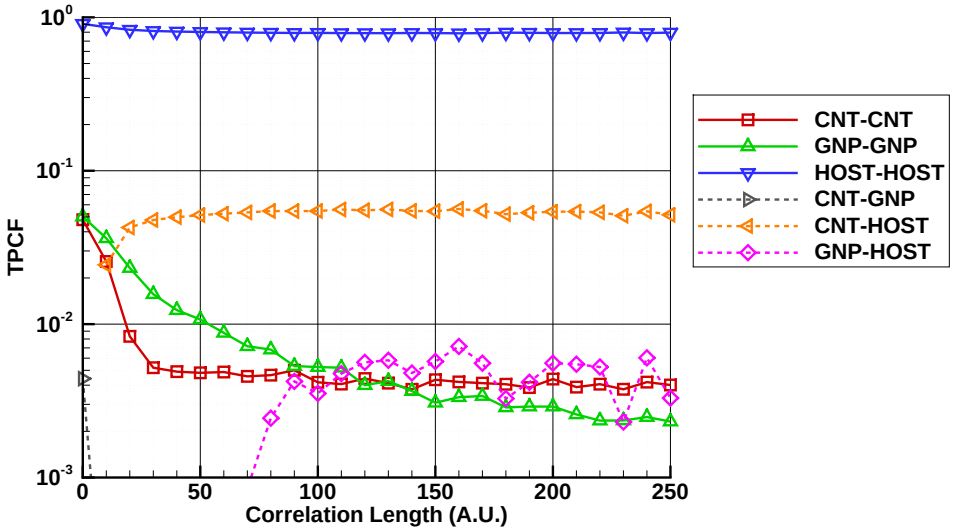

Figure 5.5: TPCFs of the Hybrid Nanocomposite - Two point correlation functions (TPCFs) of the hybrid nanocomposites loaded with 5%vol tubular and 5%vol disk-shaped inclusions homogenously distributed and isotropically dispersed. ($\phi_{tube}/\phi_{disk} = 1$ *and* $\sigma_{tube} = \sigma_{disk} = 100\sigma_{polymer}$).

the composite first order bounds. Figure 5.6 compares the effective thermal conductivity calculated by these methods. It can be observed that only the modified strong-contrast predictions are in perfect agreement with the finite element results.

The simulation results for the hybrid nanocomposites are also compared to the corresponding values for nanocomposites loaded only with the tubes or the disks. Figure 5.7 shows the modified strong-contrast predictions for each configuration and Figure 5.8 shows the corresponding values predicted by the finite-element method. It can be observed that for the selected aspect ratio (=10) both methods predict that the tubes and the disk are closely competing with each other, however, the tubes are slightly more effective (as predicted by the FEM). In addition, both methods are in agreement that the hybrid nanocomposites comprising equal volume fractions of both tubes and disks preform better for all volume fractions. This can be attributed to the formation of the more effective hybrid tube/disk network. It should be noted that these findings are based on the assumption of the ideal particle geometry and the perfect distribution/dispersion. Additionally, the current formulation does not take into account the inclusion/matrix interfacial thermal resistance which is another shortcoming. More discussions about these modeling drawbacks will be provided in the validation chapter of this dissertation.

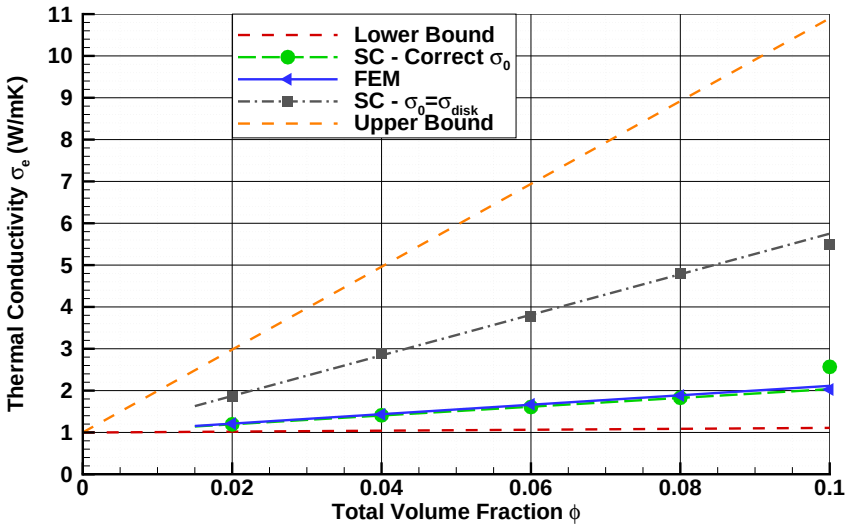

Figure 5.6: Effective Thermal Conductivity of the Hybrid Nanocomposite - Comparison between the effective thermal conductivity of the hybrid nanocomposite loaded with different volume loadings of the tubes and the disks predicted by different methods. ($\phi_{tube}/\phi_{disk} = 1$ *and* $\sigma_{tube} = \sigma_{disk} = 100\sigma_{polymer}$).

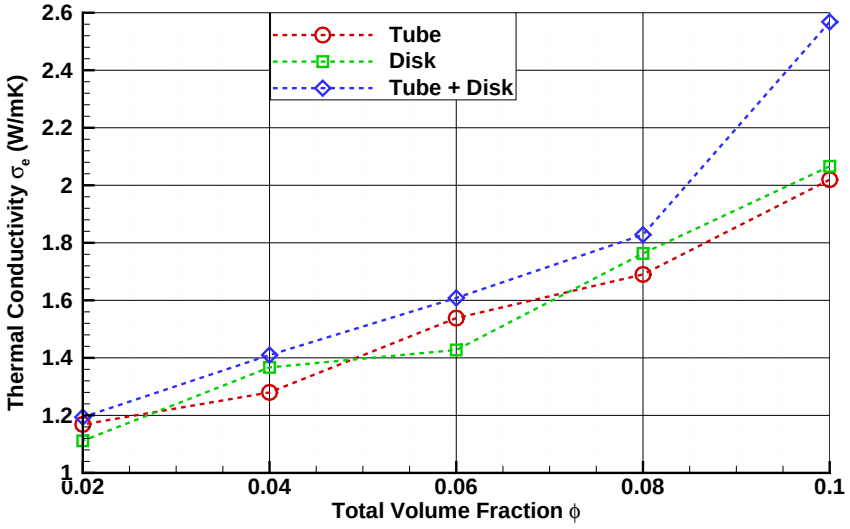

Figure 5.7: Corrected Strong-Contrast Predictions for the Hybrid Thermal Conductivity - Comparison between the effective thermal conductivity of the hybrid nanocomposite and the nanocomposites loaded only with the tubes or the disks predicted by the modified strong-contrast method. ($\phi_{tube}/\phi_{disk} = 1$ *and* $\sigma_{tube} = \sigma_{disk} = 100\sigma_{polymer}$).

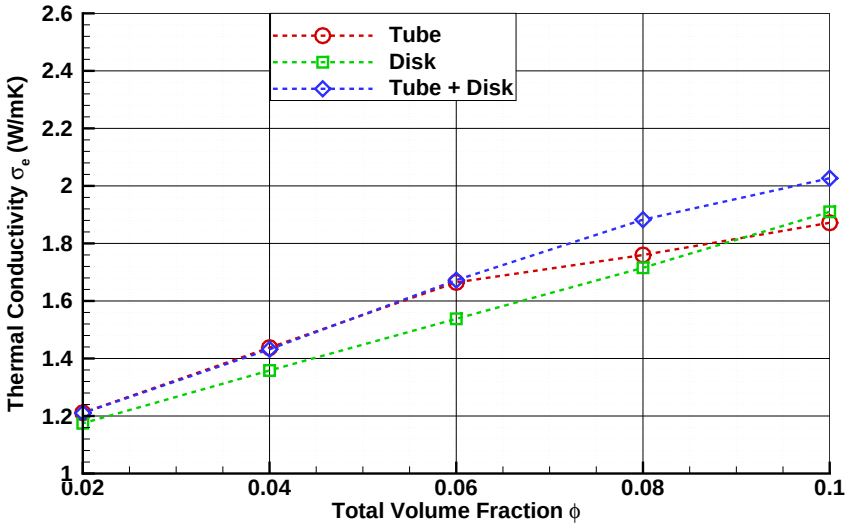

Figure 5.8: FEM Predictions for the Hybrid Thermal Conductivity - Comparison between the effective thermal conductivity of the hybrid nanocomposite and the nanocomposites loaded only with the tubes and the disks predicted by FEM method. ($\phi_{tube}/\phi_{disk} = 1$ *and* $\sigma_{tube} = \sigma_{disk} = 100\sigma_{polymer}$).

5.4 Conclusions

To investigate the effective electrical and thermal properties of the hybrid polymer nanocomposites, the two computational models developed in chapters 3 and 4 were employed. The proposed approaches were extended to the hybrid nanocomposites comprising two different types of inclusions. Using the proposed models, the effective electrical and thermal conductivities of the hybrid polymer nanocomposites comprising different volume fractions of CNTs and GNPs were calculated and compared in this chapter. It was hypothesized that the tubular and the disk-shaped geometries of CNTs and GNPs complement each other and, therefore, their synergistic combination facilitates the formation of a conductive network with better performance.

To investigate the hybridization effect, the effective electrical properties of a hybrid nanocomposite comprising GNPs as the main filler phase and CNTs as the auxiliary filler phase were studied. It was observed that the addition of negligible amounts of CNTs significantly enhances the electrical conductivity and consequently reduces the percolation threshold of these nanocomposites. These observations manifested with the fact that the relative CNT/GNP

aspect ratio plays a major role and the higher this quantity the better the transport properties are expected for the hybrid nanocomposite.

The effective thermal conductivities of the hybrid nanocomposites comprising identical volume fractions of tubular and disk-shaped inclusions were also investigated while the aspect ratio of the particles were selected to be identical. Similarly, it was observed that the hybrid nanocomposite outperforms the single-particle filler nanocomposites. Additionally, it was observed that the tubular/disk-shaped inclusions with identical low aspect ratios enhance the thermal conductivity of the nanocomposite to almost the same extent.

Finally, it was stated that the computational findings of this chapter should be acceptable when the CNTs and GNPs possess perfect geometries and there is no imperfection in their distribution/dispersion. Unfortunately, such perfect conditions can not be attained experimentally and, therefore, a number of modifications to the simulations are necessary to make them eligible for comparison with experimental results. To make these modification, a detailed feedback from experiments is necessary and the final portion of this dissertation, outlined in the next two chapters, is devoted to resolving these issues.

6

Experimental Study

6.1 Introduction and Scope

Several research groups have investigated carbon nanocomposites in the last decades. Now it is established that CNTs and GNPs are two allotropic species of carbon which can enhance the transport properties of the polymer nanocomposites namely the electrical conductivity and to a lesser degree the thermal conductivity. Looking for novel approaches to enhance the performance of these nanocomposites, recently hybrid nanocomposites comprising both CNTs and GNPs (or sometimes graphene nanosheets) were explored. In an early study, Xie et al (46) utilized the effective medium approach to compare the performance of GNPs and CNTs in terms of their ability to enhance the effective conductivity of their corresponding polymeric composites. This study came to the conclusion that GNPs are more effective than CNTs in enhancing the effective thermal conductivity. Later, Yu et al (47) explored, experimentally, a system of hybrid CNT/GNP/polymer nanocomposites. They observed that this hybridization provides a synergistic effect for the enhancement of the thermal conductivity. They attributed this enhancement to the formation of a more efficient percolation network with reduced thermal interface resistance. Furthermore, that study has reported that such hybridization reduces the effective electrical conductivity. In contradiction to these findings, Li et al (147) investigated similar hybrid nanocomposites and reported that such hybridization enhances the effective electrical conductivity. Similarly, Tung et al (168) studied CNT/graphene nanocomposites and concluded that a hybrid network of such fillers enhances the effective electric conductivity owing to a greater area of conductive pathways delivered by graphene. Later, Kim et al (169) also incorporated CNTs into thin films of graphene/polymer

and reported improved electrical conductivity. Similarly, Yan et al (170) reported that CNTs act as highly conductive flexible interconnects between graphene nanosheets which results in the improvement of the effective conductivity. In a similar study, Hong et al (149) developed a novel method to integrate CNTs into graphene nanosheets and reported excellent improvement in the electrical properties. Likewise, they attribute this enhancement in the electrical conductivity to the formation of the hybrid network. In a step further, in a recent study, Kumar et al (148), investigated hybrid CNT/GNP/polymer nanocomposites. This study also reported significant enhancement for both electrical and thermal conductivities upon hybridization. In an effort to explain this observation, this study suggested that GNPs protect the CNTs from fragmentation during high power sonication usually encountered during the dispersion task. Later, they concluded that these preserved high aspect ratio CNTs act as flexible highly conductive pathways for electrons and phonons to enhance the effective properties of the hybrid ternary nanocomposite systems. The contradictory findings of the referenced studies reveal the fact that hybrid ternary CNT/GNP/polymer composite systems are still in their infancy stage of development. Rationally, a more controlled condition is required to come to the right conclusion about the potential performance of these systems. To shed more light on this relatively vaguely investigated hybrid composites, in the following chapter hybrid CNT/GNP/polymer nanocomposites are probed experimentally. In order to investigate the importance of the effective parameters, the comparison between the current experimental observations and the relevant computational findings from the previous chapter are evaluated. Furthermore, this chapter's findings will serve as means for validation of the proposed models in previous chapters. In the following section, the materials and methods are listed. Later the experimental procedures , measurements and observations are reported.

6.2 Materials and Methods

6.2.1 Design of Experiment

To study the benefits of the hybridization a number of CNT/polymer, GNP/polymer and hybrid CNT/GNP/polymer nanocomposites specimens are processed. For the CNT/polymer and the GNP/polymer specimens five different configurations are chosen comprising $1, 2, \cdots, 5$ %wt of the CNTs and the GNPs, respectively. For the hybrid CNT/GNP polymer specimens

also five different configurations were selected; each of them comprising (X)%wt GNP and $(X/10)$%wt CNT were $x = 1, 2, \cdots, 5$.

6.2.2 Raw Materials

Exfoliated graphite nanoplatelets (x-GNPs) were supplied by XG-Sciences, Inc., with average particle diameter of 5.0 microns and thickness of approximately 6-8 nanometers (i.e. nominal aspect ratio = 650-850). Short length multiwall carbon nanotubes (MWCNTs) were supplied by Cheap Tubes, Inc., with the outer diameter of approximately 8 nm and with the length in the range 0.5 to 2.0 microns (purity > 95%). The hosting polymer matrix is a bisphenol-A epoxy vinyl ester resin (Ashland Derakane 411-350) supplied by Ashland, Inc., along with proper hardener (Norox MEKP-925H) and promoter (Cobalt Naphtenate-6%) according to the supplier's recommendation. The high purity non-ionic surfactant Triton X-100 was supplied by Sigma-Aldrich. Finally, a number of other chemicals (with high purity > 99%) including Acetone, Ethyl alcohol etc., were also supplied by commercial laboratory supplies providers.

6.2.3 Mixing and Homogenization Equipments

In order to ensure a good dispersion and distribution of the nanoparticles within the nanocomposite specimens, a number of equipments were utilized for the mixing and homogenization. An IKA Ultra-Turrax T18 basic high speed dispersion unit was utilized for high speed dispersion and homogenization. A Vibra-Cell VCX 500 tip-sonicator was utilized for the sonication process. During the processing whenever needed disposable wooden stick was utilized to mechanically mix the ingredients, standard tabletop ultrasonication bath unit was also utilized and a tabletop high speed centrifuge device was utilized for particle separation and sedimentation during the neutralization and washing processes.

6.2.4 Processing Method

In order to eliminate, or at least reduce, the metallic impurities (mainly catalytic metals) and to add some functional groups to facilitate the dispersion, the required amount of CNTs was weighed and then soaked in a 1.0 M nitric acid solution for three hours within ultrasonication bath at $40°C$. Afterward the CNTs were neutralized and washed with deionized (DI) water

three times. Every time the CNT conglomerates and sediments were re-dispersed into the DI water and bath-ultrasonicated for 2 minutes and then centrifuged to form sediments at 13K RPM. Finally, the neutralized CNTs were dried in an oven furnace at $70°C$. The dried CNTs were crushed carefully with a ceramic mortar into a fine powder. For each specimen, the needed amount of the as-prepared CNTs were weighed and then mixed with 3 ml of Acetone followed by 5 minutes of tip sonication in 20% amplitude at room temperature. After 1 minute of tip-sonication, 1 ml Triton X-100 was added to the solution to enhance the dispersion and to prevent the re-aggregation. In order to prevent the CNT-Acetone mixture from conglomeration and sedimentation prior to its usage, the suspension was stored in a bath sonicator and after every 1 minute it was tip-sonicated for 10 seconds. The required amount of GNPs were also weighed and gradually added directly to the resin using the high speed dispersion unit under 100% rotation speed. The mixing process was followed up by another 30 minutes of homogenization inside a water bath at room temperature. After then, the dispersed CNTs were added drop-wise to the as-prepared resin-GNPs suspension and the mix was homogenized for another 30 minutes. Finally, to improve the dispersion and distribution, the as-prepared mixture was tip-sonicated for another 30 minutes in a water bath. To ensure proper gelling time, after a number of trials and errors, the proper amounts of curing agent and promoter were weighed and added to the mixture and mechanically stirred followed by one minute homogenization. The CNT/GNP/resin suspension was poured into cylindrical glass tubes and stored under vacuum in a desiccator for three hours for proper degassing and to ensure initial curing at room temperature. Finally, the nanocomposite specimens were post-cured in a convention oven for 24 hours at $75°C$ and were cut into 2.5 mm thick disks using a high precision diamond saw. Figure 6.1 shows the schematic of the mixing and homogenization process. For the one filler phase CNT/epoxy and the GNP/epoxy specimens identical processing procedures were carried out.

6.2.5 High Resolution Microscopy

In order to study the quality of dispersion and distribution of CNTs, GNPs and their hybrids inside the nanocomposite cured specimens, a thin 0.1 mm disk sample was sliced and the morphologies of the cryo-fractured cross section were investigated using electron microscopy. For this purpose, a LEO (Zeiss) 1550 field effect scanning electron microscopy (FESEM) was utilized. A number of micrographs were generated from different locations on the cross-section under different magnifications. A FEI Helios 600 Nanolab dual-beam

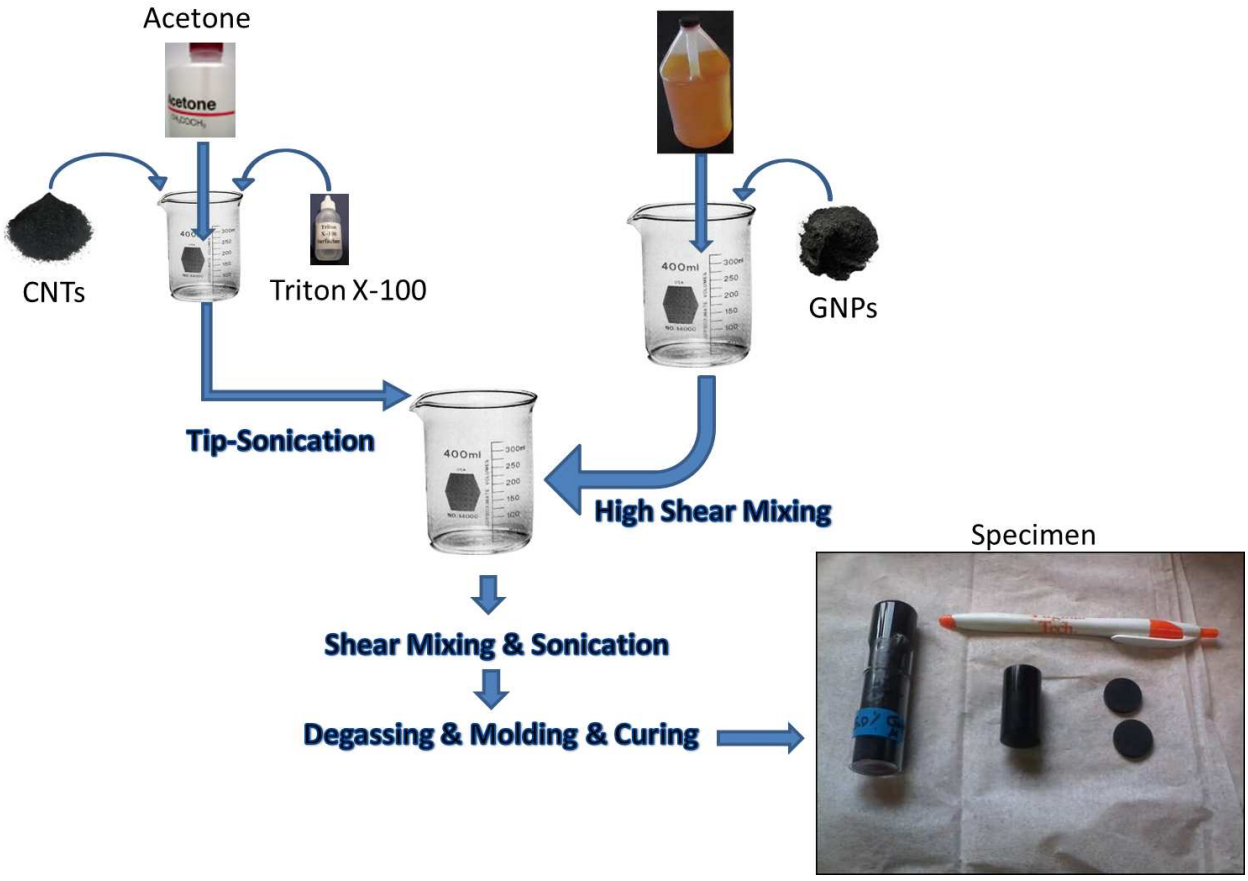

Figure 6.1: Schematic of Mixing Procedure - The schematic of mixing/homogenization process utilized for CNT/GNP/epoxy specimens.

electron/focused ion-beam (FIB) was also utilized for serial sectioning and microstructure reconstruction purposes.

6.2.6 Electrical and Thermal Conductivities Measurements

The electrical conductivities of the different nanocomposite specimens were measured using a 4-point probe station equipped with a Keithley 2001 digital multimeter with an equivalent measurement uncertainty of 1.68×10^{-9} S/m at the low conductivity range and 1.66×10^{-7} S/m at the high conductivity range (these values can be equally interpreted as the signal to noise ratio at the corresponding ranges). For this purpose, at least two disk-shaped specimen were sectioned from each nanocomposite configuration and their flat surfaces were cleaned with isopropanol alcohol. The surface resistance was measured at 20 different sites on both sides of each specimen. The averaged value is reported as the electric resistance. The thermal conductivity of the specimens was measured by transient plane source technique utilizing a Hot disk AB device. For this purpose, a Kepton hot-disk probe was sandwiched in-between two flat surfaces of two disk-shaped specimens after cleaning them with isopropanol alcohol. Using a mechanical fixture, the specimen/probe/specimen stack was loaded uniformly to ensure proper contact and to minimize the air gap and then the thermal conductivity was measured. For each configuration, the thermal conductivity was measured five times and averaged.

6.3 Results and Discussions

6.3.1 Scanning Electron Microscopy (SEM)

Figure 6.2 shows that in a cryo-fractured cross section, GNPs can be recognized by their thin crack shaped morphology. GNPs possess low out-of-plane bending stiffness and during mixing and homogenization they bend into crumpled shaped structures. This wrinkling in effect diminishes their actual aspect ratio to smaller values compared to the nominal value.

Figure 6.3 shows the cross section of GNP/epoxy specimen under different magnifications. The low magnification micrograph (Figure 6.3- a) shows that the GNPs are properly distributed within the epoxy matrix. Higher magnification micrographs (Figure 6.3- b and c) show how the GNP particles cooperate to form a local percolation network. This figure

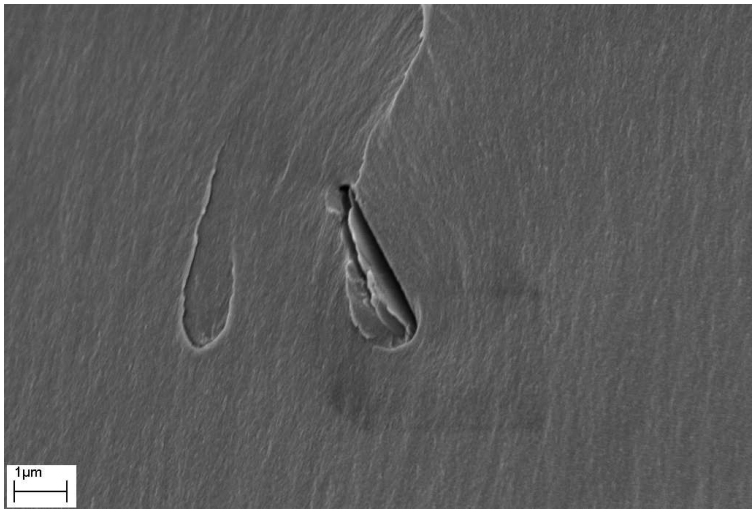

Figure 6.2: GNP/epoxy Micrograph - Scanning electron microscopy image of the GNP/epoxy specimen with 1%wt GNPs shows the crack-shaped cross section of GNPs residing in the epoxy matrix.

also confirms that the actual GNPs are not perfect disk-shaped nanoparticles; as was assumed earlier for the computational models. Usually shear mixing forces (e.g. tip-sonication process) can break them into smaller fragments and deform their shapes.

Each GNP is composed from several layers of graphene stacking on top of each other by attractive inter-layer interactions. Similarly, these forces increase the tendency of the GNPs aggregate. Figure 6.4 shows a GNP aggregate composed of 5 to 6 GNPs. Figure 6.5 similarly shows a GNP aggregate composed of 5 GNPs. On the top left corner of this figure, a fully exfoliated GNP can be observed as well. Close examination of the SEM images of the different specimens reveals that for the practiced mixing method, small GNP aggregates are abundant within the specimen. A simple analysis showed that the number of GNPs in each aggregate follows a normal distribution with an average value of 5 and a standard deviation of 3.

Figure 6.6 shows the SEM micrograph of a CNT/epoxy specimen. It can be observed that the proposed mixing technique disperses CNTs well within the specimens with lower loading content of CNTs. However, at higher loadings of CNTs ($> 2.0\%wt$), the practiced method produces CNTs aggregates. According to the Figure 6.7 and similar SEM images the formation of CNT aggregates is more noticeable for the configurations with high CNTs loadings. From experimental point of view, perfect mixing of samples with high CNT loading ($> 2.0\%wt$) is a challenging task. In these specimens, microscale voids and microbubbles are

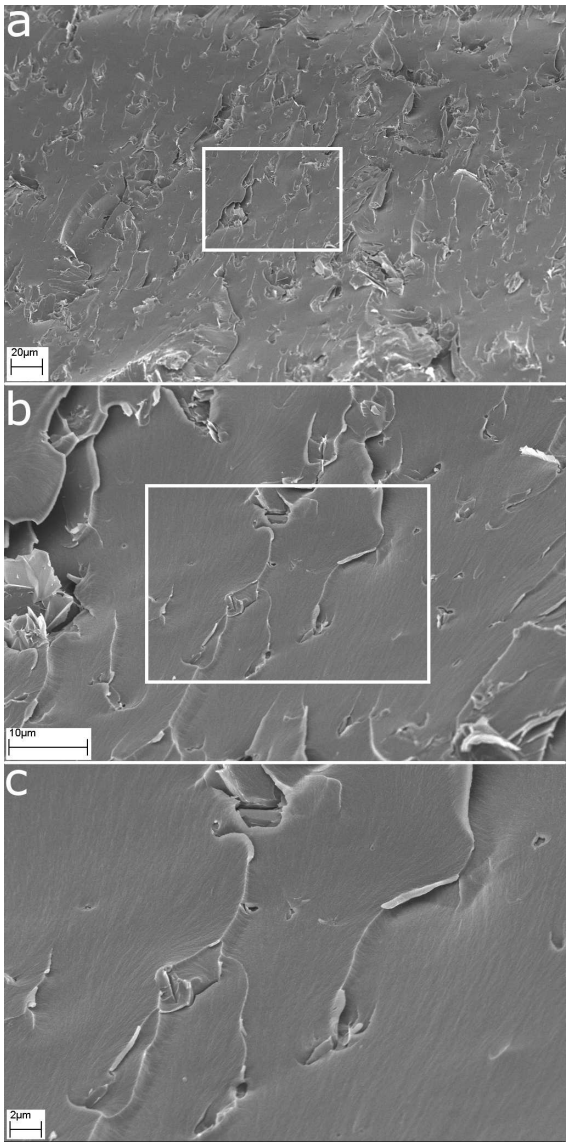

Figure 6.3: GNP/epoxy Distribution - Scanning electron microscopy image of the GNP/epoxy specimen with 1%wt GNPs shows their distribution and the formation of the local percolation network.

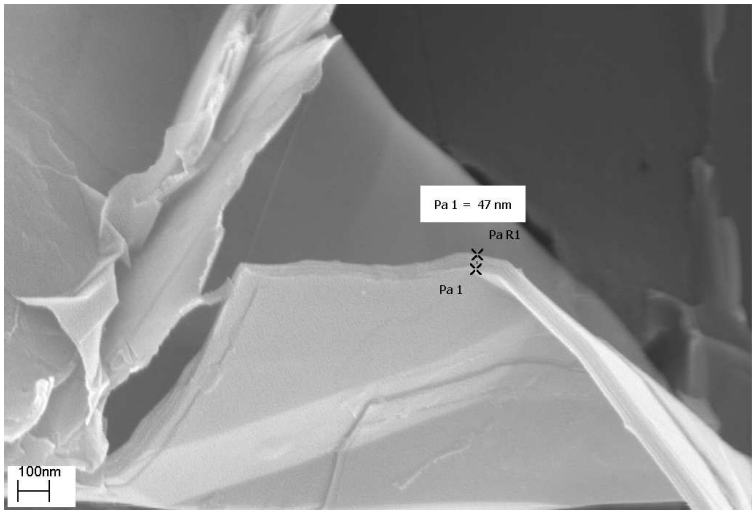

Figure 6.4: GNP Aggregate - Scanning electron microscopy image of GNP/epoxy specimen with 1%wt GNP shows an aggregate composed from 5-6 GNPs.

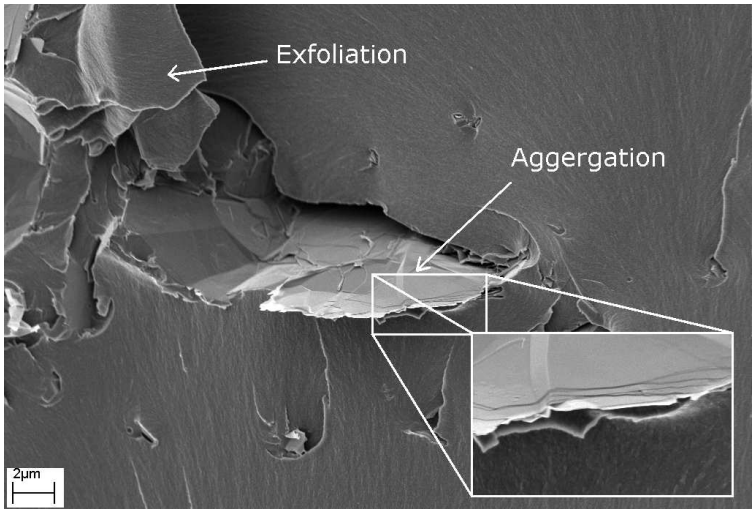

Figure 6.5: GNP Aggregate - Scanning electron microscopy image of GNP/epoxy specimen with 1%wt GNP shows an aggregate composed from 5 GNPs and a fully exfoliated GNP in the top-left corner.

also apparent.

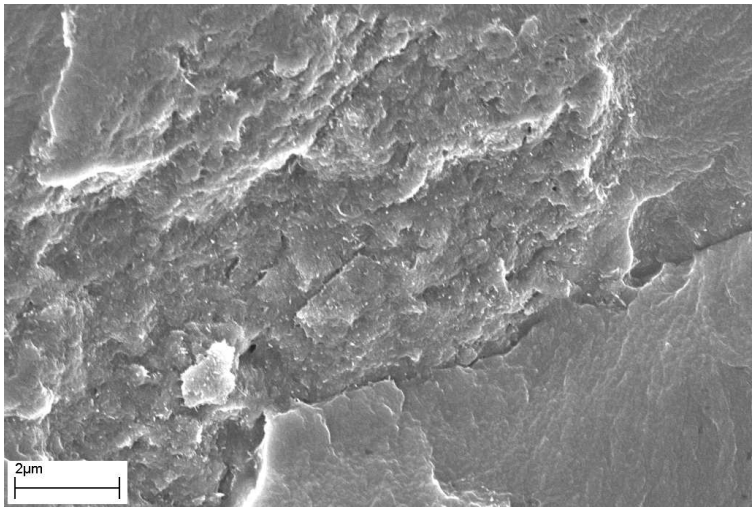

Figure 6.6: Dispersion State of CNT/epoxy - Scanning electron microscopy micrograph of the CNT/epoxy specimen with 1%wt CNTs confirms good dispersion of CNTs in the epoxy matrix.

Figure 6.8 shows how CNTs act as interconnects to form a percolation network between GNPs. For the CNT/GNP/epoxy nanocomposite configuration, CNTs act as conductive flexible pathways between large high surface area GNPs. These two species synergistically cooperate to form the hybrid percolation network and consequently expected to enhance the electrical and thermal conductivity of the specimen. The measurement of the diameter and the length of this flexible pathways reveals the fact that even when highly dispersed, a number of CNTs are forming a nanofilament. Figure 6.9 shows that CNT aggregates are also forming in the hybrid configurations with low CNT loadings. However, it is relatively hard to locate them in such specimens. The formation of such CNT aggregates is not desirable, however, these aggregates can also contribute to the percolation network as shown in Figure 6.9.

6.3.2 Focused Ion Beam (FIB)

In order to gain more insights about the morphology of the aggregated CNTs, and later to reconstruct such aggregates properly into the computational studies, a FIB study was carried out for the 5%wt CNT/epoxy specimen. Figure 6.10 shows a CNT aggregate selected as the designated site for the FIB study.

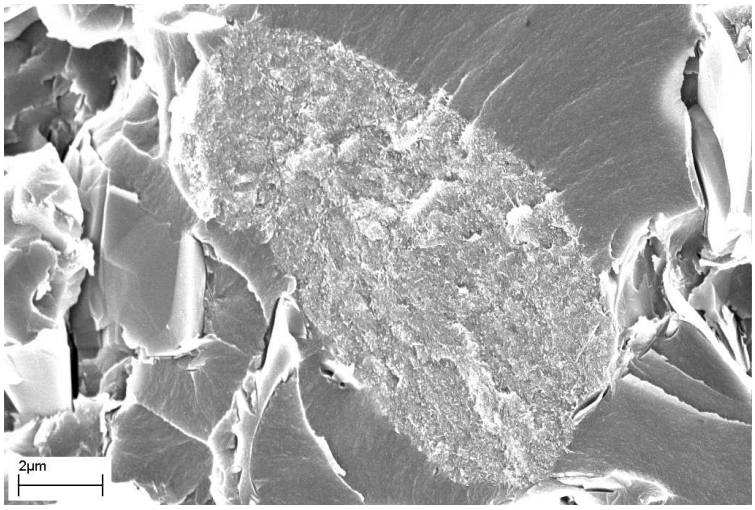

Figure 6.7: Formation of Aggregates in CNT/epoxy - Scanning electron microscopy micrograph of the CNT/epoxy specimen with 5%wt CNTs shows that for higher loadings CNTs start to form large aggregates.

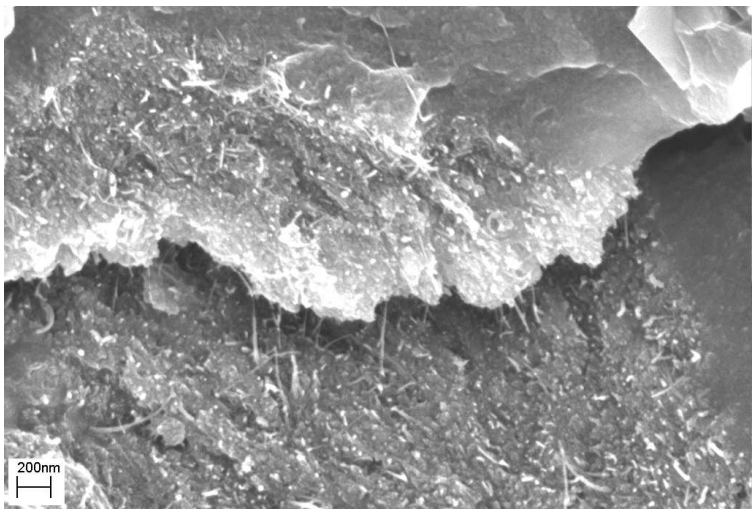

Figure 6.8: CNT as a Flexible Pathway - Scanning electron microscopy micrograph of the CNT/GNP/epoxy specimen with 5%wt GNPs and 0.5%wt CNTs shows that CNTs are acting as a flexible connector between GNPs.

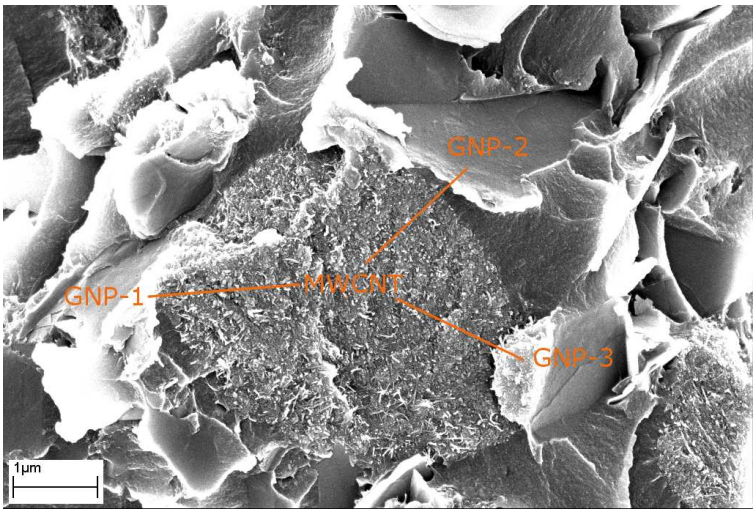

Figure 6.9: CNT Aggregate Contribution - Scanning electron microscopy micrograph of the CNT/GNP/epoxy specimen with 5%wt GNPs and 0.5%wt CNTs shows that CNT aggregates can contribute to the percolation network.

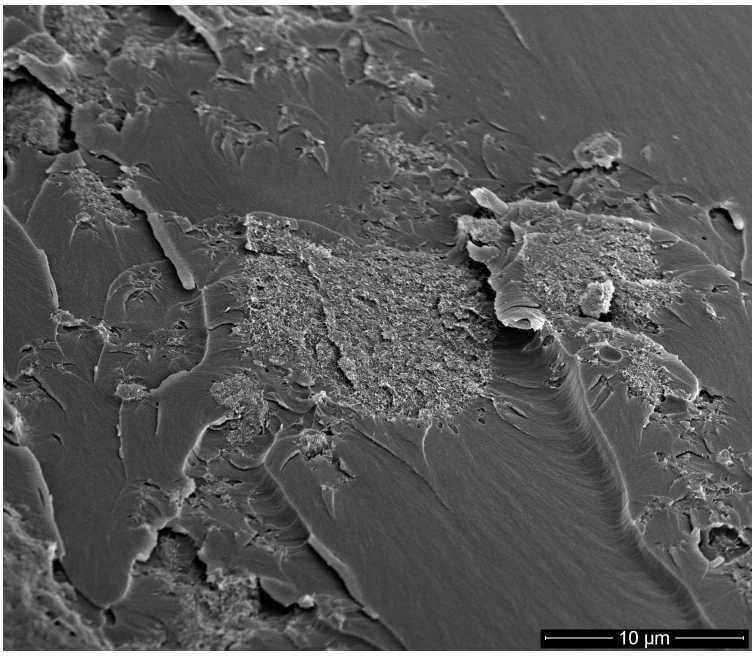

Figure 6.10: CNT Aggregate under FIB - Scanning electron microscopy micrograph of the CNT/epoxy specimen with 5%wt CNTs shows a CNT aggregate

To protect the aggregate and to later reduce undesirable curtaining effects by the high intensity focused ion beam, a thin platinum film was deposited so that it covers at least half of this aggregate. Figure 6.11 shows the aggregate after the deposition of the platinum thin film.

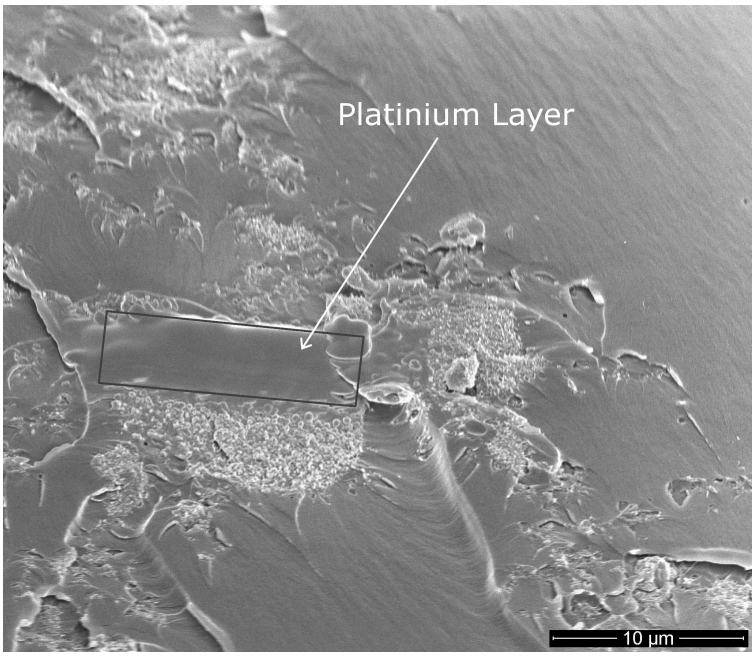

Figure 6.11: Platinum Layer - Scanning electron microscopy micrograph of the CNT/epoxy specimen with 5%wt CNTs shows a CNT aggregate protected with a platinum layer.

A part of the aggregate was engraved with highly focused ion-beam. For this purpose, initially a high-power ion beam was utilized to roughly mark the boarders of the desired area. Following that, a low-power ion beam was brushed over a thin section of the edge of the engraved area to leave a clean layer. Figure 6.12 shows the engraved aggregate after these two steps.

Figure 6.13 shows a closeup image from the engraved area. The CNTs coated with the platinum film can be detected easily. However, the CNTs are visible inside the polymeric area. There should be a good contrast between the CNTs and the surrounding polymeric area to detect them within a SEM image. In practice, the surface morphology and the extent of the contrast between the atomic number of the composing elements are the two main sources that contribute to the contrast variation in a SEM image. In this case, the engraved surface is atomically flat so the contrast originating from the morphology mechanism is irrelevant. In the platinum covered area, there is a significant atomic number difference between the

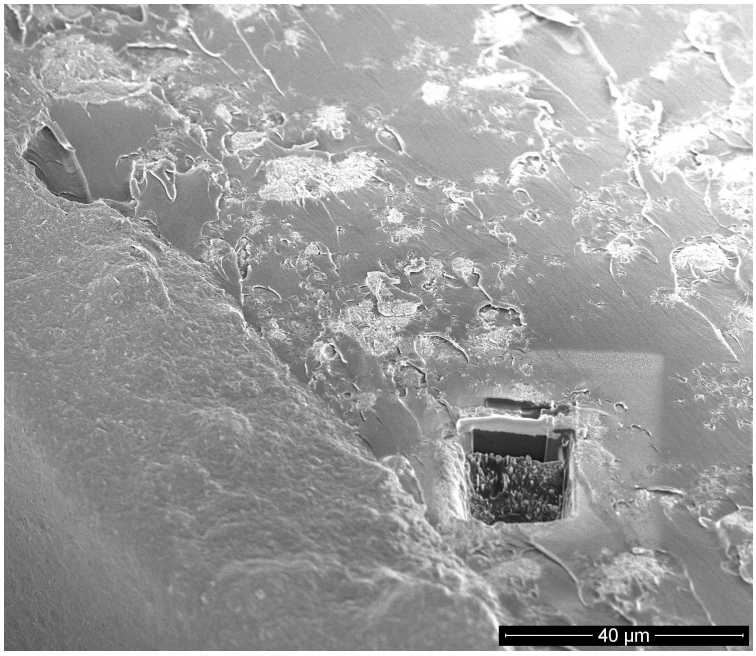

Figure 6.12: FIB Engraving - Scanning electron microscopy micrograph of the CNT/epoxy specimen with 5%wt CNTs shows a CNT aggregate after FIB engraving.

CNTs (carbon) and the surrounding platinum, therefore, the CNTs can be detected with much ease. However, within the epoxy region, the low atomic number difference between the CNTs and the epoxy (mostly carbon) weakens the contrast mechanism and therefore the CNTs can not be separated from the polymer matrix. Similar FIB studies conducted on other locations in the specimen supported this hypothesis and deemed this part of the study unsuccessful.

6.3.3 Electrical Conductivity

Figure 6.14 reports the average electrical conductivity of the specimens measured by the four-point probe method. The electrical conductivity for 1, 2 and 3 %wt GNP/epoxy samples are not reported in this figure since the minimum possible reading by the utilized equipment was $10^{-7}S/m$ which was more than the conductivity of these specimens. Similar limitation was applicable to neat resin specimen and thus in the Figure 6.14 the reported electrical conductivity for the neat epoxy specimen was borrowed form the literature (171).

By taking $10^{-7}S/m$ as the reference threshold for the electrical conductivity, it can be observed that the percolation threshold is 0.6%wt for CNT/epoxy specimens, 0.9%wt for

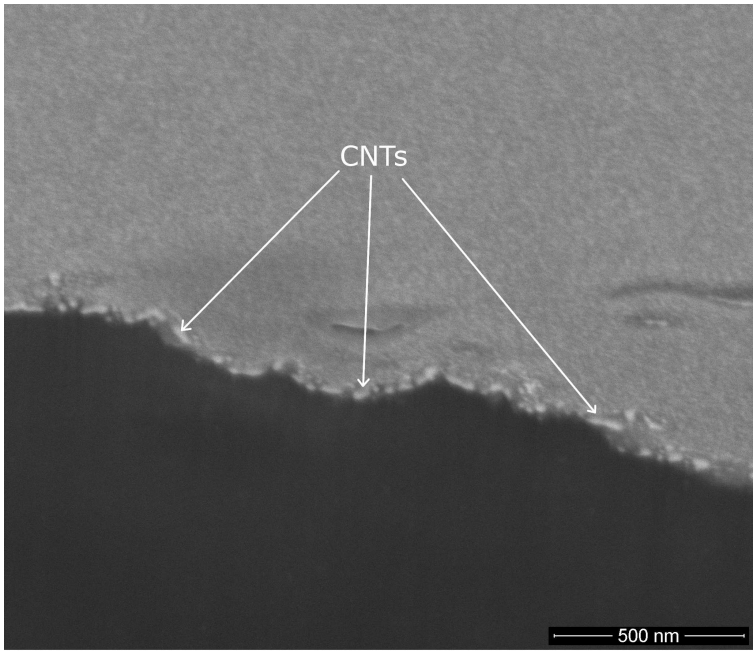

Figure 6.13: FIB Close-up - Scanning electron microscopy micrograph of the CNT/epoxy specimen with 5%wt CNTs. Low atomic number difference prevents CNTs to be observed on the engraved area.

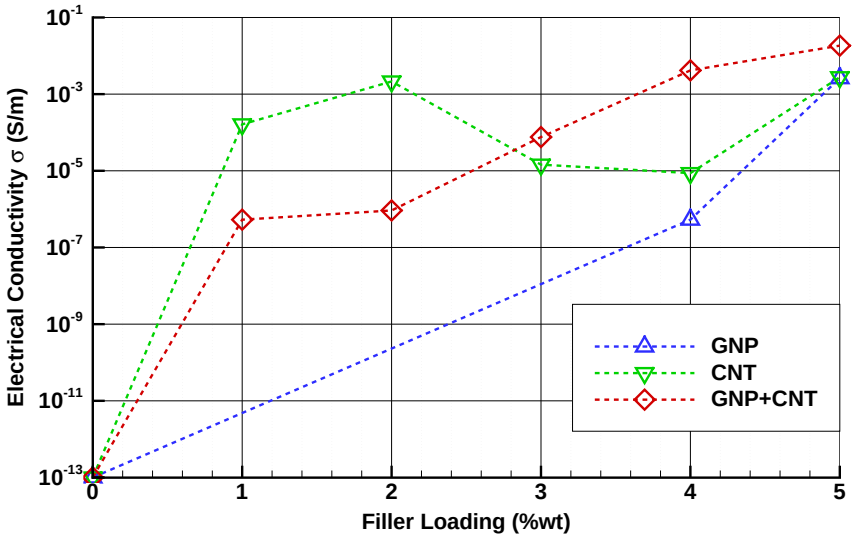

Figure 6.14: Electrical Conductivity Measurement - The electrical conductivity of CNT/epoxy, GNP/epoxy and CNT/GNP/epoxy specimen measured by the four point probe technique.

CNT/GNP/epoxy specimens and approximately about 3.6%wt for GNP/epoxy specimens (a rough estimate for this case). In general, CNT/epoxy specimens exhibit highest electrical conductivity for lower loadings compared to two other configurations. However, for the higher CNT loadings the conductivity curve follows no specific trend. This can be attributed to the naturally occurring plateau upon percolation and more importantly to the formation of the large aggregates in high CNT content which is also observed by the morphological study. Among all the different configurations, the GNP/epoxy specimens attains the minimal electrical conductivity. This is mainly because GNPs, as 2D particles, are forming a poor percolation network compared to the more flexible CNTs. Finally, it can be observed that the addition of minute amounts of the CNTs as the auxiliary conductive phase to the GNP/epoxy system reduces the percolation threshold by 50%. This is a significant improvement for the percolation threshold. Practically, for each GNP loading ($X\%wt$), the addition of ($X/10\%wt$) CNTs enhances the electrical conductivity by orders of magnitude. This notable enhancement in the electrical conductivity of the hybrid configurations can be attributed to the formation of the highly efficient hybrid CNT/GNP networks.

6.3.4 Thermal Conductivity

Figure 6.15 depicts the thermal conductivity of the specimens as measured by the hot disk method. It can be observed that the CNT/epoxy specimens attains minimal thermal conductivity compared to the two other configurations. The thermal conductivity curves for the CNT nanocomposite specimens reaches a plateau around 1%wt with minimal enhancement in the properties. Three reasons can lead to this observation. First CNTs are more flexible, than GNPs, and therefore are more vulnerable to bending during mixing into the polymer and in return their effective aspect ratio is reduced. Second, the formation of the CNT aggregates at higher loadings prevents further enhancement of the thermal conductivity and finally, the high CNT/CNT interface resistance is also a possible reason that restricts the effective thermal conductivity of the percolation network in these specimens. However, for the same weight %, the GNP/epoxy specimens possess better thermal conductivity owed to their higher surface area compared to the CNTs, their more robust structure and their lower interface resistance. Finally, it can be observed that the hybrid CNT/GNP/epoxy specimens outperform the other two single nanofillers configurations, with more than two-fold enhancement in the thermal conductivity of hybrid 5%wt CNT/GNP/epoxy specimen compared to the neat epoxy. This enhancement could be attributed to the formation of a

more efficient hybrid CNT/GNP network in this specimens which reduces the undesirable particle/polymer interface resistance effects. The CNT acting as interconnects in-between GNPs, as observed by SEM, enhances the conductivity further.

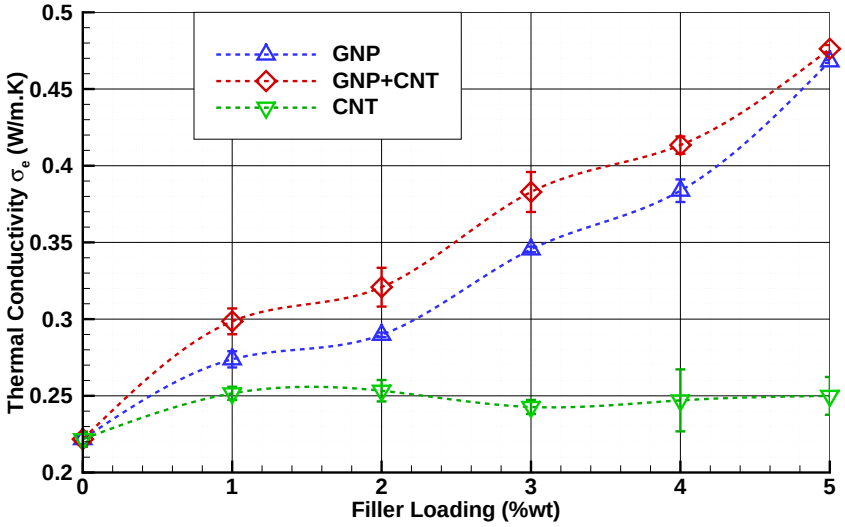

Figure 6.15: Thermal Conductivity Measurement - The thermal conductivity of CNT/epoxy, GNP/epoxy and CNT/GNP/epoxy specimen measured by the hot disk technique.

6.4 Conclusions

To investigate the potential advantages of the hybrid CNT/GNP nanocomposites and also to shed more light on the physics of these ternary systems, a number of different nanocomposites based on single and multiple nanofillers were processed and characterized. A multistep mixing and homogenization protocol was developed to minimize the nanoparticles aggregation and to enhance the state of the particle dispersion/distribution. The electrical and thermal conductivities of the different specimens were measured. A detailed investigation using SEM and FIB was carried out to probe the morphologies of the nanocomposite and to assess the dispersion/de-agglomeration of the nanofillers within the different configuration nanocomposites. It was observed that CNT/epoxy specimens provide better electrical conductivity compared to the GNP/epoxy specimens. However, the GNP/epoxy specimens are more effective thermal conductors owing to the high surface areas of the GNPs. It was also observed that for higher loadings of CNTs ($> 2.0\%wt$), the formation of aggregates

limits the properties improvements in the CNT/epoxy specimens. Finally, it was observed that the addition of minute amounts of CNTs (10% of the GNP loading in each specimen) as an auxiliary conductive phase to the GNP/epoxy specimens synergistically enhances the electrical and the thermal conductivities for these specimens compared to the CNT/epoxy or the GNP/epoxy nanocomposites. This observation could be attributed to the formation of a more efficient CNT/GNP networks with boosted performance. The formation of the synergistic CNT/GNP network was also observed by the SEM micrographs indicating that the CNTs can play the role of interconnects between different GNPs. Finally, according to this study, in general the addition of CNTs and GNPs to an insulating polymer enhances its electrical conductivity by orders of magnitude, however, a much lower enhancement in the thermal conductivity should be expected for such systems. This can be ascribed to the existence of high thermal resistance in the particle/polymer interfaces and to the relatively lower contrast between their inherent thermal properties.

7

Validation Study

7.1 Introduction and Scope

In chapters 2 and 3, the underlying physics of the electrical properties of the polymer nanocomposites were elucidated and a novel model for the assessment of these properties was proposed. During this study, the predictions of the proposed approach were validated with some published experimental studies selected from the literature for the single-inclusion based nanocomposites (CNT/polymer and GNP/polymer). Later in chapter 4, a modified strong-contrast formulation for evaluating the effective thermal conductivity of the nanocomposites was introduced. The predictions of the proposed method was verified with alternative computational approaches (e.g. FE) for the single-inclusion based nanocomposites (based on uniform shaped tubular or disk inclusions). In chapter 5, these two proposed models were employed as tools to explore the electrical and thermal properties of the hybrid nanocomposites with combinations of CNTs and GNPs under ideal simulation conditions. To validate the predictions of these models for the hybrid nanocomposites, an experimental study was conducted in chapter 6. According to the experimental observations, both CNTs and GNPs have the tendency to form aggregates and the mixing and homogenization process deforms the particles and reduces their effective aspect ratios. In order to fair the comparison between the modeling predictions and the experimental measurements, one should consider such effects in the simulations. In the following chapter, the experimental findings of the previous chapter are utilized to validate the proposed electrical and thermal conductivity models. The first section of this chapter discusses how the geometric imperfections (e.g. particle entangling, aggregation, deformation etc.) could be accounted for in

Table 7.1: The physical and geometrical properties of CNTs, GNPs and epoxy utilized in the simulations.

	Designation	**Nominal Diameter**	**Nominal Length/Tickness**	**Density** ($gr.cm^{-3}$)	**Electrical Resistivity** ($\Omega.cm$)	**Thermal Conductivity** ($Wm^{-1}K^{-1}$)
CNT	Short MWCNTs Cheaptubes	8 nm	0.5-2 μm	2.1	≈ 1	10^3
GNP	xGNP-grade M XG Sciences	5 μm	6-8 nm	2.2	$\approx 5 \times 10^{-5} \parallel$ and $\approx 1 \perp$	$3 \times 10^3 \parallel$ and $6 \perp$
Epoxy	Derakane 411-350 Ashland	N/A	N/A	1.046	$\approx 10^{15}$	0.22

the simulations. The second section is devoted to the validation of the proposed electrical conductivity model. In the third section the validation study of the thermal conductivity model is reported. Finally, the chapter ends with some concluding remarks.

7.2 Modeling Considerations

7.2.1 Geometrical and Physical Properties

Table 7.1 lists the relevant properties of the CNTs, GNPs and the epoxy utilized in the experimental study which will be utilized in the simulations conducted in this chapter. The geometrical dimensions of the CNTs and GNPs are selected in accordance with their nominal values. For each nanocomposite configuration, the weight fractions of the CNTs and GNPs are selected to mimic those in the experiments and whenever needed the corresponding volume fractions were calculated using the densities reported in this table. All the physical properties are listed from the raw materials manufacturer's data sheets except for the thermal conductivity of the CNTs which was not reported by the Cheap Tube, Inc, the corresponding values were rather adopted from the literature (23). For the epoxy, the thermal conductivity was measured experimentally as discussed in chapter 6 and the electrical conductivity was adopted from the literature (171).

7.2.2 Particle Aggregations and Deformation

Under the ideal conditions assumed in the previous chapters, CNTs and GNPs were treated as perfect straight cylindrical-shaped particles with known dimensions. However, practically

in the bulk powder forms, both CNTs and GNPs are usually clustered into large aggregates which are formed by several nanoparticles entangled and adhered together (e.g. CNTs) or stacked on top of each other (e.g. GNPs). Mixing and homogenization processes assist in disentangling these aggregates, to a certain extent, to uniformly distribute/disperse them into the host polymeric matrix. However, even under highly engineered processing protocols, a portion of these aggregates will exist in the final nanocomposite. Prolonged homogenization processes could enhance the dispersion/distribution of the nanofillers, however this enhancement comes with the caveat of increasing the chances for fracturing and deforming the individual particles and, consequently, the effective aspect ratios of these nanoparticles will be reduced leading to poor properties. Per the morphology investigations, the specimens processed in the experimental study were prone to this shortcoming. Hence, in order to consider such geometric imperfections in the simulations, in the current study the nanoparticles are treated as cylindrical aggregates each comprising an average of $\overline{N}$ individual particle. The number of particles in the aggregate was assumed to vary based on a normal distribution with an average value and a standard deviation estimated from the experimental observations. Furthermore, the aspect ratio of each cylindrical aggregate was selected based on the simple geometric aggregation model defined by the equation 7.1. This equation is simply constructed by assuming that the total volume of the nanoparticles is always conserved.

$$\lambda' = N^{1-3\alpha}\lambda \tag{7.1}$$

In this equation, λ is the nominal aspect ratio of the particles, λ' is the effective aspect ratio of the aggregates and α represents the diminution factor which governs the variation of the aspect ratio of the aggregates and should be estimated from the morphological studies. The parameter α can be a variable with some distribution or a constant representing the average value of the distribution ($\overline{\sigma}$). Figure 7.1 shows that by increasing the number N, bulkier aggregates will be generated as expected and Figure 7.2 shows that by increasing the $\overline{\alpha}$, lower aspect ratio aggregates will be generated in the sample's simulation cuboid.

Based on the experimental observations provided earlier in chapter 6, in the following study for the GNPs the number of particles in each aggregate was selected to follow a normal distribution with $\overline{N} = 5$ and a standard deviation $\sigma_N = 3$ (i.e. aggregates comprising 2-8 GNPs) and the aspect ratio was selected to be normally distributed with $\overline{\alpha} = -0.1$ and $\sigma_\alpha = 0.05$ (i.e. aggregates with reduced diameter due to the deformation and increased

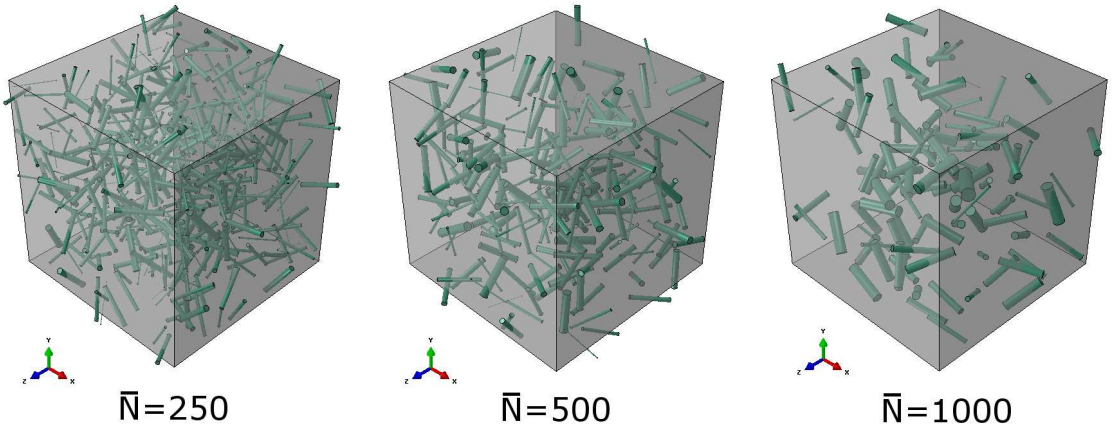

Figure 7.1: Particle Aggregation Parameter - The variation of the size of the particle aggregates by $\overline{N}$.($\overline{\alpha} = 0.5$)

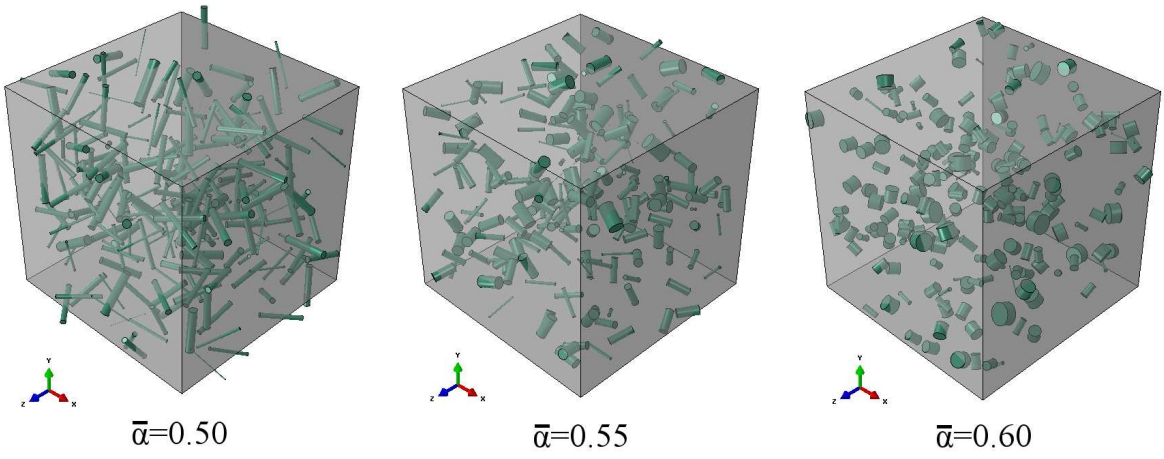

Figure 7.2: Aggregate Diminution Factor - The variation of the effective particle aggregate aspect ratio by diminution factor $\overline{\alpha}$.($\overline{N} = 500$)

thickness due to aggregation). Based on the experimental study, the CNTs are forming aggregates easier than GNPs specially for the high volume fraction configurations ($> 2\%wt$). In order to ensure the formation of low aspect ratio aggregates for CNTs, the average number of particles in the aggregate was selected to be $\overline{N} = 1000$ with $\sigma_N = 500$ (i.e. a wide distribution of large aggregates and small ones) and the aspect ratio was selected to be normally distributed with $\overline{\alpha} = 0.51$ and $\sigma_\alpha = 0.01$ (i.e. reduced length and increased diameter).

7.3 Electrical Conductivity Model Validation

The electrical conductivity of the CNT/epoxy, GNP/epoxy and CNT/GNP/epoxy polymer nanocomposites with nanoparticle loadings corresponding to the experimental values were evaluated by the established model in chapter 3. For each configuration, the simulation was repeated 20 times and the average electrical conductivity was calculated. To calculate the electrical conductivity in each simulation, the tunneling distance was set to be $\epsilon = 10\ nm$ and the pre-exponential constant was adopted from the values reported in Table 7.1 (parallel to the surface for GNPs and along the axis for CNTs). The aggregation and geometric imperfections are introduced to the simulations through the geometric particle aggregation model described in the section 7.2.2.

Figure 7.3 depicts the predicted electrical conductivities. By taking the reference threshold for the electrical conductivity to be $10^{-7}S/m$, the predicted percolation threshold is found to be 0.6%wt for CNT/epoxy, 0.8%wt for CNT/GNP/epoxy and 1.9%wt for GNP/epoxy configurations, respectively. The corresponding values measured experimentally are 0.6%wt for CNT/epoxy specimens, 0.9%wt for CNT/GNP/epoxy specimens and 3.6%wt for GNP/epoxy specimens(see Figure 6.14). It can be observed that model predictions are in good agreement with the experiments; expect for the GNP/epoxy specimen in which the experimental results are not reliable as described earlier.

Figure 7.4 compares the experimentally measured electrical conductivity of CNT/epoxy specimens with the model predictions. Up to 2.0%wt, good agreement is observed, but for higher loadings, both report the electrical conductivity saturation phase, however, the models predicts a better conductivity than experiment. This disparity between the model predictions and the experiment originates from the failure of the particle aggregation model to properly

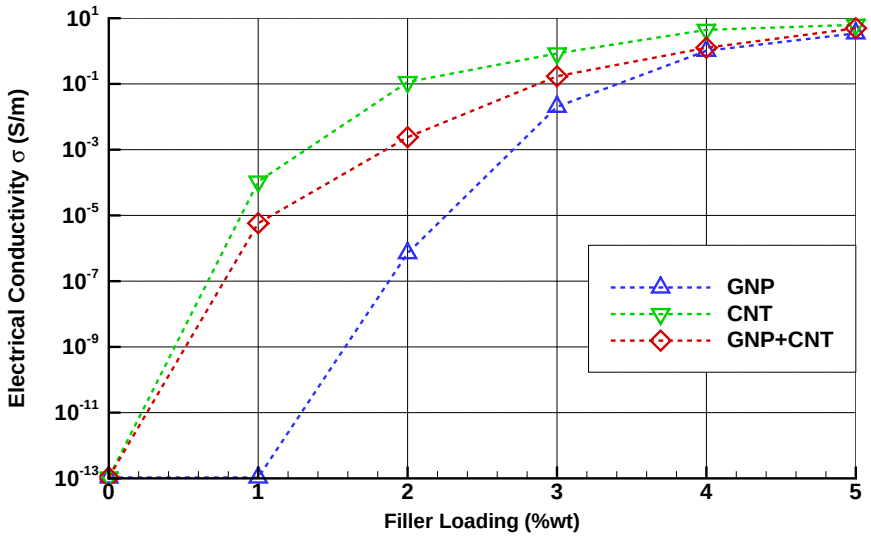

Figure 7.3: Computationally Predicted Electrical Conductivity - The predicted values for the electrical conductivities of CNT/epoxy, GNP/epoxy and CNT/GNP/epoxy specimens.

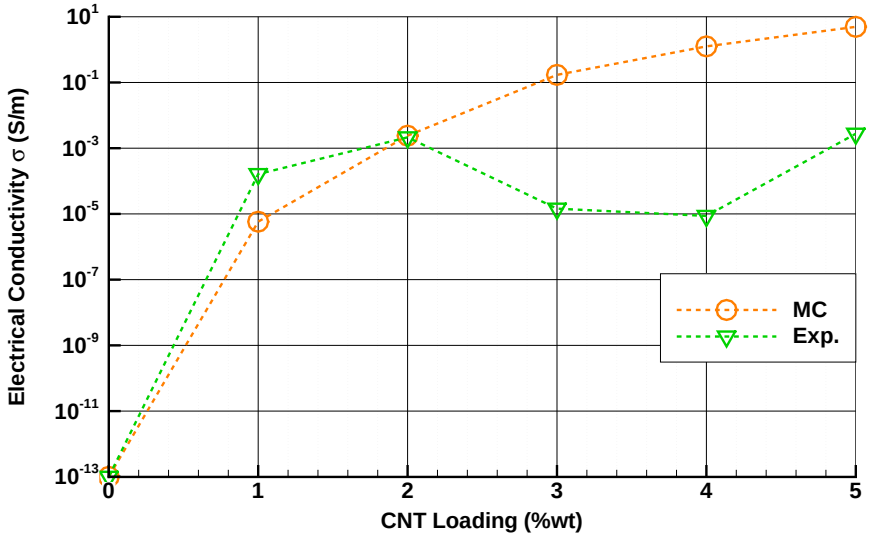

Figure 7.4: Electrical Conductivity Model Validation: CNT/epoxy - The predicted values for the electrical conductivities of CNT/epoxy specimens compared to the experimentally measured values. Exp.: experimental measurements, MC: Monte Carlo model predictions

introduce big aggregate of CNTs into the simulations upon their formation in the high CNT loading configuration.

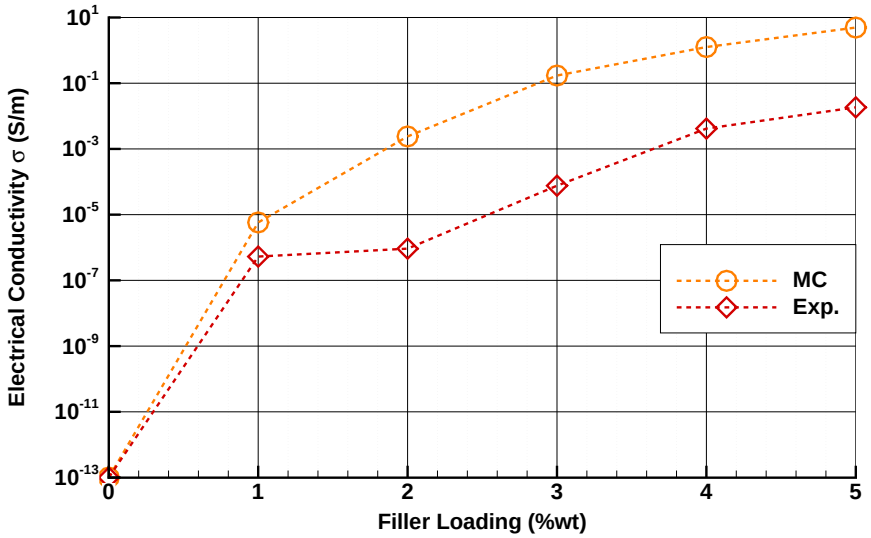

Figure 7.5: Electrical Conductivity Model Validation: CNT/GNP/epoxy - The predicted values for the electrical conductivities of CNT/GNP/epoxy specimens compared to the experimentally measured values. Exp.: experimental measurements, MC: Monte Carlo model predictions

Figure 7.5 compares the experimentally measured electrical conductivity of CNT/GNP/epoxy specimens with the model predictions. It can be observed that the model predicts the same trend for the electrical conductivity enhancement and the saturation at higher loadings. However, there is still a discrepancy between the predicted values and the experimental measurements. This can be ascribed to the modeling simplifications as well as the assumptions of constant tunneling length and the isotropic electrical conductivity for the particles and also the inherent inaccuracy of the simple geometric particle aggregation model utilized.

7.4 Thermal Conductivity Model Validation

The thermal conductivity of CNT/epoxy, GNP/epoxy and CNT/GNP/epoxy polymer nanocomposites with nanoparticle loadings corresponding to the experimental values were evaluated by the modified strong-contrast model. Furthermore, in order to verify the proposed model prediction, the thermal conductivity for each specimen was also calculated through

finite elements method. The same procedures described in the previous section were utilized to generate random distributions of the nanoparticles along with aggregation and imperfection. For each configuration the simulations were repeated 5 times and the average thermal conductivity was calculated.

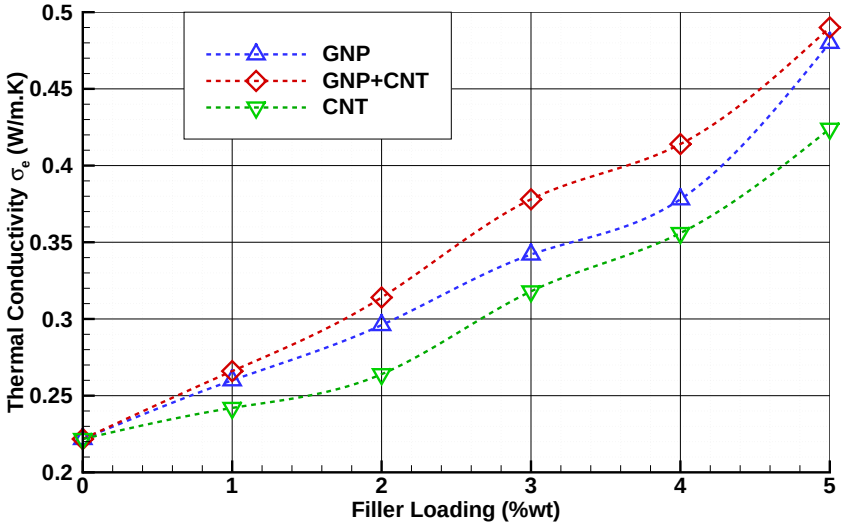

Figure 7.6: Computationally Predicted Thermal Conductivity - The predicted values for the thermal conductivities of CNT/epoxy, GNP/epoxy and CNT/GNP/epoxy specimens.

Figure 7.6 compares the thermal conductivity predicted by the proposed model for each configuration. It can be observed that the hybrid CNT/GNP/epoxy configurations attains the best thermal conductivity compared to the CNT/epoxy and GNP/epoxy configurations with only a single type of inclusions. Furthermore, for the assumed loadings, the GNP/epoxy specimens are predicted to attain better thermal conductivity compared to the CNT/epoxy specimens. The experimental measurements (see Figure 6.15) are also in support of these findings.

Figure 7.7 compares the model predictions with the experimental measurements of the thermal conductivity of GNP/epoxy specimens. Perfect agreement between the model predictions and the experimental measurements can be observed in this figure. An acceptable agreement between the model prediction and the FEM results can be observed in this case as well.

Figure 7.8 compares the model predictions with the experimental measurements of the ther-

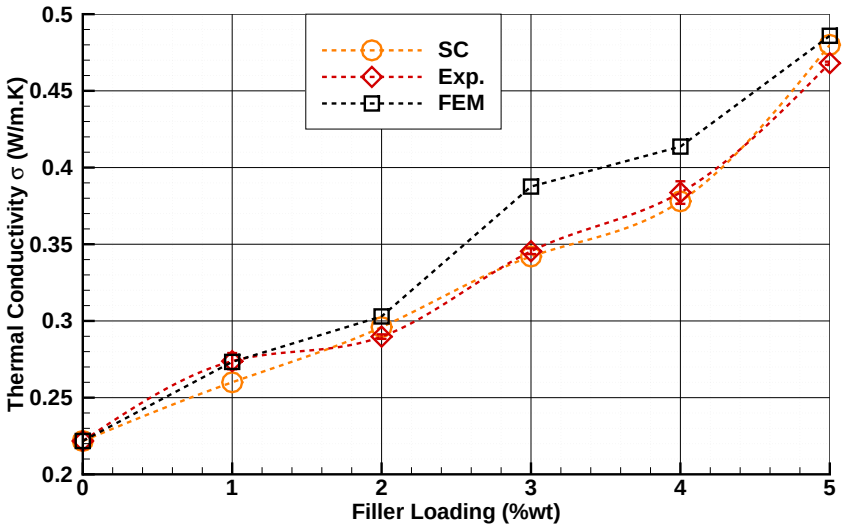

Figure 7.7: Thermal Conductivity Model Validation: GNP/epoxy - The predicted values for the thermal conductivities of GNP/epoxy specimens compared to the experimentally measured values. Exp.: experimental measurements, SC: modified strong-contrast predictions

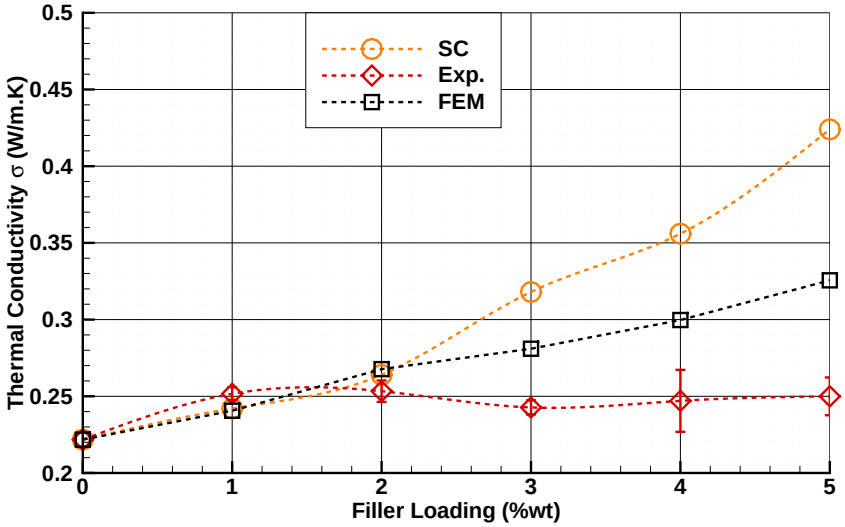

Figure 7.8: Thermal Conductivity Model Validation: CNT/epoxy - The predicted values for the thermal conductivities of CNT/epoxy specimens compared to the experimentally measured values. Exp.: experimental measurements, SC: modified strong-contrast predictions

mal conductivity for CNT/epoxy specimens. A good agreement is only observable for samples with lower loadings of CNTs ($< 2.0\%wt$), however, for higher loadings, both model and FEM overestimate the thermal conductivity compared to the experimental measurements. In analogy to the electrical conductivity study described earlier, this observation can be attributed to the high tendency of CNT/epoxy specimens to form large aggregates and the failure of the geometric aggregation model to properly simulate these conditions. Another contributing reason for this discrepancy is the high CNT/CNT interfacial resistance and its effect on the performance of the CNT percolation network which was not considered in the proposed model.

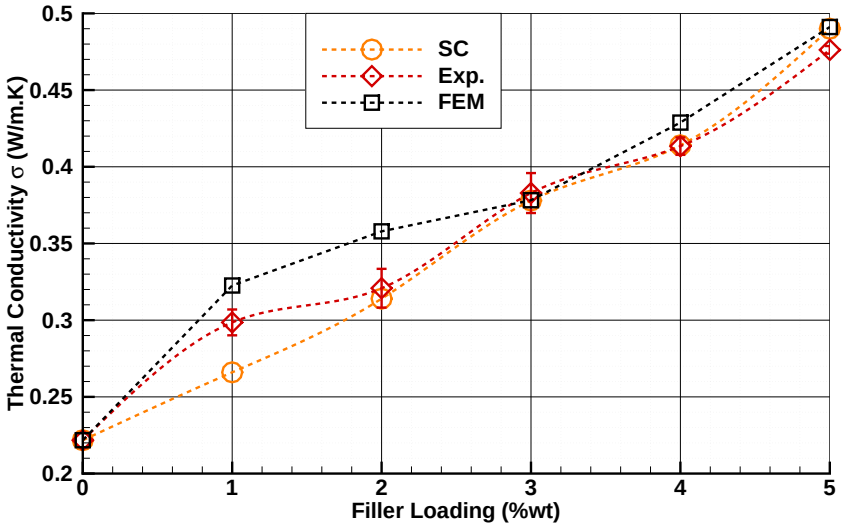

Figure 7.9: Thermal Conductivity Model Validation: CNT/GNP/epoxy - The predicted values for the thermal conductivities of CNT/GNP/epoxy specimens compared to the experimentally measured values. Exp.: experimental measurements, SC: modified strong-contrast predictions

Figure 7.9 compares the predicted values for the thermal conductivity of CNT/GNP/epoxy specimens with their corresponding experimentally measured values. A good agreement between the model predictions and the corresponding experimental values can be observed as well. An acceptable agreement between the model prediction and the FEM results can be observed in this case as well.

7.5 Conclusions

The electrical and thermal conductivities of the experimentally processed CNT/epoxy, GNP/epoxy and CNT/GNP/epoxy specimens were predicted using the computational models developed in the previous chapters. During each simulation, the physical and geometrical properties of the simulated nanofiller species were selected from the reported values in the chapter 6. To properly reconstruct the specimen morphology in the simulation, a simple model was proposed to account for the nanoparticles aggregation and imperfect geometry by assuming conservation of total volume. For this purpose, this model utilizes a set of parameters estimated from the morphological studies conducted in chapter 6. By utilizing this model, random distributions of the particles/aggregates were generated corresponding to the different experimental configurations reported in chapter 6. Finally, the effective electrical and thermal conductivities for each specimen were calculated several times and the averaged values were reported and compared to their experimental counterpart values.

The electrical conductivity model successfully predicted the electrical percolation threshold for the CNT/epoxy and the CNT/GNP/epoxy specimens. The predicted electrical conductivities were observed to be fairly in agreement with their corresponding experimental values for all configurations except for the CNT/epoxy specimens with high loading of the CNTs ($> 2.0\%wt$). For these cases, the extensive formation of CNT aggregates and the failure of the geometrical aggregation model to properly account for such conditions in the simulation cell are hypothesized to be the main reasons for the disagreement. The quantitative comparison between the model predictions and the experimental measurements also revealed that the model slightly overestimates the electrical conductivity for the hybrid specimens. This observation is attributed to the modeling uncertainties originating from the simplified assumptions of the electrical conductivity model (the constant tunneling distance and isotropic particle properties).

To validate the thermal conductivity modified strong-contrast model, its predictions were compared with the corresponding experimental measurements. The models predicts the best thermal conductivity for the hybrid configurations in agrement with the experimental observations. The model predictions for the thermal conductivities are also in good quantitative agreement with the experimental measurements except for the specimens with high loadings of CNTs. The observed disagreement is mainly attributed to the shortcoming of the utilized aggregation model. To further verify the proposed model, the thermal conductivity of all

configurations were also evaluated via the finite element method. A good agreement between the FEM calculation, the proposed model predictions and the experimental measurements constituted the validity of the proposed thermal conductivity model for both binary and ternary nanocomposite systems.

8

Conclusions and Future Work

8.1 Summary and Conclusions

To date, polymer nanocomposite are rapidly emerging into different structural and electronic applications owing to their interesting properties. They are light weigh, cost effective, easy to process and multifunctional. A polymer nanocomposite is consisting from a polymeric material and at least one nanostructured filler phase with at least one significant physical property that originates from its almost defect free confined nanostructure. Carbon nanotubes (CNTs) and graphite nanoplatelets (GNPs) are two allotropic forms of carbon with exceptional mechanical, electrical and thermal properties. Compared to an insulating pristine polymer, the electrical and the thermal conductivities of CNTs and GNPs are orders of magnitudes better. Based on simple rules of mixture law, it can be hypothesized that the addition of small amounts of CNTs or GNPs to an insulating polymeric host would significantly enhance its electrical and thermal conductivities. However, a number of experimental investigations challenged the correctness of this statement. A brief literature review revealed the lack of proper physics-based models to explain the transport properties of these polymer nanocomposites. Bearing this on mind, this dissertation was focused on investigating the electrical and the thermal properties of hybrid polymer nanocomposites based on CNTs and GNPs aiming to address some of the fundamental questions about estimating their transport properties.

The underlying mechanism of the electrical conductivity of polymer nanocomposites was investigated. It was hypothesized that the quantum electrical tunneling is the main mechanism of the electrical conductivity in these nanocomposites. To examine this hypothesis,

a computational approach based on the stochastic Monte-Carlo method was developed and implemented by a computer code (which will be referenced to by MC code). By considering GNP/polymer nanocomposites as an example, a number of simulations were carried out by the developed MC code. It was shown that when quantum tunneling is the only available mechanism for the electrical conduction, the MC code captures the electrical percolation threshold for GNP/polymer nanocomposites better than past efforts. It was argued that the gap between the predicted values and the experimental measurements originates from the modeling uncertainties and for not accounting for the imperfections in the experimental specimens.

A physical model was developed to quantify the electrical conductivity of the multiphase CNT/GNP/polymer nanocomposites. This model presumed that quantum tunneling is the main charge carrier transport mechanism. The model computes the effective electrical conductivity of the nanocomposite through estimating a purely geometrical parameter known as the critical distance. The critical distance represents the statistically averaged interparticle distance and it is a function of the particle geometry and the state of distribution and dispersion. In the next step, the model was implemented in the MC code. The developed MC code utilizes a number of physical and geometrical properties of the conductive nanoparticles utilized in the nanocomposite as inputs and then it generates a random distribution of these nanoparticles into a representative simulation cubical RVE with some simplifying assumptions about their geometry, their distribution and their state of dispersion. Finally, it computes the critical distance, and consequently through this parameter, it calculates the effective electrical conductivity of the nanocomposite. To validate the proposed model, its predictions were compared with reported experimental values for the electrical conductivities of CNT/polymer and GNP/polymer systems cited in the literature. It was observed that for low filler contents the model successfully predicts the electrical conductivity, however, for higher filler loadings, it only captures the trend. This shortcoming could be attributed to the modeling uncertainties mainly originating from the assumption of perfect distribution and dispersion of nanoparticles in the model.

To quantify the thermal conductivity of the multiphase CNT/GNP/polymer nanocomposites, a new formulation was developed based on the statistical continuum mechanics tools. This formulation can be categorized as a third order strong-contrast expansion that best works when there is a strong contrast between the properties of the system phases which is the

case for the polymer/nanofiller systems investigated in this dissertation. The proposed formulation estimates the thermal conductivity of such systems utilizing the physical and the morphological properties of each phase in the system. In the developed formulation the microstructural details are directly incorporated in the solution through one, two and three-points correlation functions; it can be extended to higher order correlation functions as well. To implement the proposed formulation, the one and two-point statistical correlation function were directly evaluated from the proposed microstructures generated by the MC code and the three-point correlation functions were estimated from the lower order correlation functions by using an approximation scheme. It was observed that the effective thermal conductivity estimated via the strong-contrast methods is highly sensitive to the proper selection of the reference phase; one of the parameters required by the proposed formulation. The proper value for the reference phase was computed through a novel method to minimize the sensitivity of the formulation and, consequently, to maximize its accuracy. To establish the validity of the proposed formulation, the effective thermal conductivity of a number of polymer nanocomposites comprising different volume loadings of the tubular (CNTs) and the disk-shaped (GNPs) nanoparticles was predicted both by the proposed method and by the finite element method (FEM). Perfect agreement between the predictions of the proposed formulation and the finite element established its validity.

It was hypothesized that the tubular and the disk-shaped geometries of CNTs and GNPs complement each other and, therefore, their synergistic combination could facilitate the formation of a conductive networks and consequently enhances the nanocomposite performance. To examine this hypothesis, a number of simulations were carried out for a set of carefully selected CNT/epoxy, GNP/epoxy and hybrid CNT/GNP/epoxy nanocomposites with GNPs as the main conductive phase and minute amounts of CNTs as the auxiliary conductive phase. It was observed that for equivalent filler loading contents, CNTs enhance the electrical conductivity better than GNPs and, therefore, when added to the GNPs network the hybrid CNT/GNP/polymer exhibits better electrical conductivity and, consequently, lower percolation threshold than the GNP/polymer nanocomposite. Furthermore, it was observed that for equivalent filler loadings, GNPs enhance the thermal conductivity better than CNTs; however, again the hybrid CNT/GNP/polymer nanocomposite observed to have better thermal conductivity than the GNP/polymer nanocomposites.

To provide a meaningful comparison between the measured experimental values and the computational estimates of the transport properties, the dissertation furnished a detailed

experimental study to investigate the electrical and thermal conductivities of CNT/epoxy, GNP/epoxy and hybrid CNT/GNP/epoxy nanocomposite. This study was designed aiming at serving two goals. First, to collect enough experimental data for validating the computational models developed earlier and second to re-examine the hypothesis of the synergy of the transport properties for a multi-phase nanocomposite based on CNTs/GNPs/epoxy. In this study, multiple step mixing/homogenization protocols were developed to ensure proper nanoparticles dispersion and distribution. A number of CNT/epoxy, GNP/epoxy and hybrid CNT/GNP/epoxy nanocomposites specimens were processed following these processing protocols. Detailed morphological studies were carried out for these specimens utilizing electron microscopy techniques. It was observed that by following the proposed mixing protocol a good distribution and dispersion of GNPs and CNTs can be achieved with fewer number of aggregates. However, it was also concluded that for high loading contents of the CNTs ($> 2.0\%wt$) the proposed mixing method fails and large aggregates are formed. The electrical and thermal conductivities of the different nanocomposite configurations specimens were measured. The experimental measurements confirmed the beneficial effects of the hybridization and established the synergistic nature of the transport properties for a trinary nanocomposite system compared to nanocomposites based on single nanofiller phase (CNTs or GNPs).

Having generated experimental measurements of the thermal and electrical conductivities for a trinary nanocomposite system, a number of simulations were carried out utilizing the raw material properties together with the measurements and morphological attributes of the nanocomposite specimens reported from the in-house experiments. To reduce the modeling uncertainties, the state of particle aggregation was approximated in the simulation cell through a simple geometrical model accounting for the particles aggregation and employing some of the morphological study results. The electrical and thermal conductivities of the CNT/epoxy, the GNP/epoxy and the hybrid CNT/GNP/epoxy specimens were computationally evaluated by the proposed models and compared to their counterpart experimental values. It was observed that the computational model was successfully capable of predicting the electrical percolation thresholds. The model predictions were found to be in satisfactory agreements with the experimental measurements except for the specimens with high contents of the CNTs ($> 2.0\%wt$). In light of the experimental observations this disagreement could be attributed to the formation of large CNT aggregates. Furthermore, it was argued that the remnant modeling uncertainties contribute to the discrepancies between the predicted and experimentally measured electrical conductivities values. A parallel study was carried

out to estimate the thermal conductivity of the different nanocomposites specimens and it was observed that the high-contrast model predictions are in perfect agreement with the experimental measurements for all configuration except for the specimens with high contents of the CNTs ($> 2.0\%wt$); originating from the large CNT aggregates. Finally, to further establish the validity of the proposed model, the thermal conductivity of CNT/GNP/epoxy specimens was also estimated by the finite element method and a good agreement between the strong-contrast model predictions, the experimental measurements and the finite element results was observed.

8.2 Future Work

Two computational models developed and validated in this study for evaluating the electrical and the thermal properties of the hybrid CNT/GNP/polymer nanocomposites. These models are based on a set of simplified assumptions. For future work, it is recommended to address the following issues within these models:

- These models should be very general; their validity for nanoparticles with complex morphologies other than tubes and disks should be established.
- The effect of the particle aggregation and non-uniform distribution on these models properties should be studied with more rigor. Better models to accounts for agglomerations need to be developed. One approach is to utilize experimental microstructural reconstruction tools to create these geometries.
- For the electrical conductivity model, the simplified assumptions of constant tunneling length and isotropic particle properties should be revisited.
- For the thermal conductivity model, the simplified assumptions of perfect particle/ polymer thermal bounding and isotropic properties for the particles should be re-examined.
- The models developed here capture basic transport behaviors of hybrid nanocomposites. However, knowing the chemistry and the physics of the interface/interphase between the nanoparticles and polymer is a crucial step for further developments of these models. Multiscale models based on molecular dynamics coupled with the current analysis could establish a feasible route to account for the interphase effects.

Bibliography

[1] Karen I. Winey and Richard A. Vaia. Polymer Nanocomposites. *MRS Bulletin*, 32(04):314–322, 2007.

[2] B. Jang and A. Zhamu. Processing of nanographene platelets (NGPs) and NGP nanocomposites: a review. *Journal of Materials Science*, 43(15):5092–5101, 2008.

[3] Farzana Hussain, Mehdi Hojjati, Masami Okamoto, and Russell E. Gorga. Review article: Polymer-matrix Nanocomposites, Processing, Manufacturing, and Application: An Overview. *Journal of Composite Materials*, 40(17):1511–1575, September 2006.

[4] T. W. Ebbesen, H. J. Lezec, H. Hiura, J. W. Bennett, H. F. Ghaemi, and T. Thio. Electrical conductivity of individual carbon nanotubes. *, Published online: 04 July 1996; | doi:10.1038/382054a0*, 382(6586):54–56, July 1996.

[5] Wolfgang Bauhofer and Josef Z. Kovacs. A review and analysis of electrical percolation in carbon nanotube polymer composites. *Composites Science and Technology*, 69(10):1486–1498, August 2009.

[6] Sasha Stankovich, Dmitriy A. Dikin, Geoffrey H. B. Dommett, Kevin M. Kohlhaas, Eric J. Zimney, Eric A. Stach, Richard D. Piner, SonBinh T. Nguyen, and Rodney S. Ruoff. Graphene-based composite materials. *Nature*, 442(7100):282–286, July 2006.

[7] Dale W. Schaefer and Ryan S. Justice. How Nano Are Nanocomposites? *Macromolecules*, 40(24):8501–8517, 2007.

[8] S. Iijima et al. Helical microtubules of graphitic carbon. *nature*, 354(6348):5658, 1991.

[9] Jonathan N. Coleman, Umar Khan, Werner J. Blau, and Yurii K. Gunko. Small but strong: A review of the mechanical properties of carbon nanotube-polymer composites. *Carbon*, 44(9):1624–1652, August 2006.

[10] E. T Thostenson, Z. Ren, and T. W Chou. Advances in the science and technology of carbon nanotubes and their composites: a review. *Composites science and technology*, 61(13):18991912, 2001.

[11] J. P Salvetat, J. M Bonard, N. H. Thomson, A. J. Kulik, L. Forro, W. Benoit, and L. Zuppiroli. Mechanical properties of carbon nanotubes. *Applied Physics A: Materials Science & Processing*, 69(3):255260, 1999.

[12] Mohammad Moniruzzaman and Karen I. Winey. Polymer Nanocomposites Containing Carbon Nanotubes. *Macromolecules*, 39(16):5194–5205, 2006.

[13] M.S. Dresselhaus, G. Dresselhaus, and R. Saito. Physics of carbon nanotubes. *Carbon*, 33(7):883–891, 1995.

[14] J. W.G Wildoer, L. C Venema, A. G Rinzler, R. E Smalley, and C. Dekker. Electronic structure of atomically resolved carbon nanotubes. *Nature*, 391(6662):5962, 1998.

[15] Savas Berber, Young-Kyun Kwon, and David Tomnek. Unusually High Thermal Conductivity of Carbon Nanotubes. *Physical Review Letters*, 84(20):4613–4616, May 2000.

[16] Zhidong Han and Alberto Fina. Thermal conductivity of carbon nanotubes and their polymer nanocomposites: A review. *Progress in Polymer Science*, 36(7):914–944, July 2011.

[17] R. Saito, G. Dresselhaus, M. S Dresselhaus, et al. *Physical properties of carbon nanotubes*, 35. Imperial college press London, 1998.

[18] J.K.W. Sandler, J.E. Kirk, I.A. Kinloch, M.S.P. Shaffer, and A.H. Windle. Ultra-low electrical percolation threshold in carbon-nanotube-epoxy composites. *Polymer*, 44(19):5893–5899, September 2003.

[19] Peng-Cheng Ma, Naveed A. Siddiqui, Gad Marom, and Jang-Kyo Kim. Dispersion and functionalization of carbon nanotubes for polymer-based nanocomposites: A review. *Composites Part A: Applied Science and Manufacturing*, 41(10):1345–1367, October 2010.

[20] F. Du, J. E Fischer, and K. I Winey. Effect of nanotube alignment on percolation conductivity in carbon nanotube/polymer composites. *Departmental Papers (MSE)*, page 79, 2005.

[21] Eric Pop, David Mann, Qian Wang, Kenneth Goodson, and Hongjie Dai. Thermal Conductance of an Individual Single-Wall Carbon Nanotube above Room Temperature. *Nano Lett.*, 6(1):96–100, 2005.

[22] Motoo Fujii, Xing Zhang, Huaqing Xie, Hiroki Ago, Koji Takahashi, Tatsuya Ikuta, Hidekazu Abe, and Tetsuo Shimizu. Measuring the Thermal Conductivity of a Single Carbon Nanotube. *Physical Review Letters*, 95(6):065502, 2005.

[23] P. Kim, L. Shi, A. Majumdar, and P. L. McEuen. Thermal Transport Measurements of Individual Multiwalled Nanotubes. *Physical Review Letters*, 87(21):215502, October 2001.

[24] Florian H. Gojny, Malte H.G. Wichmann, Bodo Fiedler, Ian A. Kinloch, Wolfgang Bauhofer, Alan H. Windle, and Karl Schulte. Evaluation and identification of electrical and thermal conduction mechanisms in carbon nanotube/epoxy composites. *Polymer*, 47(6):2036–2045, March 2006.

[25] Scott T. Huxtable, David G. Cahill, Sergei Shenogin, Liping Xue, Rahmi Ozisik, Paul Barone, Monica Usrey, Michael S. Strano, Giles Siddons, Moonsub Shim, and Pawel Keblinski. Interfacial heat flow in carbon nanotube suspensions. *Nature Materials*, 2(11):731–734, 2003.

[26] Hongliang Zhong and Jennifer R. Lukes. Interfacial thermal resistance between carbon nanotubes: Molecular dynamics simulations and analytical thermal modeling. *Physical Review B*, 74(12):125403, 2006.

[27] E. T. Swartz and R. O. Pohl. Thermal boundary resistance. *Reviews of Modern Physics*, 61(3):605–668, July 1989.

[28] S. Shenogin, A. Bodapati, L. Xue, R. Ozisik, and P. Keblinski. Effect of chemical functionalization on thermal transport of carbon nanotube composites. *Applied Physics Letters*, 85(12):2229–2231, September 2004.

[29] Thomas C. Clancy and Thomas S. Gates. Modeling of interfacial modification effects on thermal conductivity of carbon nanotube composites. *Polymer*, 47(16):5990–5996, July 2006.

[30] K. S. Novoselov, A. K. Geim, S. V. Morozov, D. Jiang, Y. Zhang, S. V. Dubonos, I. V. Grigorieva, and A. A. Firsov. Electric Field Effect in Atomically Thin Carbon Films. *Science*, 306(5696):666–669, October 2004.

[31] A. K. Geim and K. S. Novoselov. The rise of graphene. *Nature Materials*, 6(3):183–191, 2007.

[32] Hyunwoo Kim, Ahmed A. Abdala, and Christopher W. Macosko. Graphene/Polymer Nanocomposites. *Macromolecules*, 43(16):6515–6530, 2010.

[33] E. Rollings, G.-H. Gweon, S.Y. Zhou, B.S. Mun, J.L. McChesney, B.S. Hussain, A.V. Fedorov, P.N. First, W.A. de Heer, and A. Lanzara. Synthesis and characterization of atomically thin graphite films on a silicon carbide substrate. *Journal of Physics and Chemistry of Solids*, 67(910):2172–2177, September 2006.

[34] Xianbao Wang, Haijun You, Fangming Liu, Mingjian Li, Li Wan, Shaoqing Li, Qin Li, Yang Xu, Rong Tian, Ziyong Yu, Dong Xiang, and Jing Cheng. Large-Scale Synthesis of Few-Layered Graphene using CVD. *Chemical Vapor Deposition*, 15(1-3):5356, 2009.

[35] Dmitry V. Kosynkin, Amanda L. Higginbotham, Alexander Sinitskii, Jay R. Lomeda, Ayrat Dimiev, B. Katherine Price, and James M. Tour. Longitudinal unzipping of carbon nanotubes to form graphene nanoribbons. *Nature*, 458(7240):872–876, April 2009.

[36] Jianfeng Shen, Yizhe Hu, Chen Li, Chen Qin, Min Shi, and Mingxin Ye. Layer-by-Layer Self-Assembly of Graphene Nanoplatelets. *Langmuir*, 25(11):6122–6128, 2009.

[37] H. Fukushima, L. Drzal, B. Rook, and M. Rich. Thermal conductivity of exfoliated graphite nanocomposites. *Journal of Thermal Analysis and Calorimetry*, 85(1):235–238, 2006.

[38] Aiping Yu, Palanisamy Ramesh, Mikhail E. Itkis, Elena Bekyarova, and Robert C. Haddon. Graphite NanoplateletEpoxy Composite Thermal Interface Materials. *J. Phys. Chem. C*, 111(21):7565–7569, 2007.

[39] Chuangang Lin and D.D.L. Chung. Graphite nanoplatelet pastes vs. carbon black pastes as thermal interface materials. *Carbon*, 47(1):295–305, January 2009.

[40] Tapas Kuilla, Sambhu Bhadra, Dahu Yao, Nam Hoon Kim, Saswata Bose, and Joong Hee Lee. Recent advances in graphene based polymer composites. *Progress in Polymer Science*, 35(11):1350–1375, November 2010.

[41] E. J. Garboczi, K. A. Snyder, J. F. Douglas, and M. F. Thorpe. Geometrical percolation threshold of overlapping ellipsoids. *Physical Review E*, 52(1):819–828, July 1995.

[42] Kyriaki Kalaitzidou, Hiroyuki Fukushima, and Lawrence T. Drzal. Multifunctional polypropylene composites produced by incorporation of exfoliated graphite nanoplatelets. *Carbon*, 45(7):1446–1452, June 2007.

[43] Kyriaki Kalaitzidou, Hiroyuki Fukushima, Per Askeland, and Lawrence T. Drzal. The nucleating effect of exfoliated graphite nanoplatelets and their influence on the crystal structure and electrical conductivity of polypropylene nanocomposites. *Journal of Materials Science*, 43(8):2895–2907, October 2007.

[44] Sabyasachi Ganguli, Ajit K. Roy, and David P. Anderson. Improved thermal conductivity for chemically functionalized exfoliated graphite/epoxy composites. *Carbon*, 46(5):806–817, April 2008.

[45] GERALD L. POLLACK. Kapitza Resistance. *Reviews of Modern Physics*, 41(1):48–81, January 1969.

[46] S. H Xie, Y. Y Liu, and J. Y Li. Comparison of the effective conductivity between composites reinforced by graphene nanosheets and carbon nanotubes. *Applied Physics Letters*, 92(24):243121–243121–3, June 2008.

[47] Aiping Yu, Palanisamy Ramesh, Xiaobo Sun, Elena Bekyarova, Mikhail E. Itkis, and Robert C Haddon. Enhanced Thermal Conductivity in a Hybrid Graphite Nanoplatelet Carbon Nanotube Filler for Epoxy Composites. *Advanced Materials*, 20(24):47404744, 2008.

[48] S. Ghose, D. C. Working, J. W. Connell, J. G. Smith, K. A. Watson, D. M. Delozier, Y. P. Sun, and Y. Lin. Thermal Conductivity of UltemTM/Carbon Nanofiller Blends. *High Performance Polymers*, 18(6):961–977, December 2006.

[49] L. Monica Veca, Mohammed J. Meziani, Wei Wang, Xin Wang, Fushen Lu, Puyu Zhang, Yi Lin, Robert Fee, John W. Connell, and Ya-Ping Sun. Carbon Nanosheets for Polymeric Nanocomposites with High Thermal Conductivity. *Advanced Materials*, 21(20):20882092, 2009.

[50] O. Breuer and Uttandaraman Sundararaj. Big returns from small fibers: A review of polymer/carbon nanotube composites. *Polymer Composites*, 25(6):630645, 2004.

[51] Jeong-Mi Moon, Kay Hyeok An, Young Hee Lee, Young Soo Park, Dong Jae Bae, and Gyeong-Su Park. High-Yield Purification Process of Singlewalled Carbon Nanotubes. *J. Phys. Chem. B*, 105(24):5677–5681, 2001.

[52] Young Soo Park, Young Chul Choi, Keun Soo Kim, Dong-Chul Chung, Dong Jae Bae, Kay Hyeok An, Seong Chu Lim, Xiao Yan Zhu, and Young Hee Lee. High yield purification of multiwalled carbon nanotubes by selective oxidation during thermal annealing. *Carbon*, 39(5):655–661, April 2001.

[53] M. J Biercuk, M. C Llaguno, M. Radosavljevic, J. K Hyun, A. T Johnson, and J. E Fischer. Carbon nanotube composites for thermal management. *Applied Physics Letters*, 80(15):2767–2769, April 2002.

[54] Nabarun Roy, Rajatendu Sengupta, and Anil K. Bhowmick. Modifications of carbon for polymer composites and nanocomposites. *Progress in Polymer Science*, 37(6):781–819, June 2012.

[55] Xiaoyi Gong, Jun Liu, Suresh Baskaran, Roger D. Voise, and James S. Young. Surfactant-Assisted Processing of Carbon Nanotube/Polymer Composites. *Chem. Mater.*, 12(4):1049–1052, 2000.

[56] Cheol Park, Zoubeida Ounaies, Kent A Watson, Roy E Crooks, Joseph Smith Jr., Sharon E Lowther, John W Connell, Emilie J Siochi, Joycelyn S Harrison, and Terry L.St Clair. Dispersion of single wall carbon nanotubes by in situ polymerization under sonication. *Chemical Physics Letters*, 364(34):303–308, October 2002.

[57] Jonathan N Coleman, Werner J Blau, Alan B Dalton, Edgar Muoz, Steve Collins, Bog G Kim, Joselito Razal, Miles Selvidge, Guillermo Vieiro, and Ray H Baughman. Improving the mechanical properties of single-walled carbon nanotube sheets by intercalation of polymeric adhesives. *Applied Physics Letters*, 82(11):1682–1684, March 2003.

[58] R. Haggenmueller, H.H. Gommans, A.G. Rinzler, J.E. Fischer, and K.I. Winey. Aligned single-wall carbon nanotubes in composites by melt processing methods. *Chemical Physics Letters*, 330(34):219–225, November 2000.

[59] Jeffrey Jordan, Karl I. Jacob, Rina Tannenbaum, Mohammed A. Sharaf, and Iwona Jasiuk. Experimental trends in polymer nanocompositesa review. *Materials Science and Engineering: A*, 393(12):1–11, February 2005.

[60] M. Sennett, E. Welsh, J.B. Wright, W.Z. Li, J.G. Wen, and Z.F. Ren. Dispersion and alignment of carbon nanotubes in polycarbonate. *Applied Physics A: Materials Science & Processing*, 76(1):111–113, 2003.

[61] Kyriaki Kalaitzidou, Hiroyuki Fukushima, and Lawrence T. Drzal. A Route for Polymer Nanocomposites with Engineered Electrical Conductivity and Percolation Threshold. *Materials*, 3(2):1089–1103, February 2010.

[62] G. Z. Chen, M. S. P. Shaffer, D. Coleby, G. Dixon, W. Zhou, D. J. Fray, and A. H. Windle. Carbon Nanotube and Polypyrrole Composites: Coating and Doping. *Advanced Materials*, 12(7):522526, 2000.

[63] W.K Maser, A.M Benito, M.A Callejas, T Seeger, M.T Martinez, J Schreiber, J Muszynski, O Chauvet, Z Osvth, A.A Kos, and L.P Bir. Synthesis and characterization of new polyaniline/nanotube composites. *Materials Science and Engineering: C*, 23(12):87–91, January 2003.

[64] Q.H. Zeng, A.B. Yu, and G.Q. Lu. Multiscale modeling and simulation of polymer nanocomposites. *Progress in Polymer Science*, 33(2):191–269, February 2008.

[65] Young W. Kwon, David H. Allen, and R. Talreja. *Multiscale Modeling and Simulation of Composite Materials and Structures*. Springer, December 2007.

[66] Andrew R. Leach. *Molecular Modelling: Principles and Applications*. Prentice Hall, 2001.

[67] David P. Landau and Kurt Binder. *A Guide To Monte Carlo Simulations In Statistical Physics*. Cambridge University Press, September 2005.

[68] T. Mura. *Micromechanics of defects in solids*, 3. Springer, 1987.

[69] Junuthula Narasimha Reddy. *An Introduction to the Finite Element Method*. McGraw-Hill Higher Education, 2006.

[70] R. strumpler and J. Glatz-Reichenbach. FEATURE ARTICLE Conducting Polymer Composites. *Journal of Electroceramics*, 3(4):329–346, 1999.

[71] K. C Kao and W. Hwang. *Electrical transport in solids: with particular reference to organic semiconductors*. Taylor & Francis, 1979.

[72] A. R. Blythe and David Bloor. *Electrical Properties Of Polymers*. Cambridge University Press, June 2005.

[73] L. K. H. van Beek and B. I. C. F. van Pul. Internal field emission in carbon black-loaded natural rubber vulcanizates. *Journal of Applied Polymer Science*, 6(24):651655, 1962.

[74] J. Frenkel. On the Electrical Resistance of Contacts between Solid Conductors. *Physical Review*, 36(11):1604–1618, December 1930.

[75] J. Li, P. C. Ma, W. S. Chow, C. K. To, B. Z. Tang, and J.-K. Kim. Correlations between Percolation Threshold, Dispersion State, and Aspect Ratio of Carbon Nanotubes. *Advanced Functional Materials*, 17(16):32073215, 2007.

[76] I. Balberg, C. H. Anderson, S. Alexander, and N. Wagner. Excluded volume and its relation to the onset of percolation. *Physical Review B*, 30(7):3933–3943, October 1984.

[77] Lars Onsager. The effects of shape on the interaction of colloidal particles. *Annals of the New York Academy of Sciences*, 51(4):627659, 1949.

[78] E. Saar, J. Einasto, O. Toomet, A. A. Starobinsky, H. Andernach, M. Einasto, E. Kasak, and E. Tago. The supercluster-void network V. *Astronomy and Astrophysics*, 393(1):1–23, October 2002.

[79] Ian J Youngs. A geometric percolation model for non-spherical excluded volumes. *Journal of Physics D: Applied Physics*, 36(6):738–747, March 2003.

[80] Dietrich Stauffer and Amnon Aharony. *Introduction To Percolation Theory*. CRC Press, July 1994.

[81] Muhammad Sahimi. *Applications Of Percolation Theory*. CRC Press, January 1994.

[82] I. Balberg. Universal percolation-threshold limits in the continuum. *Physical Review B*, 31(6):4053–4055, March 1985.

[83] J Sandler, M.S.P Shaffer, T Prasse, W Bauhofer, K Schulte, and A.H Windle. Development of a dispersion process for carbon nanotubes in an epoxy matrix and the resulting electrical properties. *Polymer*, 40(21):5967–5971, October 1999.

[84] C.A. Martin, J.K.W. Sandler, M.S.P. Shaffer, M.-K. Schwarz, W. Bauhofer, K. Schulte, and A.H. Windle. Formation of percolating networks in multi-wall carbon-nanotubeepoxy composites. *Composites Science and Technology*, 64(15):2309–2316, November 2004.

[85] Josef Z. Kovacs, Bala S. Velagala, Karl Schulte, and Wolfgang Bauhofer. Two percolation thresholds in carbon nanotube epoxy composites. *Composites Science and Technology*, 67(5):922–928, April 2007.

[86] C.A. Martin, J.K.W. Sandler, A.H. Windle, M.-K. Schwarz, W. Bauhofer, K. Schulte, and M.S.P. Shaffer. Electric field-induced aligned multi-wall carbon nanotube networks in epoxy composites. *Polymer*, 46(3):877–886, January 2005.

[87] H. Garmestani, M.s. Al-Haik, K. Dahmen, R. Tannenbaum, D. Li, S.s. Sablin, and M.y. Hussaini. Polymer-Mediated Alignment of Carbon Nanotubes under High Magnetic Fields. *Advanced Materials*, 15(22):19181921, 2003.

[88] Sameer S Rahatekar, Marc Hamm, Milo S. P Shaffer, and James A Elliott. Mesoscale modeling of electrical percolation in fiber-filled systems. *The Journal of Chemical Physics*, 123(13):134702–134702–5, October 2005.

[89] James T. Wescott, Paul Kung, and Amitesh Maiti. Conductivity of carbon nanotube polymer composites. *Applied Physics Letters*, 90(3):033116 –033116–3, January 2007.

[90] Leonard H. Switzer and Daniel J. Klingenberg. Flocculation in simulations of sheared fiber suspensions. *International Journal of Multiphase Flow*, 30(1):67–87, January 2004.

[91] Jing Li and Jang-Kyo Kim. Percolation threshold of conducting polymer composites containing 3D randomly distributed graphite nanoplatelets. *Composites Science and Technology*, 67(10):2114–2120, August 2007.

[92] Chunyu Li, Erik T. Thostenson, and Tsu-Wei Chou. Effect of nanotube waviness on the electrical conductivity of carbon nanotube-based composites. *Composites Science and Technology*, 68(6):1445–1452, May 2008.

[93] Florent Dalmas, Rmy Dendievel, Laurent Chazeau, Jean-Yves Cavaill, and Catherine Gauthier. Carbon nanotube-filled polymer composites. Numerical simulation of electrical conductivity in three-dimensional entangled fibrous networks. *Acta Materialia*, 54(11):2923–2931, June 2006.

[94] L. Berhan and A. M. Sastry. Modeling percolation in high-aspect-ratio fiber systems. II. The effect of waviness on the percolation onset. *Physical Review E*, 75(4):041121, April 2007.

[95] Chunyu Li and Tsu-Wei Chou. Continuum percolation of nanocomposites with fillers of arbitrary shapes. *Applied Physics Letters*, 90(17):174108–174108–3, April 2007.

[96] I. Balberg and N. Binenbaum. Computer study of the percolation threshold in a two-dimensional anisotropic system of conducting sticks. *Physical Review B*, 28(7):3799–3812, October 1983.

[97] I. Balberg, N. Binenbaum, and N. Wagner. Percolation Thresholds in the Three-Dimensional Sticks System. *Physical Review Letters*, 52(17):1465–1468, April 1984.

[98] Dong-Li Shi, Xi-Qiao Feng, Yonggang Y. Huang, Keh-Chih Hwang, and Huajian Gao. The Effect of Nanotube Waviness and Agglomeration on the Elastic Property of Carbon Nanotube-Reinforced Composites. *Journal of Engineering Materials and Technology*, 126(3):250, 2004.

[99] Ruediger Schueler, Juergen Petermann, Karl Schulte, and Hans-Peter Wentzel. Agglomeration and electrical percolation behavior of carbon black dispersed in epoxy resin. *Journal of Applied Polymer Science*, 63(13):17411746, 1997.

[100] Ingo Alig, Tetyana Skipa, Dirk Lellinger, and Petra Ptschke. Destruction and formation of a carbon nanotube network in polymer melts: Rheology and conductivity spectroscopy. *Polymer*, 49(16):3524–3532, July 2008.

[101] D. Bigg. Thermal conductivity of heterophase polymer compositions. In *Thermal and Electrical Conductivity of Polymer Materials*, 119 of *Advances in Polymer Science*, pages 1–30. Springer Berlin / Heidelberg, 1995.

[102] S. Torquato. Effective electrical conductivity of two-phase disordered composite media. *Journal of Applied Physics*, 58(10):3790–3797, November 1985.

[103] Z. Hashin and S. Shtrikman. A Variational Approach to the Theory of the Effective Magnetic Permeability of Multiphase Materials. *Journal of Applied Physics*, 33(10):3125–3131, October 1962.

[104] R. L. Hamilton and O. K. Crosser. Thermal Conductivity of Heterogeneous Two-Component Systems. *Industrial & Engineering Chemistry Fundamentals*, 1(3):187–191, 1962.

[105] Hiroshi Hatta and Minoru Taya. Effective thermal conductivity of a misoriented short fiber composite. *Journal of Applied Physics*, 58(7):2478–2486, October 1985.

[106] Lawrence E. Nielsen. The Thermal and Electrical Conductivity of Two-Phase Systems. *Industrial & Engineering Chemistry Fundamentals*, 13(1):17–20, 1974.

[107] I. H. Tavman. Thermal and mechanical properties of aluminum powder-filled high-density polyethylene composites. *Journal of Applied Polymer Science*, 62(12):21612167, 1996.

[108] Hu Zhou, Shimin Zhang, and Mingshu Yang. The effect of heat-transfer passages on the effective thermal conductivity of high filler loading composite materials. *Composites Science and Technology*, 67(6):1035–1040, May 2007.

[109] A.G. Every, Y. Tzou, D.P.H. Hasselman, and R. Raj. The effect of particle size on the thermal conductivity of ZnS/diamond composites. *Acta Metallurgica et Materialia*, 40(1):123–129, January 1992.

[110] Ce-Wen Nan, R. Birringer, David R Clarke, and H. Gleiter. Effective thermal conductivity of particulate composites with interfacial thermal resistance. *Journal of Applied Physics*, 81(10):6692–6699, May 1997.

[111] Martin L Dunn and Minoru Taya. The effective thermal conductivity of composites with coated reinforcement and the application to imperfect interfaces. *Journal of Applied Physics*, 73(4):1711–1722, February 1993.

[112] S. Torquato and M. D. Rintoul. Effect of the Interface on the Properties of Composite Media. *Physical Review Letters*, 75(22):4067–4070, November 1995.

[113] Robert Lipton and Bogdan Vernescu. Composites with Imperfect Interface. *Proceedings of the Royal Society of London. Series A: Mathematical, Physical and Engineering Sciences*, 452(1945):329–358, February 1996.

[114] N. Shenogina, S. Shenogin, L. Xue, and P. Keblinski. On the lack of thermal percolation in carbon nanotube composites. *Applied Physics Letters*, 87(13):133106–133106–3, September 2005.

[115] Young Seok Song and Jae Ryoun Youn. Evaluation of effective thermal conductivity for carbon nanotube/polymer composites using control volume finite element method. *Carbon*, 44(4):710–717, April 2006.

[116] Suchismita Ghosh, Wenzhong Bao, Denis L. Nika, Samia Subrina, Evghenii P. Pokatilov, Chun Ning Lau, and Alexander A. Balandin. Dimensional crossover of thermal transport in few-layer graphene. *Nature Materials*, 9(7):555–558, 2010.

[117] Xiaotuo Li, Xinyu Fan, Yingdan Zhu, Juan Li, John M. Adams, Shirley Shen, and Hongzhou Li. Computational modeling and evaluation of the thermal behavior of randomly distributed single-walled carbon nanotube/polymer composites. *Computational Materials Science*, 63(0):207–213, October 2012.

[118] Muhammad Zain-ul Abdein, Sajjad Azeem, and Syed Mushtaq Shah. Computational investigation of factors affecting thermal conductivity in a particulate filled composite using finite element method. *International Journal of Engineering Science*, 56(0):86–98, July 2012.

[119] Rajatendu Sengupta, Mithun Bhattacharya, S. Bandyopadhyay, and Anil K. Bhowmick. A review on the mechanical and electrical properties of graphite and modified graphite reinforced polymer composites. *Progress in Polymer Science*, 36(5):638–670, May 2011.

[120] G.C. Psarras. Hopping conductivity in polymer matrixmetal particles composites. *Composites Part A: Applied Science and Manufacturing*, 37(10):1545–1553, October 2006.

[121] N. F. Mott. Conduction in non-crystalline materials. *Philosophical Magazine*, 19(160):835–852, 1969.

[122] Jeppe C. Dyre and Thomas B. Schrder. Universality of ac conduction in disordered solids. *Reviews of Modern Physics*, 72(3):873–892, July 2000.

[123] I Balberg. Tunnelling and percolation in lattices and the continuum. *Journal of Physics D: Applied Physics*, 42(6):064003, March 2009.

[124] G. E. Pike and C. H. Seager. Percolation and conductivity: A computer study. I. *Physical Review B*, 10(4):1421–1434, 1974.

[125] L. Berhan and A. M. Sastry. Modeling percolation in high-aspect-ratio fiber systems. I. Soft-core versus hard-core models. *Physical Review E*, 75(4):041120, April 2007.

[126] Chunyu Li and Tsu-Wei Chou. Electrical Conductivities of Composites with Aligned Carbon Nanotubes. *Journal of Nanoscience and Nanotechnology*, 9(4):2518–2524, 2009.

[127] G. Belford, L. Jackson Laslett, J. N. Snyder, J. M. Cook, I. J. Good, M. J. R. Healy, A. J. M. Hitchcock, N. S. Mendelsohn, H. I. Meyer, B. J. Hollingsworth, J. C. P. Miller, Thomas H. Southard, and Harvey M. Wagner. Technical Notes and Short Papers. *Mathematical Tables and Other Aids to Computation*, 11(58):79–104, April 1957. ArticleType: research-article / Full publication date: Apr., 1957 / Copyright 1957 American Mathematical Society.

[128] G. R Ruschau, S. Yoshikawa, and R. E Newnham. Resistivities of conductive composites. *Journal of Applied Physics*, 72(3):953–959, August 1992.

[129] S.F. Wang and A.A. Ogale. Continuum space simulation and experimental characterization of electrical percolation behavior of particulate composites. *Composites Science and Technology*, 46(2):93–103, 1993.

[130] A. Dani and A.A. Ogale. Electrical percolation behavior of short-fiber composites: Experimental characterization and modeling. *Composites Science and Technology*, 56(8):911–920, 1996.

[131] Toshiaki Natsuki, Morinobu Endo, and Tatsuhiro Takahashi. Percolation study of orientated short-fiber composites by a continuum model. *Physica A: Statistical Mechanics and its Applications*, 352(24):498–508, July 2005.

[132] Harvey Gould and Jan Tobochnik. *An introduction to computer simulation methods: applications to physical systems*. Addison-Wesley, 1988.

[133] Yan Geng, Shu Jun Wang, and Jang-Kyo Kim. Preparation of graphite nanoplatelets and graphene sheets. *Journal of Colloid and Interface Science*, 336(2):592–598, August 2009.

[134] R K Goyal, S D Samant, A K Thakar, and A Kadam. Electrical properties of polymer/expanded graphite nanocomposites with low percolation. *Journal of Physics D: Applied Physics*, 43(36):365404, September 2010.

[135] Tong Wei, Guilian Luo, Zhuangjun Fan, Chao Zheng, Jun Yan, Chengzhao Yao, Weifang Li, and Chen Zhang. Preparation of graphene nanosheet/polymer composites using in situ reductionextractive dispersion. *Carbon*, 47(9):2296–2299, August 2009.

[136] Weng W-G., Chen G-H., Wu D-J., and Yan W-L. HDPE/expanded graphite electrically conducting composite. *Composite Interfaces*, 11(2):131–143, 2004.

[137] Xiao-Mei Chen, Jing-Wei Shen, and Wen-Yi Huang. Novel electrically conductive polypropylene/graphite nanocomposites. *Journal of Materials Science Letters*, 21(3):213–214, 2002.

[138] G. Ambrosetti, N. Johner, C. Grimaldi, T. Maeder, P. Ryser, and A. Danani. Electron tunneling in conductor-insulator composites with spherical fillers. *Journal of Applied Physics*, 106(1):016103 –016103, July 2009.

[139] G. Ambrosetti, I. Balberg, and C. Grimaldi. Percolation-to-hopping crossover in conductor-insulator composites. *Physical Review B*, 82(13):134201, October 2010.

[140] G. Ambrosetti, C. Grimaldi, I. Balberg, T. Maeder, A. Danani, and P. Ryser. Solution of the tunneling-percolation problem in the nanocomposite regime. *Physical Review B*, 81(15):155434, April 2010.

[141] C Gau, Cheng-Yung Kuo, and H S Ko. Electron tunneling in carbon nanotube composites. *Nanotechnology*, 20(39):395705, September 2009.

[142] B I Shklovskii and A L fros. Percolation theory and conductivity of strongly inhomogeneous media. *Soviet Physics Uspekhi*, 18(11):845–862, November 1975.

[143] M. Pollak and G. E. Pike. ac Conductivity of Glasses. *Physical Review Letters*, 28(22):1449–1451, May 1972.

[144] J D Sherwood. Packing of spheroids in three-dimensional space by random sequential addition. *Journal of Physics A: Mathematical and General*, 30(24):L839–L843, December 1997.

[145] T. Kanit, S. Forest, I. Galliet, V. Mounoury, and D. Jeulin. Determination of the size of the representative volume element for random composites: statistical and numerical approach. *International Journal of Solids and Structures*, 40(1314):3647–3679, June 2003.

[146] D. Eberly. Intersection of cylinders. *Geometric Tools, Inc*, 2000.

[147] Jing Li, Pui-Shan Wong, and Jang-Kyo Kim. Hybrid nanocomposites containing carbon nanotubes and graphite nanoplatelets. *Materials Science and Engineering: A*, 483484(0):660–663, June 2008.

[148] S Kumar, L L Sun, S Caceres, B Li, W Wood, A Perugini, R G Maguire, and W H Zhong. Dynamic synergy of graphitic nanoplatelets and multi-walled carbon nanotubes in polyetherimide nanocomposites. *Nanotechnology*, 21(10):105702, March 2010.

[149] Tae-Keun Hong, Dong Wook Lee, Hyun Jung Choi, Hyeon Suk Shin, and Byeong-Su Kim. Transparent, Flexible Conducting Hybrid Multilayer Thin Films of Multiwalled Carbon Nanotubes with Graphene Nanosheets. *ACS Nano*, 4(7):3861–3868, 2010.

[150] Kyriaki Kalaitzidou, Hiroyuki Fukushima, and Lawrence T. Drzal. A new compounding method for exfoliated graphitepolypropylene nanocomposites with enhanced flexural properties and lower percolation threshold. *Composites Science and Technology*, 67(10):2045–2051, August 2007.

[151] Fuan He, Sienting Lau, Helen Laiwa Chan, and Jintu Fan. High Dielectric Permittivity and Low Percolation Threshold in Nanocomposites Based on Poly(vinylidene fluoride) and Exfoliated Graphite Nanoplates. *Advanced Materials*, 21(6):710715, 2009.

[152] Guohua Chen, Wengui Weng, Dajun Wu, and Cuiling Wu. PMMA/graphite nanosheets composite and its conducting properties. *European Polymer Journal*, 39(12):2329–2335, December 2003.

[153] Guoxiu Wang, Juan Yang, Jinsoo Park, Xinglong Gou, Bei Wang, Hao Liu, and Jane Yao. Facile Synthesis and Characterization of Graphene Nanosheets. *The Journal of Physical Chemistry C*, 112(22):8192–8195, 2008.

[154] M. B. Bryning, M. F. Islam, J. M. Kikkawa, and A. G. Yodh. Very Low Conductivity Threshold in Bulk Isotropic Single-Walled Carbon NanotubeEpoxy Composites. *Advanced Materials*, 17(9):11861191, 2005.

[155] Salvatore Torquato. *Random Heterogeneous Materials*. Springer, October 2005.

[156] Tungyang Chen, George J Dvorak, and Yakov Benveniste. Mori-Tanaka estimates of the overall elastic moduli of certain composite materials. *ASME Transactions Series E Journal of Applied Mechanics*, 59:539–546, September 1992.

[157] Ral Guinovart-Daz, Reinaldo Rodrguez-Ramos, Julin Bravo-Castillero, Federico J. Sabina, Jos A. Otero-Hernndez, and Gerard A. Maugin. A recursive asymptotic homogenization scheme for multi-phase fibrous elastic composites. *Mechanics of Materials*, 37(11):1119–1131, November 2005.

[158] Muneo Hori and Sunil Munasighe. Generalized HashinShtrikman variational principle for boundary-value problem of linear and non-linear heterogeneous body. *Mechanics of Materials*, 31(7):471–486, July 1999.

[159] J. C. Affdl and J. L. Kardos. The Halpin-Tsai equations: a review. *Polymer Engineering & Science*, 16(5):344352, 1976.

[160] Mark J. Beran. *Statistical continuum theories*. Interscience Publishers, 1968.

[161] M. G. Rozman and Marcel Utz. Uniqueness of Reconstruction of Multiphase Morphologies from Two-Point Correlation Functions. *Physical Review Letters*, 89(13):135501, 2002.

[162] S. Torquato. Exact Expression for the Effective Elastic Tensor of Disordered Composites. *Physical Review Letters*, 79(4):681–684, July 1997.

[163] D. C Pham and S. Torquato. Strong-contrast expansions and approximations for the effective conductivity of isotropic multiphase composites. *Journal of Applied Physics*, 94(10):6591–6602, November 2003.

[164] H. Le Quang, G. Bonnet, and D. C. Pham. Bounds and correlation approximation for the effective conductivity of heterogeneous plates. *Physical Review E*, 84(6):061153, December 2011.

[165] Peter B Corson. Correlation functions for predicting properties of heterogeneous materials. II. Empirical construction of spatial correlation functions for two-phase solids. *Journal of Applied Physics*, 45(7):3165–3170, July 1974.

[166] A. Mikdam, A. Makradi, S. Ahzi, H. Garmestani, D.S. Li, and Y. Remond. Effective conductivity in isotropic heterogeneous media using a strong-contrast statistical continuum theory. *Journal of the Mechanics and Physics of Solids*, 57(1):76–86, January 2009.

[167] M. Baniassadi, S. Ahzi, H. Garmestani, D. Ruch, and Y. Remond. New approximate solution for N-point correlation functions for heterogeneous materials. *Journal of the Mechanics and Physics of Solids*, 60(1):104–119, January 2012.

[168] Vincent C. Tung, Li-Min Chen, Matthew J. Allen, Jonathan K. Wassei, Kurt Nelson, Richard B. Kaner, and Yang Yang. Low-Temperature Solution Processing of GrapheneCarbon Nanotube Hybrid Materials for High-Performance Transparent Conductors. *Nano Letters*, 9(5):1949–1955, 2009.

[169] Young-Kwan Kim and Dal-Hee Min. Durable Large-Area Thin Films of Graphene/Carbon Nanotube Double Layers as a Transparent Electrode. *Langmuir*, 25(19):11302–11306, 2009.

[170] Jun Yan, Tong Wei, Zhuangjun Fan, Weizhong Qian, Milin Zhang, Xiande Shen, and Fei Wei. Preparation of graphene nanosheet/carbon nanotube/polyaniline composite as electrode material for supercapacitors. *Journal of Power Sources*, 195(9):3041–3045, May 2010.

[171] Jun Xu, John P. Donohoe, and Charles U. Pittman Jr. Preparation, electrical and mechanical properties of vapor grown carbon fiber (VGCF)/vinyl ester composites. *Composites Part A: Applied Science and Manufacturing*, 35(6):693–701, June 2004.